Lawrence Berkeley National Laboratory

Title

Petrology, Density and Velocity Structure of Subducting Lithosphere and the Mantle

Permalink

https://escholarship.org/uc/item/0s84z9np

Author

Ita, J.J.

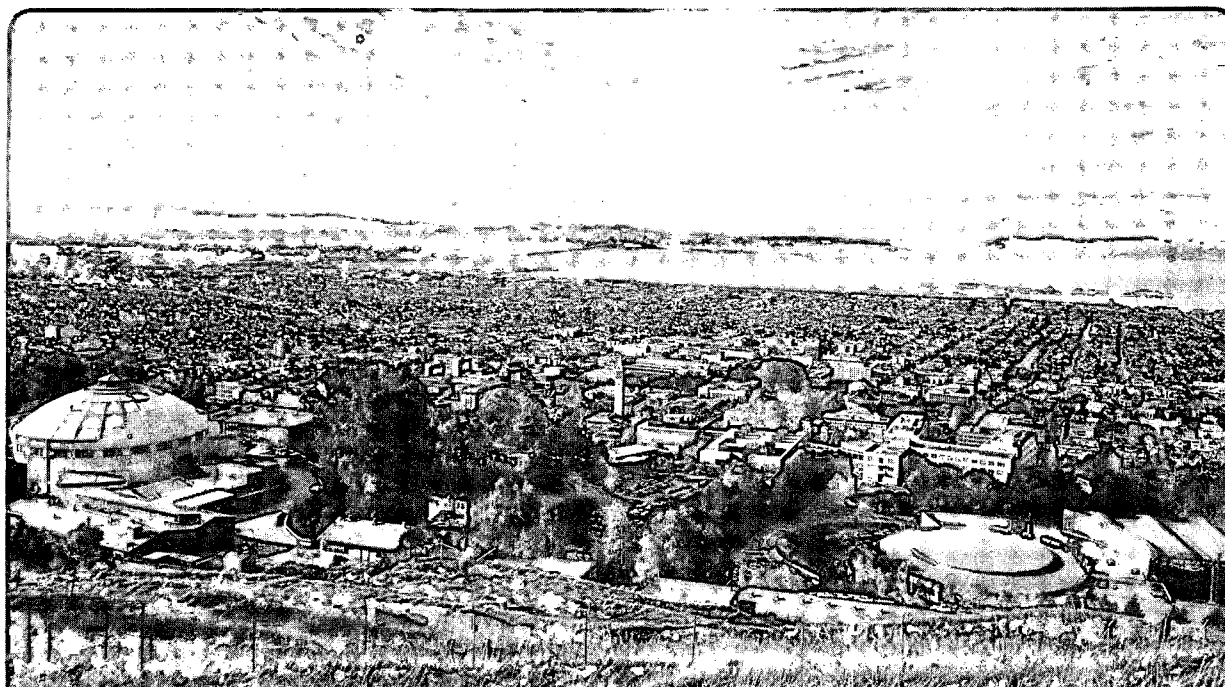**Publication Date**

1992-11-01

Lawrence Berkeley Laboratory
UNIVERSITY OF CALIFORNIA

EARTH SCIENCES DIVISION

Petrology, Density, and Velocity Structure of
Subducting Lithosphere and the Mantle

J.J. Ita
(Ph.D. Thesis)

November 1992

DISCLAIMER

DISCLAIMER

Petrology, Density, and Velocity Structure of Subducting Lithosphere and the Mantle

Joel Jacob Ita
(Ph.D. Thesis)

Earth Sciences Division
Lawrence Berkeley Laboratory
University of California
Berkeley, California 94720

November 1992

Petrology, Density, and Velocity Structure of Subducting Lithosphere and the Mantle

Copyright © 1992

by

Joel Jacob Ita

To My Grandfather, Art McLain

The man was a constant reminder to me that there is an important distinction

between knowledge and wisdom and of the two wisdom is greater.

A kinder person has never lived.

Table of Contents

Acknowledgements

I thank my advisor Lane Johnson for his invaluable guidance and infinite patience through this process. He never questioned my long sojourn into mineral physics and hopefully it has resulted in an investigation of his liking.

Much of this study would not have materialized with out the help of my fellow graduate student Lars Stixrude. He supplied me with the programs to implement the thermodynamic potential and much advice and guidance. So much guidance in fact that his fiance Carolina Lithgow-Bertelloni often joked that I was his first "student".

I also enjoyed many enlightening conversations with Philip Stark on the statistical nuances of this undertaking. Helpful reviews of parts of this manuscript by Raymond Jeanloz, Mark Bukowinski and Mark Richards resulted in noticeable improvements and some careful thinking about my methodology.

The encouragement by and interaction with my cubicle mates Don Vasco, Jay Pulliam, Mike Leonard, and the rest of the gang at CCS also buoyed me through many low moments and supplied many of the high moments during my stay here. Better friends and colleagues I will never find.

Of course, I would never have arrived at this point without the help of my family. Foremost among them is my wife Stacey. Her support and understanding have been sorely tried over the years. I am glad that completing this dissertation means almost as much to her as it does to me. Love you babe! Of my father and mother, Don and Judy, I can't say enough. They allowed me to dream of great things and then did their most to see that I could achieve them. I set quite a pace for my brothers and sisters, Thad, Polly, Robert, and Jody, earlier on, but they ran their own races and seem to have finished ahead of me. Really guys, I'm getting out of school and getting a real job just like the rest of you!

Abstract

Petrology, Density, and Velocity Structure of Subducting
Lithosphere and the Mantle

by

Joel Jacob Ita

Doctor of Philosophy in Geophysics

University of California at Berkeley

Professor Lane R. Johnson, Chair

I compare the predictions of compositional models of the mantle to properties inferred from seismological data by constructing phase diagrams in the MgO - FeO - CaO - Al_2O_3 - SiO_2 system and estimating the elasticity of the relevant minerals. Mie-Grüneisen theory is combined with the Birch-Murnaghan or the Universal equation of state to extrapolate experimental measurements of thermal and elastic properties to high pressures and temperatures. The resulting semi-empirical thermodynamic potentials combined with the estimated phase diagrams predict self-consistently the density, seismic parameter and mantle adiabats for a given compositional model. The transition zone and upper mantle are likely to have similar compositons. I find that both olivine rich (pyrolite-like) and olivine poor (piclogite-like) compositions agree well with the observed properties of the upper mantle and transition zone. Compositions low in olivine substantially underestimate the magnitude of the 400 km discontinuity unless they have enough Al to cause the pyroxene-garnet transition to coincide approximately with this boundary. The dissolution of Ca rich perovskite at 18 gigapascals in these models provides a promising explaination of the 520 km discontinuity. Also, the temperature jump associated with a compositional change at 400 km leads to poor agreement with seismic observations for all compositions. However, the composition of the lower mantle may differ from that of the upper mantle. The candidate upper mantle compositions considered here provide acceptable fits to lower mantle observations, but along adiabats which are cooler than expected. If the mantle is isochemical, a thermal boundary layer near 670 km depth is highly unlikely.

Isobaric phase changes induced by thermal anomalies in subduction zones have a significant effect on the material properties of that region. Strong lateral and vertical velocity and density gradients not predicted by previous modelling efforts are found to exist. The nature of the velocity and density distribtions in subducting slabs is greatly affected by the presence or absence of metastable olivine deep within them. Its presence would be conducive to dynanmic layering of the mantle while its absence will have the opposite effect.

Chapter 1

Introduction

1.1 Geophysical Background

The structure of the Earth is dominated by internal layering in the form of radial shells (Figure 1.1). Secondary features consist of departures from the mean properties within a given shell. The thermal and chemical evolution of the Earth, the dynamics of its interior and thus the forces which drive plate tectonics depend critically on the nature of this structure. If the radial boundaries in the mantle are due to changes in phase alone, either whole mantle or layered convection could exist, depending on the nature of the phase transitions. If they are marked by a change in composition as well as phase, convection would most likely occur within the shells but not between them. The reduction of heat and material transport between layers would engender the presence of large scale chemical heterogeneities and the preservation of primordial heat. Lateral variations in material properties outline the patterns of convection within and between the spherical shells. Sharp contrasts in these deviations across a boundary would indicate a barrier to flow, while a high positive correlation is more ambiguous. It may represent flow across the boundary or thermal coupling of the convective patterns in each shell with little or no exchange of material.

Some models of the early evolution of the Earth suggest strong chemical fractionation and the formation of multiple compositional layers. These models, which are based on analogy with crustal magma chambers, envision silicate liquids sinking relative to lighter olivine in the shallow mantle, but rising relative to denser perovskite in the lower mantle, producing a chemically distinct transition zone [*Anderson and Bass*, 1986; *Ohtani*, 1988]. However, detailed analysis of very high Rayleigh number dynamics indicates that convective mixing in a planet scale magma chamber may completely prevent crystal fractionation [*Tonks and Melosh*, 1990]. Furthermore, extensive crystal fractionation appears inconsistent with the Earth's trace element chemistry [*Kato et al.*, 1988; but see also *Walker and Agee*, 1989].

Upper

Transition Zone

400 km

Mantle

670 km
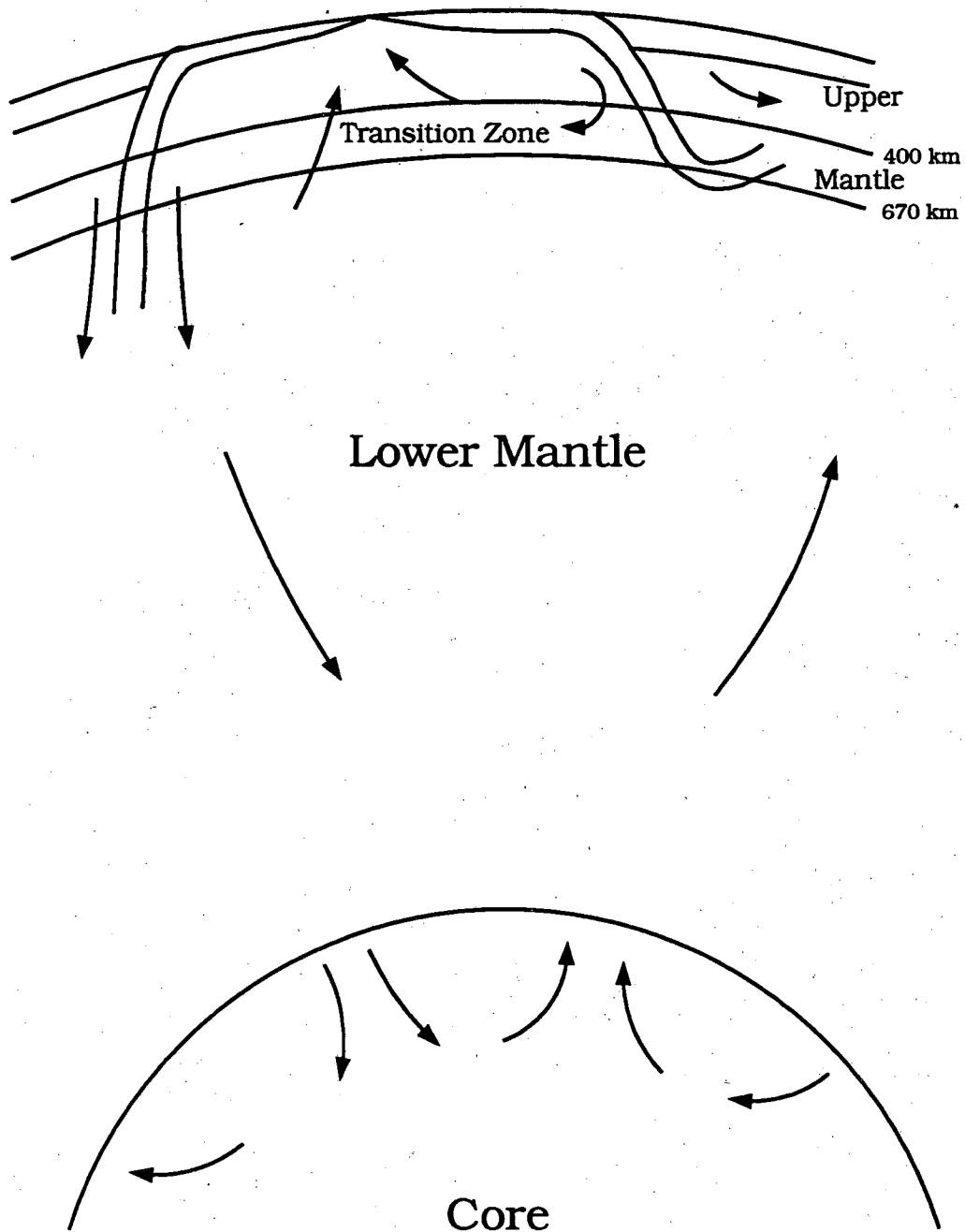
Lower Mantle

Core

Fig. 1.1 Cartoon of the Earth's internal structure depicting the major features such as the upper mantle, the transition zone, the lower mantle, and the core. Secondary features such as the lateral difference between oceanic and continental lithosphere and differing views of convective patterns in the mantle are also represented. In this investigation, the upper mantle is defined as the fraction of the mantle that lies above the 670 km discontinuity, the transition zone lies between the 400 and 670 km discontinuities, and the lower mantle lies between the 670 km discontinuity and the core.

1.2 Subduction Zone Properites

Many types of geophysical observations bear on the nature of mantle layering, but none have unambiguously resolved whether the Earth's mantle is isochemical or compositionally layered. Deep seismicity patterns, used to infer the presence of subducting slabs, show that many slabs penetrate into and in some cases, span the entire length of the transition zone [*Isacks* and *Molnar*, 1971; *Jarrard*, 1986]. Travel time and wave-form studies indicate that slabs in the Kurile, Mariana and Tonga trenches penetrate well into the lower mantle [*Creager and Jordan*, 1984, 1986; *Fischer et. al.*, 1991; *Silver and Chan*, 1986], although these results are controversial [*Anderson*, 1987; *Zhou et al.*, 1990; *Gaherty et al.*, 1991; *Schwartz et al.*, 1991]. Tomographic images of the mantle also suggest deep mantle penetration of slabs in some areas, while in other regions they appear to be confined to the upper mantle [*Zhou and Clayton*, 1990; *van. der Hilst et al.*, 1991; *Fukao et al.*, 1992]. Isochemical mantle models easily accommodate these observations, but slab penetration is also consistent with a compositionally layered mantle in which the layers are separated by permeable (leaky) boundary layers, or boundaries that are only intermittently breached [*Silver et al.*, 1988; *Machetel and Weber*, 1991], *Peltier and Solheim*, 1992].Tomographic models [*Fukao et al.*, 1992] and analysis of seismicity patterns [*Giardini* and *Woodhouse*, 1984, 1986] also indicate that at least some subducting slabs are substantially deformed by the boundary between the upper and lower mantle, suggesting a change in material properties at 670 km depth. Slab deformation is easily explained by a change in composition between upper and lower mantles, but is also consistent with an isochemical mantle which exhibits a 10- to 30-fold increase in viscosity [*Vassiliou et al.*, 1984; *Gurnis* and *Hager*, 1988] or contains an endothermic phase change whose Calpeyron slope is less than -2 MPa/K at 670 km depth [*Machetel and Weber*, 1991; *Peltier and Solheim*, 1992]. The viscosity increase is actually thought to exist in the Earth on the basis of geoid observations [*Hager*, 1984; *Hager and Richards*, 1989]. The spinel to perovskite phase transition thought to be responsible for the 670 km discontinuity has a Clapeyron slope of -2.8 MPa/K; within the range needed for stratified convection.

At the same time, the absence of slab deformation at 400 km is not inconsistent with compositional change at that boundary provided the attendant changes in density and viscosity are not large

enough to significantly impede the slab's descent. Many geochemical observations are most easily explained by the survival of two or more physically distinct reservoirs, such as multiple convective layers [*Depaolo*, 1983; *Allegre and Turcotte*, 1985; *Zindler and Hart*, 1986; *Silver et al.*, 1988]. However, inefficient mixing may allow the long-term survival of chemical heterogeneity on many length scales even in single-layer convection [*Gurnis and Davies*, 1986].

1.3   Mantle Properites

Comparison of seismological observations of the Earth's interior with known material properties is the most direct way of determining the composition of the mantle. It was first recognized by *Bernal* [1936] that pressure-induced phase transformations could cause increases in seismic velocity with depth. Birch [1952] later argued that the anomalously high seismic velocity gradients in the transition zone were most easily explained by a series of phase changes, rather than the effect of pressure on a single phase. Since that time, many workers have tried to constrain mantle composition by comparing the density and elastic properties of the Earth to that of high pressure minerals. The density and elasticity of the mantle is inferred from seismological data while that of the high pressure phases has been measured experimentally or estimated from systematics of analog minerals.

Studies of this kind have followed three different approaches. The first two involve the use an equation of state to extrapolate the mineralogical elasticity data to mantle conditions. Following this tact, some investigators searched through a spectrum of mineral assemblages to find those that were consistent with the seismological data. In the upper mantle, this has been attempted by *Anderson* [1967], *Burdick and Anderson* [1975], *Lees et al.* [1983], *Bina and Wood* [1987], and *Duffy and Anderson* [1989]. Similar lower mantle studies were conducted by *Butler and Anderson* [1978] and *Bina and Silver* [1990]. Alternatively, others have chosen to compare the properties of phase assemblages predicted by mantle compositions based on studies of mantle xenoliths or geochemical considerations [*Jeanloz and Thompson*, [1983]; *Anderson and Bass*, 1984; *Bass and Anderson*, 1984; *Weidner*, 1985; *Akaogi et al.*, 1987; *Irifune*, 1987; *Duffy and Anderson*, 1989]. The third approach involves using an equation of state to extrapolate the inferred elastic properties of the mantle to ambient conditions and then perform the comparison [*Jeanloz and Knittle*, 1989; *Bina and Silver*, 1990; *Bukowinski and Wolf*,

1990].

The petrologic complexity of the transition zone and the extreme pressures and temperatures of the lower mantle, however, have hindered these efforts. Until recently, information about the high pressure behavior of many possible mantle minerals was virtually unknown. Forced to rely on estimates of these crucial quantities, the aforementioned investigators have come to very different conclusions regarding the composition of the transition zone and the existence of chemical stratification in the Earth's mantle.

1.4   Summary

A good of body evidence has been advanced from the diverse fields of seismology, geodynamics, mineral physics, and geochemistry to explain the structure and composition of the mantle, yet a consensus still eludes us. This lack of agreement is no cause for concern at the present moment however. Recent advances in high pressure experimental petrology have disentangled the stability relations among the more than 25 phases which may exist in the transition zone, while Brillouin spectroscopy has determined the elastic constants of many of these phases. In situ measurements at combined high pressures and temperatures have placed the first experimental constraints on the thermal expansivity of likely lower mantle phases at high pressure. Innovative application of theory has also reduced the reliance on estimates of parameters needed to describe the high pressure, high temperature behavior of possible mantle minerals.

Armed with this new information, I analyze three models of mantle composition by combining a self-consistent thermodynamic formulation with recent measurements of mineral elasticity, phase equilibria and high pressure thermal expansivity. This formulation is used to predict the properties of their associated phase assemblages under conditions thought to exist in the mantle. A comparison between the predicted properties and those that exist in the Earth provides constraints on mantle composition. I then extend this investigation to predict the effect of temperature on the mineralogy, density and velocity structure in subduction zones.

The average density and elastic properties of the Earth are well constrained, but there still exists

significant uncertainty. The cause of this uncertainty and its quantification are the subject of chapter two. In chapter three, the origin of the model compositions used is discussed. A review of the phase equilibria studies relevant to these compositions is also presented. Coupled with this is a discussion of the pressure - temperature phase diagrams used in this study. Chapter four outlines the theory used to predict the properties of these phases under mantle conditions. The improvements of this formulation over that used in previous investigations are noted. A discussion of the determination and reliability of the parameters used in this formulation is also given. At this point, the comparison between the predicted and expected density and elastic properties of the upper and lower mantle is made in chapter five. Effects of error on the results of this section are also explored. In chapter six, the effect of temperature and compositional contrasts on the mineralogy of subducting slabs is presented. Lateral changes in mineral assemblage predicted by my models may explain some of the more perplexing aspects of the tomography models and should have a noticable impact on forward modeling of travel-times, waveforms and convective patterns. This is followed by a summary and some concluding remarks in chapter seven.

Chapter 2

Observational Constraints on Mantle Properties

2.1 Introduction

Most of our knowledge of mantle properties is derived from observations of seismic waves that travel through it. Measurements of waveforms and traveltimes of body waves and surface waves as well as the periods of free oscillations of the Earth provide us the information needed to estimate compressional (V_P) and shear wave (V_S) velocities and density as a function of depth. From this information I can infer material properties of the Earth such as bulk (K) and shear (μ) modulus as well as density (ρ). Given these material properties, one can subsume the composition and petrology of the mantle.

As with any estimate of the physical properties of nature, there is error present due to the inability to make all the measurements necessary, inexactness in our measurements when they are made, and inadequacies in the theory used to derive from these measurements knowledge about the desired property. Early attempts were made to quantify the errors in V_P and V_S by *Wiggins* [1969,1972], in ρ by *Gilbert et al.* [1973], and in velocity and density simultaneously by *Press* [1970]. Our knowledge of the mean properties of the Earth has progressed since that time, but estimates of its associated error have not kept pace. Recently, most estimates of resolution and uncertainty of velocity and density in the Earth have been derived from long period surfaces waves (see *Montager and Tanimoto*, 1991; *Tanimoto*, 1991; and references therein). The depth resolution of these models in the mantle is approximately 200 to 400 km and is unsuitable for a meaningful analysis of the upper mantle, though it may be adequate for the lower mantle.

One way out of this dilemma is to get an estimate of the uncertainty from the V_P, V_S and ρ profiles themselves. Enough models exist in the literature, that one could consider them as a random sample of the true average profile of the Earth. From this sample I can then estimate the mean and standard deviation of the average velocity or density. Many of the profiles in this estimate represent the average properties of the Earth, but a significant number are drawn from regional studies. Implicit in

this approach is the assumption that distribution of regional profiles used in the study is equal to their distribution in the Earth and thus will not bias the estimate of the mean. As shown below, this assumption appears to be valid.

2.2 Density

I estimate the expected density profile of the mantle and its uncertainty with the mean and standard deviation of 14 published models [*Derr*, 1969; *Haddon and Bullen*, 1969; *Mizutani and Abe*, 1971; *Wang*, 1972; *Jordan and Anderson*, 1974; *Gilbert and Dziewonski*, 1975; *Kind and Muller*, 1975; *Hart et al.*, 1976; *Nakada and Hashizume*, 1983; *Lerner-Lam and Jordan*, 1987; *Montagner and Anderson*, 1989; *Dost*, 1990] by standard statistical formulae [*Bevington*, 1969]. The five most recent models are based exclusively on surface wave data which provide radial density resolution of approximately 100 km in the upper 700 km of the mantle. Most of these utilized a starting model based on body-wave observations and thus agree in the placement of the discontinuities in the upper mantle, though the gradients between them do vary significantly. The older models are based mostly on free oscillation data and give information about the mantle over its entire depth range. The resolution of these models is poorer in the upper mantle, but they agree in general with the surface wave models.

Some of the older models may contain systematic errors due to the effects of attenuation [*Hart et al.*, 1976], but this error does not appear to significantly bias the mean in the upper mantle. A comparison is made with the Earth model PREM [*Dzeiwonski* and *Anderson*, 1981] which was purposely left out of the average to provide an independent test of the mean. The mean and PREM are in excellent agreement throughout the upper mantle except just above the 400 and 670 km discontinuities (see Figure 2.1). Even there, PREM falls within the uncertainty of the mean. It appears that any error introduced by the older models has only increased the standard deviation in this region, making it a conservative estimate. A significant bias does appear between PREM and our mean curve in the lower mantle. The standard deviation estimated in this region should overestimate the actual uncertainty given the increased disparity between profiles with and without this bias. In order to account for this bias, I assume that PREM represents the true mean in the lower mantle and has the same standard deviation as the biased curve. The implications of this assumption for mantle composition is discussed in chapter 5.
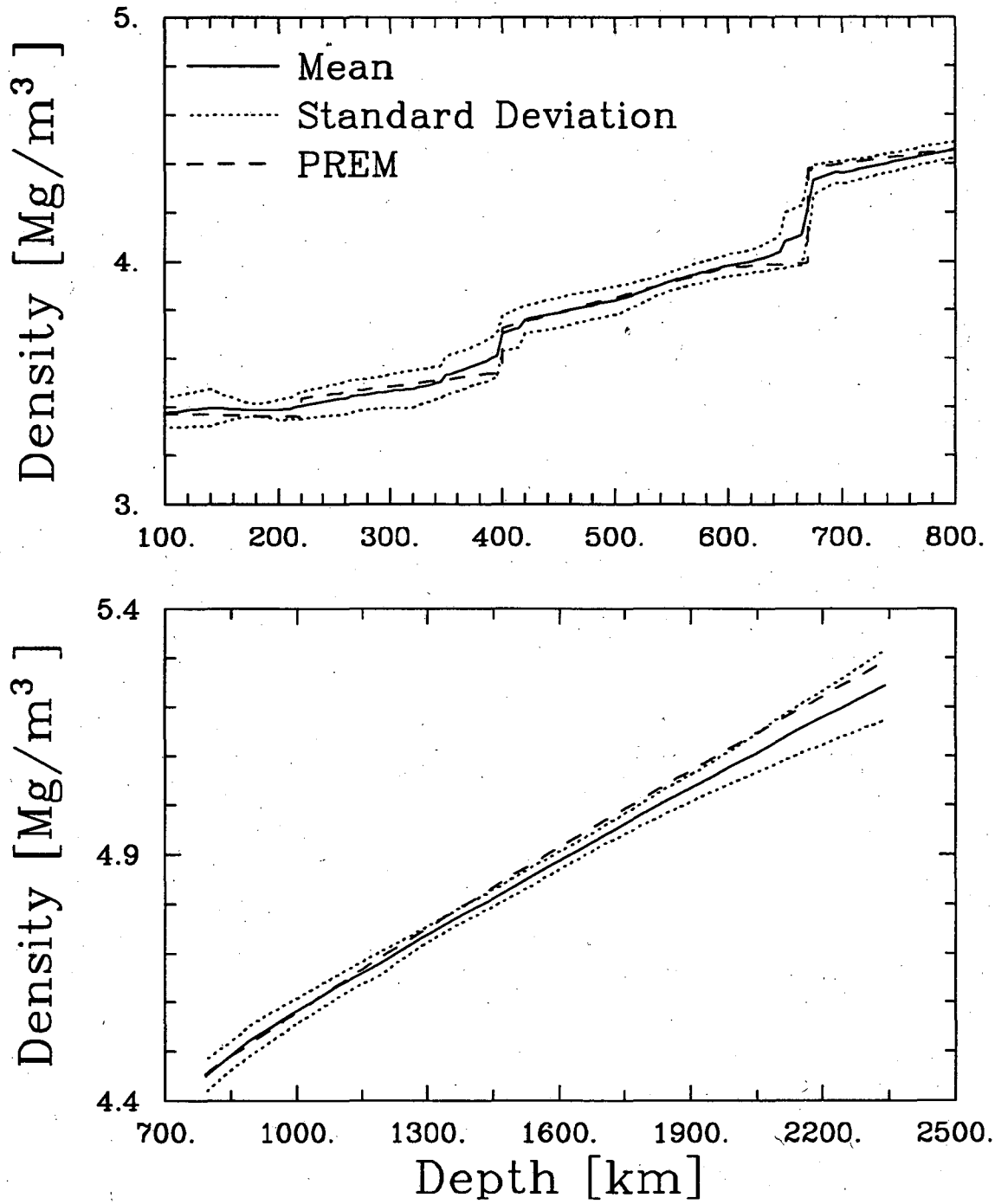
Fig. 2.1. Comparison of the expected mean and standard deviation of density with the PREM density model throughout the mantle.

Also, in this region, the average standard deviation is 0.6% which is in good agreement with other estimates of the error [*Silver et al.*, 1988].

2.3 Velocity

We base our estimate of the expected velocity distribution in the mantle and its uncertainty on 37 P-wave velocity (V_P) profiles and 34 S-wave velocity (V_S) profiles [*Chinnery and Toksoz*, 1967; *Hales et al.*, 1968; *Herrin*, 1968; *Fairborn* 1969; *Hales and Roberts*, 1970; *Buchbinder* 1971; *Randall*, 1971; *Robinson and Kovach*, 1972; *Wright and Cleary*, 1972; *Wiggins et al.*, 1973; *Gilbert and Dziewonski*, 1975; *Hart*, 1975; *Kind and Muller*, 1975; *Dey-Sarkar and Wiggins*, 1976; *Hart et al.*, 1976; *King and Calcagnile*, 1976; *Fukao*, 1977; *Burdick and Helmberger*, 1978; *Sengupta and Julian*, 1978; *McMechan*, 1979; 1981; *Uhrhammer*, 1979; *Given and Helmberger*, 1980; *Hales et al.*, 1980; *Burdick*, 1981; *Dziewonski and Anderson*, 1981; *Vinnik and Ryaboy*, 1981; *Fukao et al.*, 1982; *Nakada and Hashizume*, 1983; *Grand and Helmberger*, 1984a,b; *Walck*, 1984, 1985; *Lyon-Caen*, 1986; *Lerner-Lam and Jordan*, 1987; *Paulssen*, 1987; *Grad*, 1988; *Graves and Helmberger*, 1988; *Montagner and Anderson*, 1989; *Lefevre and Helmberger*, 1989; *Bowman and Kennett*, 1990; *Dost*, 1990; *Kennett and Engdahl*, 1991] mostly generated from high resolution waveform or travel-time studies of body waves with the remainder coming from surface wave or free oscillation investigations. In the upper mantle, I have selected only profiles that were generated after 1974 to avoid any systematic bias that may have been introduced by attenuation. In the lower mantle, *Hart et al.* [1976] find that attenuation has little effect on velocities; a result confirmed below. The average radial resolution of these models in the upper mantle is on the order of 20 to 30 km. Shown in Figures 2.2 and 2.3 are the mean and standard deviation of V_P and V_S respectively.

Presently, the behavior of the shear modulus in individual minerals at elevated pressures and temperatures is poorly known. For this reason, I use the bulk sound velocity (V_Φ) as a constraint on the predicted properties of the Earth generated in this investigation. V_Φ can be extracted from V_P and V_S via:

$$V^2_\Phi = K/\rho = V^2_P - 4/3V^2_S \qquad\qquad 2.1$$

As shown in this expression, V_Φ depends only on K and ρ, whose values can be accurately predicted at

Fig. 2.2. a) Number of P wave profiles used in the analysis. b) Mean (solid line), standard deviation (dotted line), and maximum deviation from the mean (dashed line) of the P wave velocity profiles in the upper mantle.
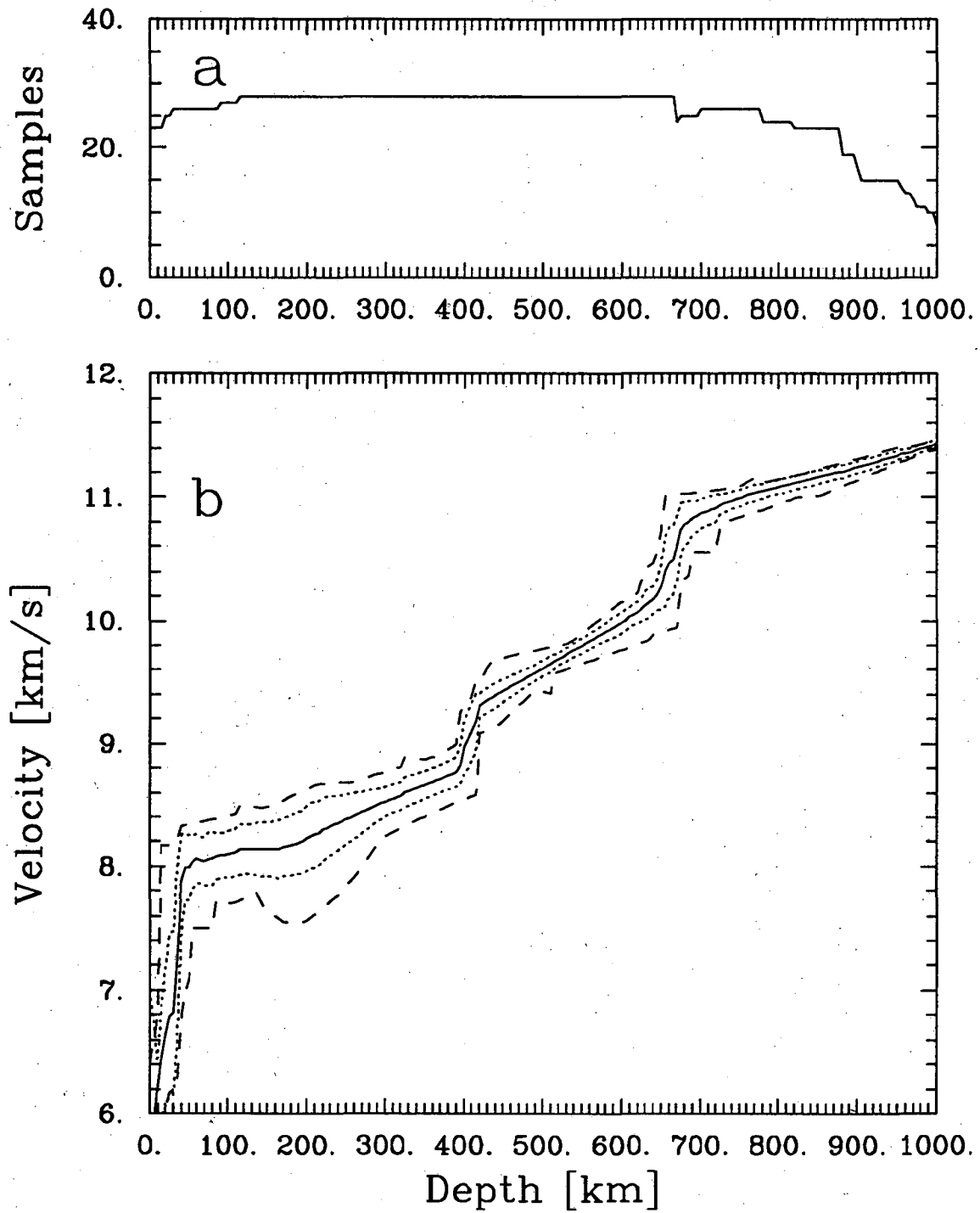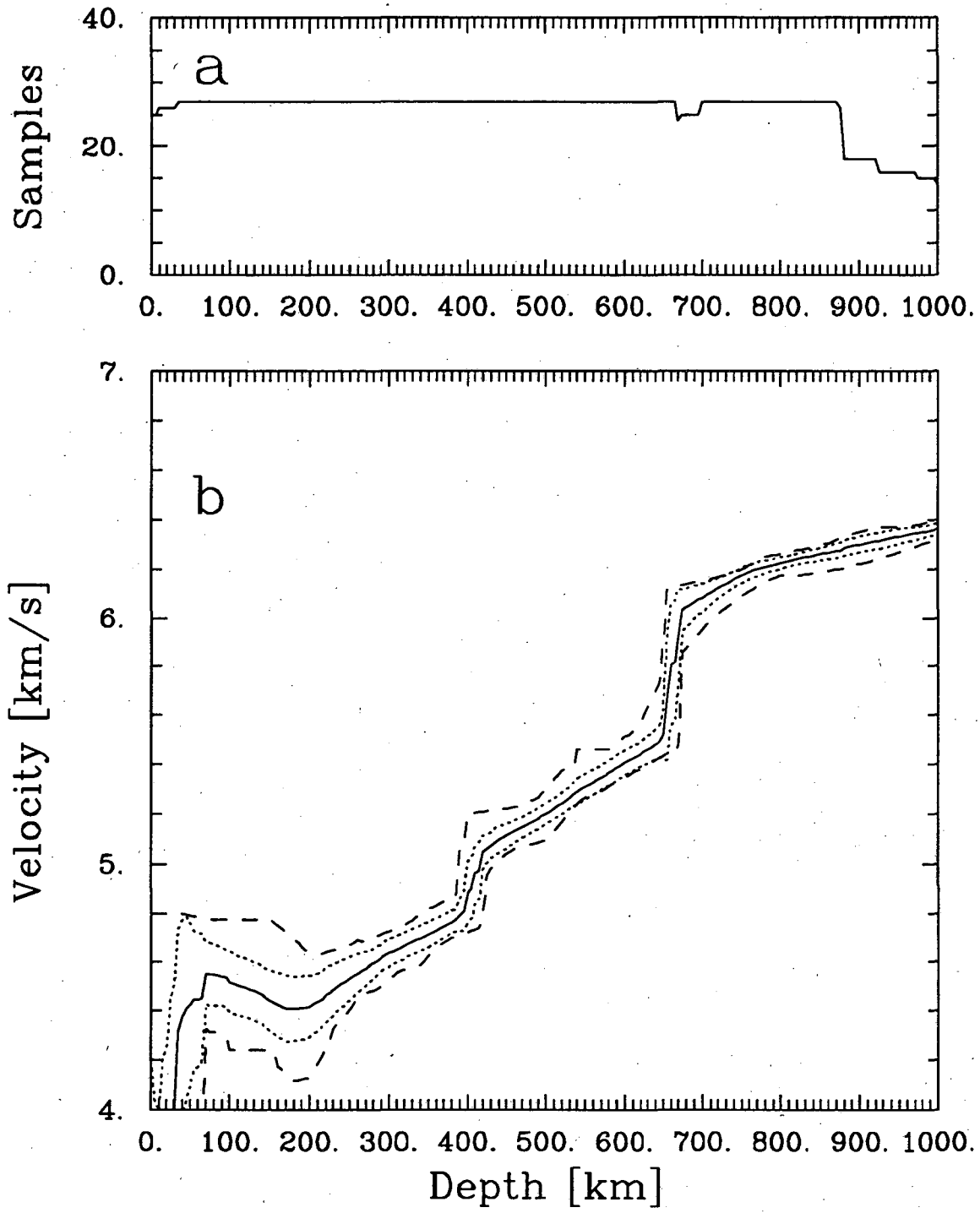
Fig. 2.3. Same as figure 2.2, but for S wave velocity.

mantle conditions.

The expected value of V_Φ and its variance in the upper mantle and transition zone is calculated from the mean and standard deviation of the V_P and V_S profiles through a formal propagation of errors. As shown in Figure 2.4, the results of this procedure are nearly identical to those recovered from a simulation of the probability distribution of V_Φ which used all possible combinations of the V_P and V_S profiles. This indicates that the statistical properties of V_Φ reported here are robust. Figure 2.5 compares the estimated mean and uncertainty of V_Φ with very recent global and high resolution, regional profiles. Our estimate agrees well with the observed profiles except in the uppermost mantle. This observation is not surprising in light of the fact this is the most variable region in the mantle as evidenced by the high level of uncertainty. Thus any deviation due to bias between our estimate and the true mean is probably insignificant compared to the error.

Below 900 km depth, the number of published velocity profiles decreases rapidly. Thus, in the lower mantle, I use the method of Bessonova et al. [1976] to invert tau estimates for the statistical properties of V_P and V_S. The tau estimates are calculated directly from traveltime data in the International Seismological Centre catalog [*Tralli and Johnson*, 1986; *Ita and Tralli*, Appendix A]. The mean and standard deviation of the profile calculated using this method agrees well with an average of the published profiles that extend throughout the depth range of the lower mantle (Figure 2.6). It should be noted that the lower 560 km of the mantle is not resolved by the tau method because of contamination of the S wave traveltime curve by SKS arrivals. This is not of concern however. Anomalous velocity gradients have often been observed in this region (see *Lay and Young*, [1986]). These gradients are symptomatic of possible non-adiabatic temperature gradients and changes in bulk composition, which I do not attempt to explain here.

To fully represent the statistical properties of the expected lower mantle seismic profiles, I include the covariance for both density and bulk sound velocity. The covariance matrix, Λ, is given by

$$\Lambda_{ij} = \frac{1}{N}\sum_{k=1}^{N}(x_{ik}-\bar{x}_i)(x_{jk}-\bar{x}_j), \qquad\qquad 2.1$$

where x_{ik} is the value at the ith depth point of the kth density or velocity profile and $\bar{x}_i$ is the mean value at that depth. For density, the covariance matrix was calculated using the same set of profiles
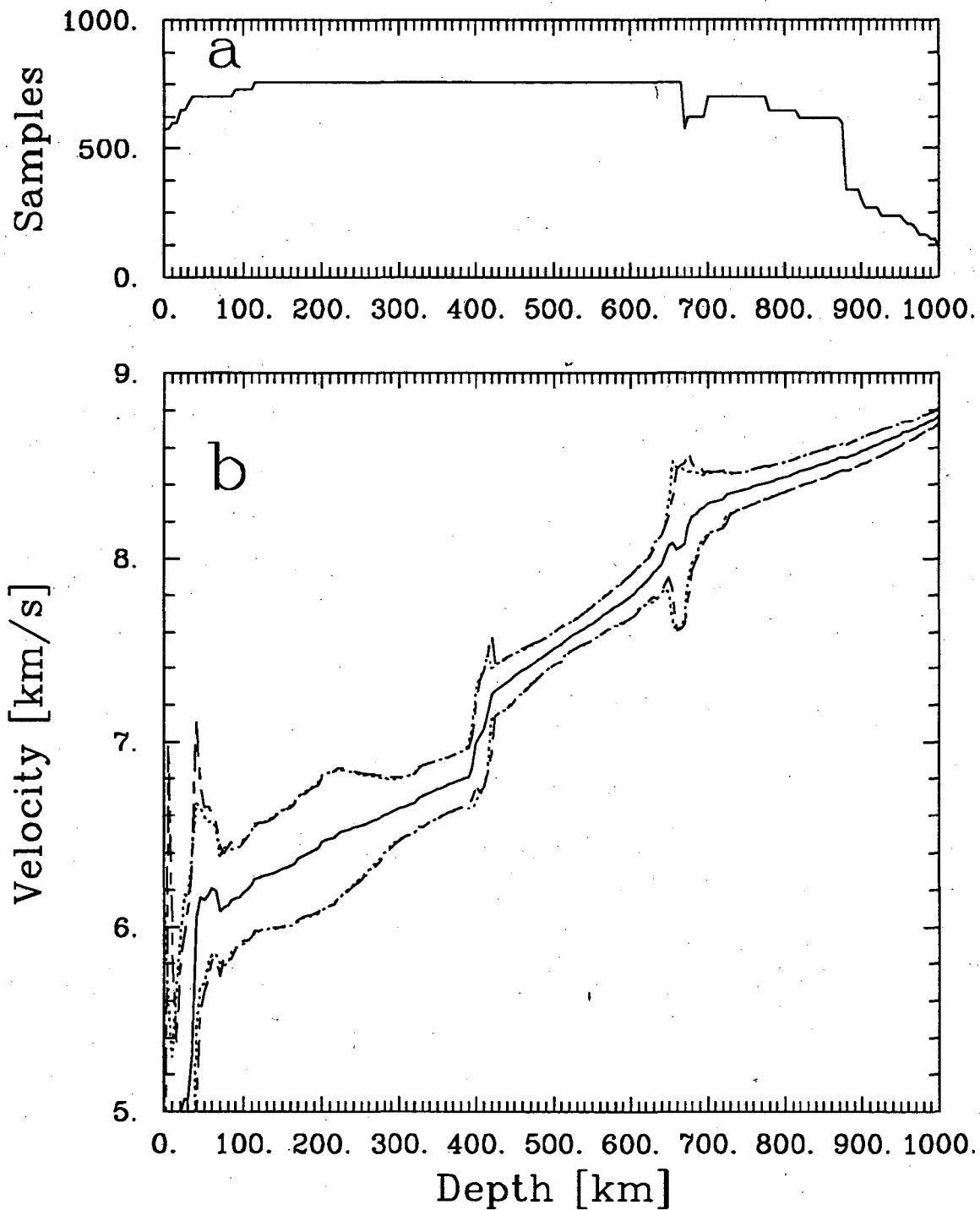
Fig. 2.4. a) Number of bulk sound velocity profiles calculated from all possible combinations of the P and S wave profiles used in the analysis. b) Mean (solid line), standard deviation calculated from the propagation of errors (dotted line), and standard deviation (dashed line) calculated from the ensemble of profiles generated from the P and S wave velocity distributions.
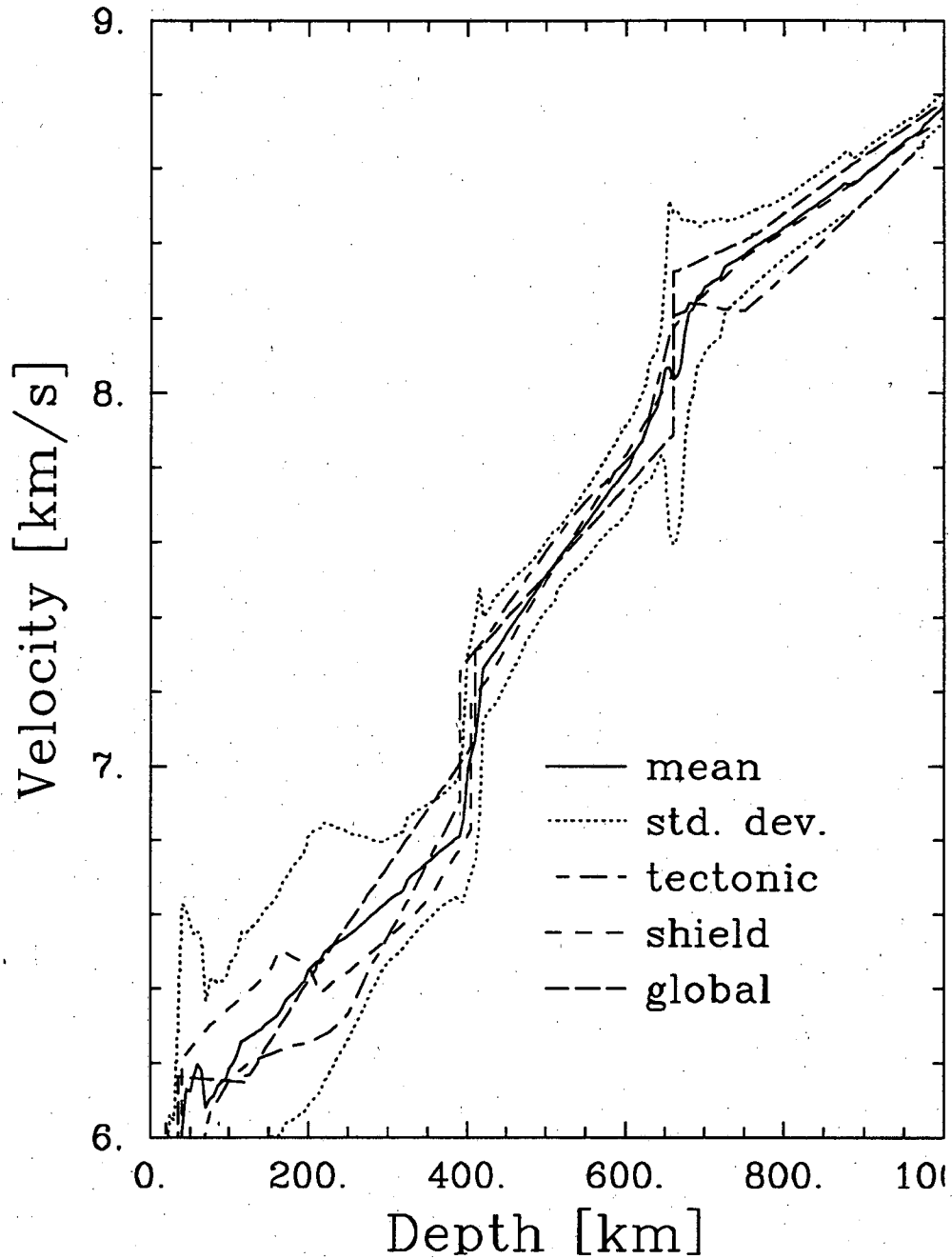
Fig. 2.5. Mean and standard deviation of bulk sound velocity compared to individual curves observed in the Earth. The tectonic profile representative of tectonically active regions is calculated from the P wave profile of *Walck* [1984] and the tectonic S wave profile of *Grand and Helmberger* [1984]. The shield profile representative of cratonic regions is calculated from the P - wave model of *Lefevre and Helmberger* [1989] and the shield S - wave model of *Grand and Helmberger* [1984]. The global model is calculated from the average P and S wave models of *Kennett and Engdahl* [1991].
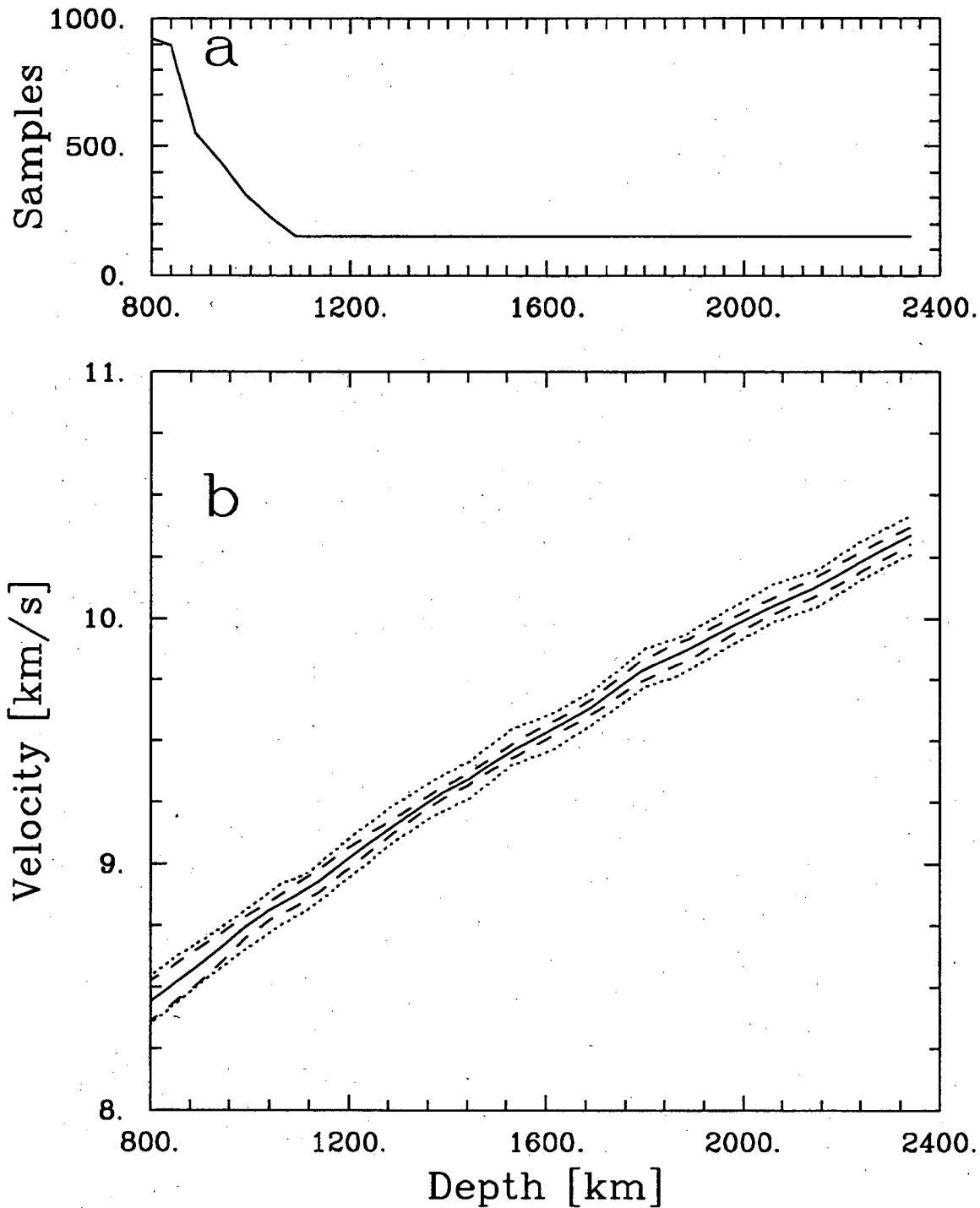
Fig. 2.6. a) Number of lower mantle bulk sound velocity profiles calculated from all possible combinations of the P and S wave profiles used in the analysis. b) Mean (solid line), standard deviation calculted from the tau analysis (dotted line), and standard deviation (dashed line) calculated from the ensemble of profiles generated from the P and S wave velocity distributions.

described above. For the bulk sound velocity, I used the variance given by the tau method to represent the on-diagonal terms of the matrix. The off-diagonal terms are derived from a statistical analysis of the 11 V_P and V_S profiles available in the lower mantle. Correlation matricies represented in Figures 2.7 and 2.8 illustrate the importance of covariance. The errors in V_Φ are virtually independent of one another according to this estimate. Density errors are strongly correlated however. As we shall see in Chapter 5, this correlation can have a strong influence on the inferences one can make about mantle composition.
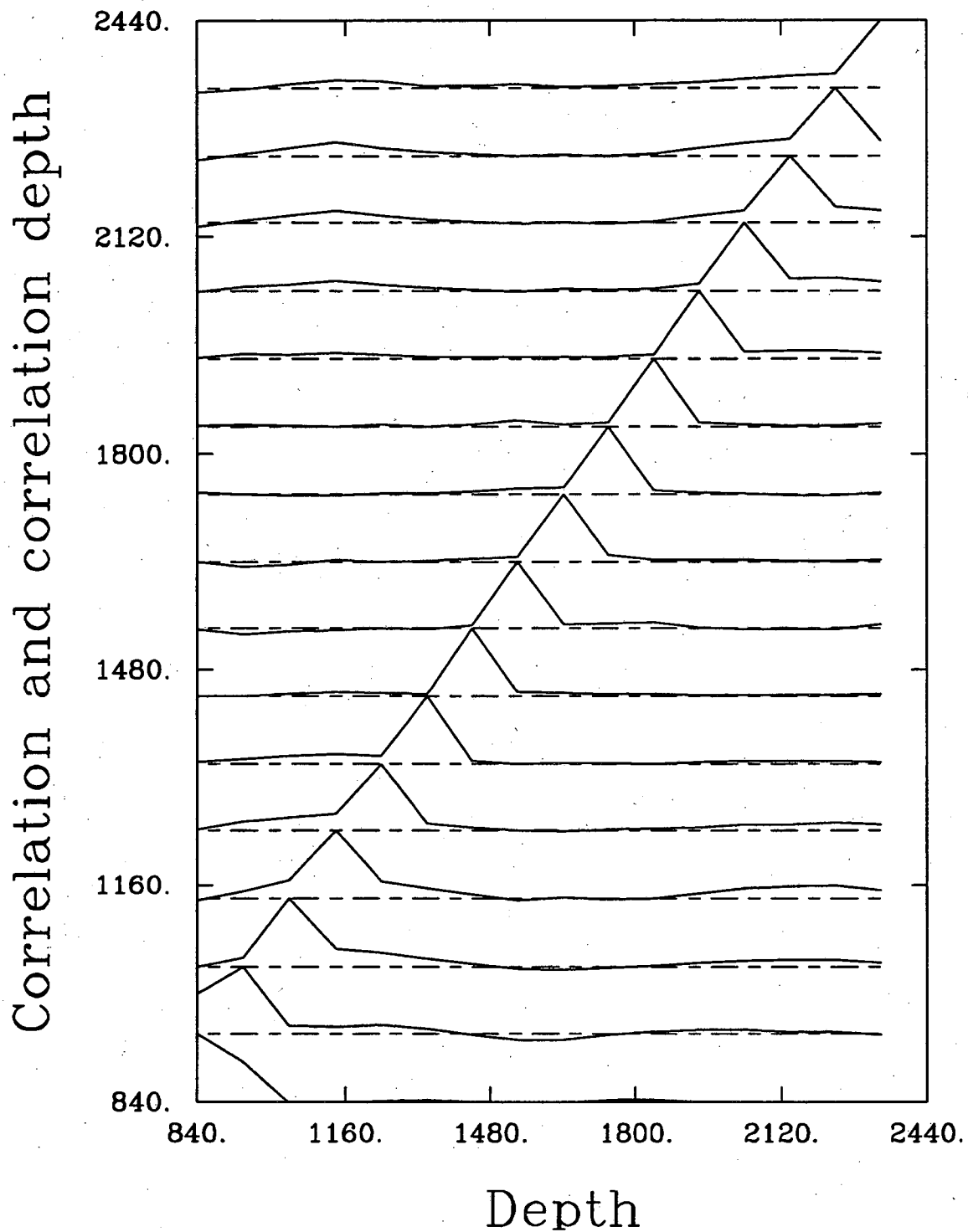
Fig. 2.7. Correlation matrix for bulk sound velocity. Depth of the velocity parameter (dashed line) to which all velocity-depth are correlated with and the correlation cofficient (solid line) is given on the y-axis. Depth at which the correlation is evaluated is given on the x-axis. The value of the correlation can range from -1 to 1 with the correlation depth (dashed line) representing a value of 0.
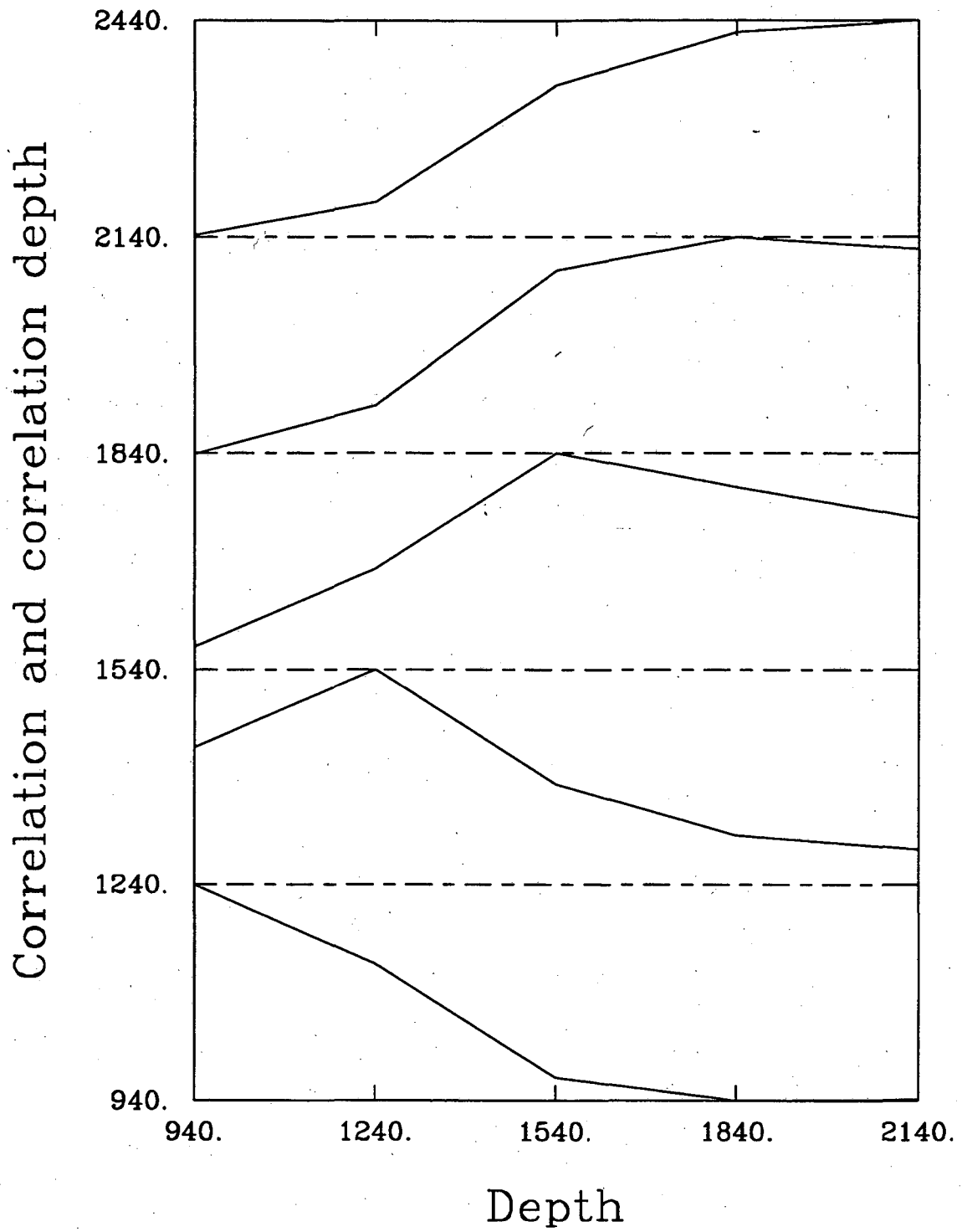
Fig. 2.8. Same as Figure 2.7, but for density.

Chapter 3

Compositional Models and Phase equilibria

3.1 Origin of Models

Our knowledge of the chemical composition of the Earth's interior is derived from two major sources. The first and most reliable source comes from surface samples of mantle material. Mantle rocks are usually found as xenoliths in ultramafic kimberlites which are volcanic in origin or as bodies in thrust sheets brought to the surface by tectonic forces [Ringwood, 1979; Haggerty and Sautter, 1991]. These samples are thought to originate at less than 180 km depth, although deeper samples may have been found recently [Haggerty and Sautter, 1991]. The second source comes from the composition of meteoritic carbonaceous chondrites. High volatile contents and near solar ratios of refractory elements indicate that chondrites represent primitive solar nebula material from which the terrestrial planets formed [Anderson, 1989]. Agreement in the elemental abundances between chondrites and mantle nodules indicate that the composition of the mantle may be well represented by samples from its uppermost regions.

The major oxide contents of the three upper mantle compositions considered here are shown in Table 3.1. Composition A is that of pyrolite. Pyrolite was first proposed by Ringwood [1962] based on observations of the bulk chemistry of basalt and peridotite, a rock type thought to originate in the uppermost mantle. He noted that the elemental partitioning between the two is complementary suggesting that they could represent the partial melt product and residuum of some "parent" mantle material (pyrolite). Due to the increased understanding of the phase equilibria of basaltic rocks and bulk Earth composition, pyrolite has undergone a slow evolution over time [Ringwood, 1975; Irifune, 1987]. Composition A represents the most recent version of pyrolite as defined by Irifune [1987].

Composition B is the model deduced from the preferred phase assemblage of Duffy and Anderson [1989]. The model was developed based on the comparison of V_P and V_S predicted by combinations of possible mantle minerals as explained in chapter 1. Their preferred assemblage was chosen due to its

	Composition (mole %)			
	A	B	C	Harz
SiO_2	38.59	41.94	39.82	36.23
MgO	49.09	42.32	42.77	57.38
FeO	6.24	5.30	5.35	5.44
CaO	3.25	8.67	8.76	0.44
Al_2O_3	2.20	1.78	3.30	0.32
Na_2O	0.33	-	-	.01
Cr_2O_3	0.15	-	-	0.17
Ti_2O	0.14	-	-	0.01
$\frac{100\times MgO}{MgO+FeO}$	88.72	88.88	88.88	91.35
$(Mg,Fe)_2SiO_4$ wt%	62	40	40	82
Si#	3.23	3.46	3.26	3.17

TABLE 3.1. Molar percents of major oxides for the mantle compositions and harzburgite. Si# is number of Si atoms per every 12 O atoms.

optimal fit to the transition zone. It is important to note that the derivation of this composition relied heavily on estimates of the shear modulus whose pressure and temperature dependence was based almost exclusively on systematics.

Composition C is an aluminum enriched version of B and is similar to piclogite compositions defined by *Bass* and *Anderson* [1984] and *Anderson* and *Bass* [1984]. Piclogite is an olivine enriched eclogite, a high pressure form of basalt which is rich in sodium and aluminum. It was proposed as an alternative model to pyrolite based on the high eclogite content of some mantle xenoliths. *Schulze* [1989] concluded that the actual amount of eclogite in the upper mantle is insignificant, but I include it in this study for completeness.

Significant chemical variation has also been noted to occur in the oceanic lithosphere and thus will have a strong affect on the mineralogical evolution of subduction zones. A petrologic model of the oceanic lithosphere is shown in Figure 3.1. The oceanic crust is composed of basalt formed from the partial melting of mantle material upwelling at spreading ridges. The residuum left from this partial melting event is contained in the underlying olivine-rich harzburgite layer. Below the harzburgite lies a lherzolite layer which represents the transition from the residuum to the normal mantle material. Here I wish to consider only the large spatial scale length effects of chemical heterogeneity and thus ignore the oceanic crust. The oxide composition of harzburgite is given in Table 3.1. The composition in the lherzolite layer is assumed to grade linearly from the harzburgite to that of the mantle.

3.2   Phase Equilibria

To fully exploit phase equilibrium data on pseudo-binary systems, I assume that these bulk compositions can be divided into two subsystems, olivine and the remainder (residuum), which do not affect each other's phase equilibria [*Jeanloz* and *Thompson*, 1983; *Irifune*, 1987]. This is consistent with the results of *Akaogi* and *Akimoto* [1979] which show no change in the relative proportions of these two subsystems to at least 20 GPa.

I base the form of the $(Mg,Fe)_2SiO_4$ phase diagram on the experiments of *Ito and Takahashi* [1989], and *Katsura and Ito* [1989] (Figure 3.2). These data along with the thermochemical calcula-
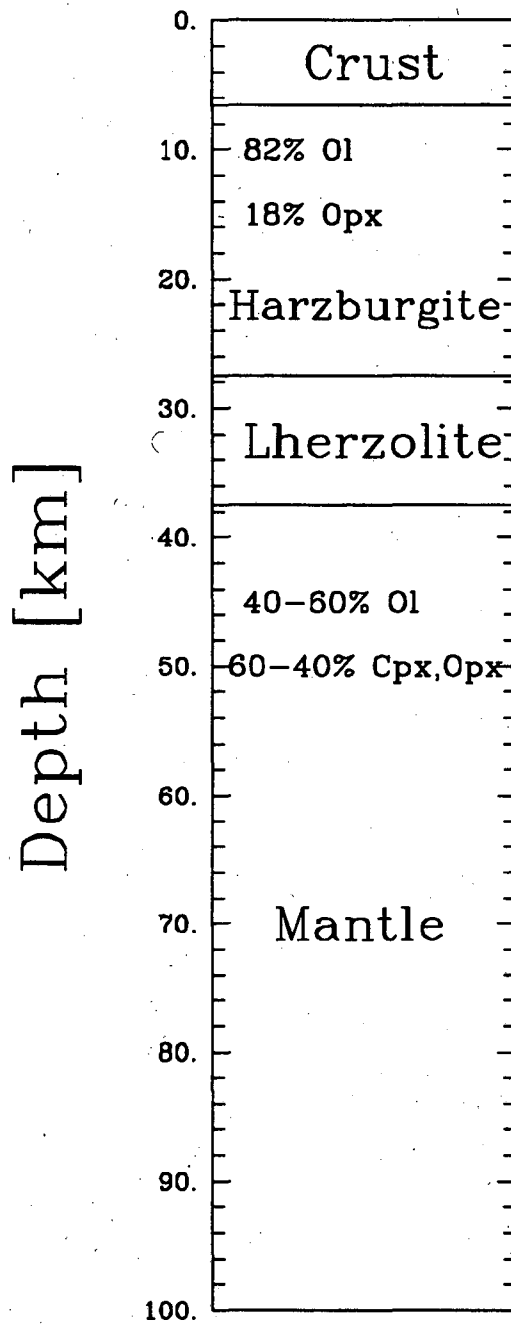
Fig. 3.1. Petrological model of the oceanic lithosphere (Adapted from *Ringwood*, 1982; *Irifune and Ringwood*, 1987b)
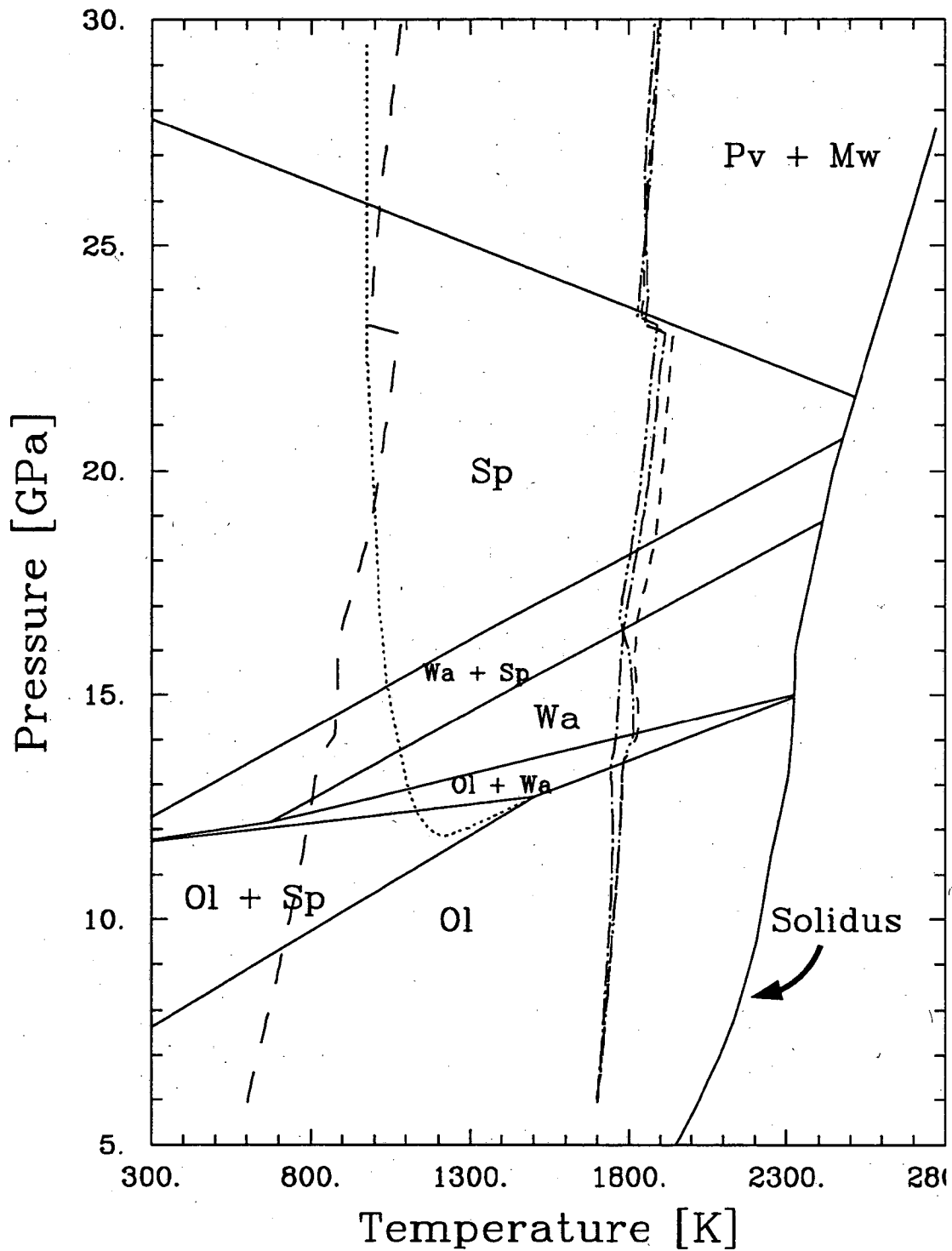
Fig. 3.2. (Mg,Fe)$_2$SiO$_4$ phase diagram. The mantle solidus is from *Ito and Takahashi* [1987] and *Gasparik* [1990]. The 1700 K adiabats of compositions A (short - dashed line), B (dash - double dotted line), and C (dash - dotted line) are superimposed as well as the geotherm of the cold core of the subducting slab model (long - dashed line) (see text and Figure 5.1).

tions of *Akaogi et al.* [1989], *Wood* [1990], and *Fei et al.* [1991] provide tight constraints on the relevant phase boundaries (precision of ± 0.5 GPa) throughout the pressure-temperature range considered here. Recently, much attention has also been given to the kinetic hindrance of phase transitions in the olivine system at low temperatures. *Kirby et al.* [1991] find the metastable behavior of olivine proposed by *Sung and Burns* [1976] provides a convincing explanation for the variation in the maximum depth of earthquakes between different subduction zones. Because of its apparent relevance to the Earth, I include the kinetic boundary of *Sung and Burns* [1976] in this analysis. Given that their magnesium to iron ratios are nearly identical, I use the same phase diagram for all compositions.

Phase diagrams in the residuum component (Figures 3.3-4) are primarily constrained by measurements on the Mg, Fe, and (Ca,Mg) pyroxene-garnet joins up to 20 GPa reviewed by *Akaogi et al.* [1987], the enstatite-pyrope join from 24 to 27 GPa [*Kanzaki*, 1987; *Irifune and Ringwood*, 1987a] and direct observation of pyrolite and harzburgite residuum at 1200 C and 1300 C, respectively, throughout the pressure range considered here [*Irifune and Ringwood*, 1987a,b]. These data encompass the major element chemistries of the compositions considered here (Table 3.2).

Mantle Residuum. The coexistence field of pyroxene and garnet is perturbed slightly from its location on the enstatite-pyrope join by the competing effects of Ca and Fe substitution. Because the residua components of the compositions have more Ca than Fe (Table 3.2), I have raised the pyroxene+garnet to garnet boundary above that in the magnesium end-member by 1 GPa, based on linear interpolation of the results of *Akaogi et al.* [1987]. Compared with compositions A and C, the lower Al content of B raises the boundary slightly and reduces its temperature dependence [*Akaogi et al.*, 1987]. The estimated boundaries are consistent with the whole rock experiments of *Irifune* [1987], *Irifune and Ringwood* [1987b], and *Takahashi and Ito* [1987].

I assume that the formation of Ca-perovskite is not strongly dependent on bulk composition and base the garnet to garnet + Ca-perovskite transition on observed transitions in diopside and hedenbergite. Ca-perovskite first forms at 17 GPa in diopside [*Irifune et al.*, 1989; *Tamai and Yagi*, 1989] and at somewhat higher pressures in more Fe rich compositions [*Kim et al.*, 1989]. Assuming that Fe has a linear effect on the appearance of Ca-perovskite, I place the garnet to garnet + Ca-perovskite transition
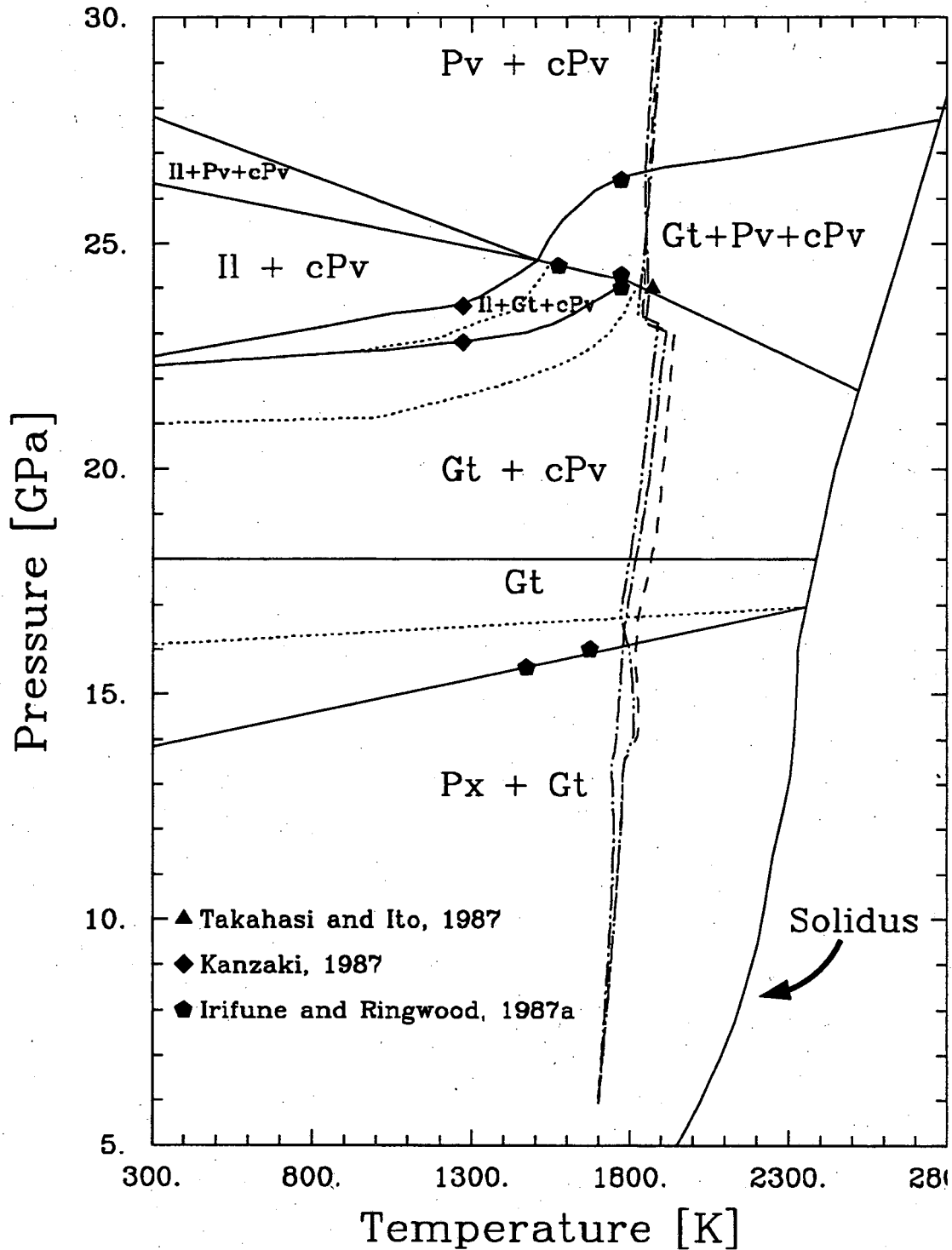
Fig. 3.3. Mantle residuum phase diagram. Symbols present experimental observations of phase boundaries. Solid lines represent phase boundaries in compositions A and C. Where composition B differs from the other two, its phase boundaries are represented by dotted lines. Mantle solidus and the superimposed adiabats are the same as in Figure 3.2. Px = Opx + Cpx; Gt = Py + Gr + Maj + Ca-Maj.
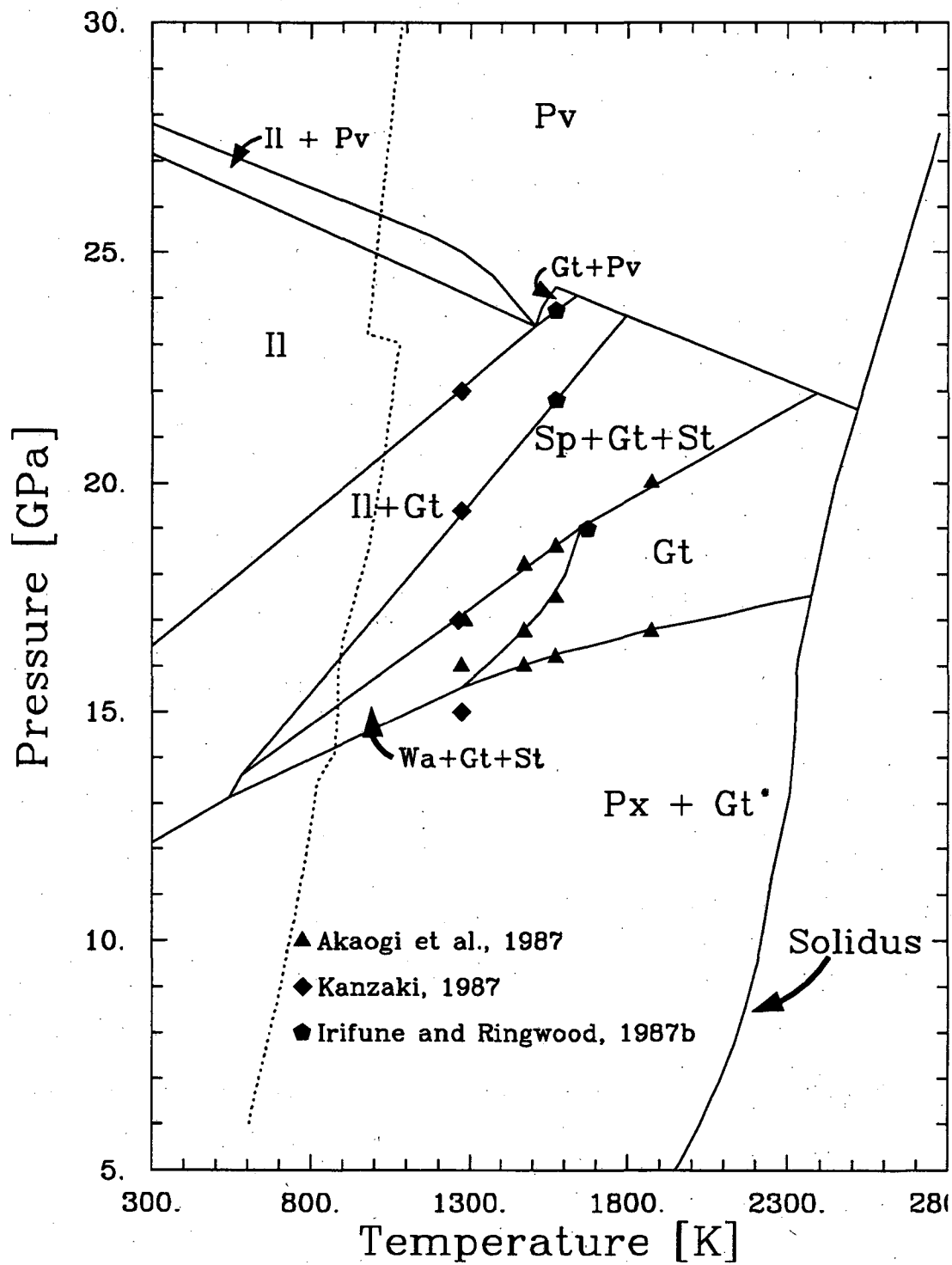
Fig. 3.4. Harzburgite residuum phase diagram. Symbols present experimental observations of phase boundaries. Mantle solidus is the same as in Figure 3.2. The dashed line represents the geotherm for the cold core of the subducting slab model. Px = Opx + Cpx; Gt = Py + Gr + Maj + Ca-Maj.

| | Residuum Composition (mole %) | | | |
	A	B	C	Harz
SiO$_2$	48.60	48.39	44.81	48.51
MgO	29.93	29.64	29.50	41.49
FeO	3.82	3.71	4.34	4.25
CaO	9.45	15.17	15.50	2.70
Al$_2$O$_3$	5.84	3.11	3.30	1.92
Na$_2$O	0.95	-	-	.03
Cr$_2$O$_3$	0.44	-	-	1.05
Ti$_2$O	0.42	-	-	0.05
Si#	3.58	3.76	3.43	3.90

TABLE 3.2. Molar percents of major oxides in the residuum system of the mantle compositions and harzburgite. Si# is number of Si atoms per every 12 O atoms.

at 18 GPa. This estimate is consistent with observations of pyrolite residuum by *Ito and Takahashi* [1987a] and *Irifune* [1987] and of complete pyrolite by *Takahashi and Ito* [1987]. These experiments indicate that the boundary is insensitive to temperature.

Above 18 GPa, the estimated phase boundaries are identical to those in the enstatite-pyrope system as determined by *Kanzaki* [1987] and *Irifune and Ringwood* [1987a]. This is supported by the observed garnet + Ca-perovskite to garnet + (Mg,Fe)-perovskite + Ca-perovskite boundary in pyrolite residuum [*Ito and Takahashi*, 1987a; *Irifune and Ringwood*, 1987b] which agrees with the garnet to garnet + (Mg,Fe)- perovskite boundary on the enstatite-pyrope join [*Irifune and Ringwood*, 1987a]. The inferred formation of ilmenite from pyrolite residuum [*Irifune and Ringwood*, 1987b] also agrees with the estimated phase boundaries. Compared with A and C, the lower Al content of B extends the stability of ilmenite to slightly higher temperatures. The assumed lower mantle assemblage is in excellent agreement with very high pressure (25-84 GPa) determinations of peridotite phase equilibria [*O'Neill and Jeanloz*, 1990].

Harzburgite Residuum. Given that the relative abundances of Ca and Fe are about equal in harzburgite, the phase relations along the enstatite-pyrope join to 22 GPa are used. This assumption is corroborated by the study on harzburgite residuum by *Irifune and Ringwood* [1987a]. The upper boundary for the pure ilmenite phase is based on the the ilmenite to perovskite phase transition given by *Ito and Takahasi* [1989]. An ilmenite + perovskite phase field is inserted based upon the phase relations shown by *Irifune and Ringwood* [1987a]. The lower boundary for pure perovskite is also taken from *Ito and Takahasi* [1989] for the spinel to perovskite phase transition. This boundary should be well constrained because the stoichiometry of the olivine component changes at this point. Thus, one can no longer consider the system as two separate components. Dilution of the olivine component with the residuum component in harzburgite has little effect on the transition to perovskite + magnesiowüstite but the same is not true for normal mantle material [*Irifune and Ringwood*, 1987a]. There, the presence of aluminum rich material stabilizes garnet to higher pressures (Figure 3.3).

It is interesting to note that the geotherm for the cold core of the slab indicated by the dashed line in Figure 3.4 lies well below the experimental data for most of the pressure range considered. This

fact coupled with the scarcity of data at higher pressures could mean that the phase boundaries could be in error by ± 2 to ± 4 GPa or more in poorly constrained regions. In relatively well constrained regions, the error should be about ± 1 GPa assuming it is the same order as the referenced data.

3.3   Determination of Mineral Proportions

Based on the results of *Akaogi and Akimoto* [1977], olivine and residuum systems are assigned identical bulk Fe contents. In the olivine system, volume fractions of coexisting phases vary linearly from the lower single phase field to the upper one [*Irifune*, 1987; *Weidner and Ito*, 1987]. The exception is the olivine + spinel field. Here it is assumed that the amount of spinel grades from 0% at the bottom boundary to a variable percentage at the top boundary that depends linearly on temperature. At 273 K, spinel is assumed to comprise 100% of a given volume of rock. At 1500 K, it contributes nothing. At the upper boundary, the spinel phase portion converts instantaneously to the wadsleyite phase and the remaining olivine converts to wadsleyite as one moves to the upper boundary of the olivine + wadsleyite field. The Mg-Fe partition coefficient between magnesiowüstite and perovskite is calculated using the reference Helmholtz free energies and interaction parameters of these minerals according to the procedure outlined in *Stixrude and Bukowinski* [1992].

In the residuum component, volume fractions and Al contents of coexisting pyroxene and garnet are taken from the phase diagrams of *Akaogi et al.* [1987], which are consistent with the results of *Irifune and Ringwood* [1987a,b]. I ignore the effects of Al on the properties of enstatite since only minor amounts (less than 1 %) are soluble at the pressures of interest here. Pressure- and temperature-independent Mg-Fe partition coefficients between pyroxene and garnet are taken from *Akaogi and Akimoto* [1979]. Proportions for the spinel + stishovite + garnet field are based on the experiments of *Irifune and Ringwood* [1987a]. The wadsleyite + stishovite + garnet field is not observed by them because of their high experimental temperatures, but it is assumed to display the same volume ratios as the spinel + stishovite + garnet field. In the ilmenite + garnet phase field, the composition changes completely from garnet to ilmenite where it is overlain by the ilmenite field. From the point where the ilmenite field pinches out to where the ilmenite + garnet field does the same, the amount of ilmenite present at the upper boundary decreases from 100% to nothing. The results of *Irifune* [1987] and

Irifune and Ringwood [1987a,b] on pyrolite and harzburgite compositions determine the amount of Ca-perovskite. Volume fractions of coexisting garnet and perovskite are determined by the phase diagram of *Irifune and Ringwood*, [1987a]. In the absence of data, I have assumed an Mg-Fe-Al partition coefficient of unity between garnet and (Mg,Fe,Al)-perovskite.

Chapter 4

Theoretical Prediction of Mantle Properties

4.1 The Thermodynamic Potential

Calculations of mineral elasticity and mantle adiabats are self-consistently based on semi-empirical thermodynamic potentials. The Gibbs free energy per formula unit, G, of a phase composed of a solid solution of N species as a function of pressure and temperature (P and T) can be expressed as:

$$G_i(P,T) = \sum_{j=1}^{N} x_{ij} [G_{ij}(P,T) + s_i RT \ln a_{ij}] \qquad (1)$$

where G_{ij}, x_{ij}, and a_{ij} are the molar Gibbs free energy, mole fraction, and activity of species j in phase i, s_i is the stoichiometric coefficient of the mixing site and R is the gas constant. Assuming symmetric solid solution behavior [e.g. *Guggenheim*, 1952]

$$RT \ln a_{ij} = RT \ln x_{ij} + W_i(1-x_{ij})^2 \qquad (1a)$$

where W_i is the interaction parameter assumed to be independent of pressure and temperature. The molar Gibbs free energy can be written as:

$$G_{ij}(P,T) = F_{ij}(V_{ij},T) + PV_{ij} \qquad (2)$$

where V_{ij} is the molar volume and F_{ij} is the molar Helmholtz free energy.

Following the development of Stixrude and Bukowinski [1990], F_{ij} can be divided into a reference term, a volume dependent part given by Birch-Murnaghan or Universal equations of state, and a thermal part given by Debye theory (subscripts ij understood)

$$F(V,T) = F_o + F_C(V,T_o) + [F_{TH}(V,T) - F_{TH}(V,T_0)] \qquad (3)$$

where the subscript o refers to zero pressure and temperature T_o. The cold part is given by

$$F_C(V) = 9K_o V_o (f^2/2 + a_1 f^3/3) \qquad (4a)$$

where

$$f = (1/2) [(V_o/V)^{2/3} - 1] \qquad (4b)$$

$$a_1 = (3/2)(K_o{'} - 4), \tag{4c}$$

for the Birch Murnaghan equation of state and by integration of the pressure volume relation proposed by *Vinet et al.* [1987] for the universal equation of state:

$$F_C(V) = \frac{9K_o V_o}{\eta^2}[1 + e^{\eta(1 - X)}(\eta - \eta X - 1)] \tag{4d}$$

where

$$X = (V/V_o)^{1/3} \tag{4e}$$

$$\eta = 3(K_o{'}-1)/2 \tag{4f}$$

Here, K_o and $K_o{'}$ are the isothermal bulk modulus and its first pressure derivative. The thermal part is given by:

$$F_{TH} = 9nRT(T/\theta)^3 \int_0^{\theta/T} ln\,(1 - e^t)t^2\,dt \tag{5a}$$

where n is the number of atoms per formula unit and θ is the Debye temperature, whose negative logarithmic volume derivative is the Grüneisen parameter, γ, which is assumed to have the form:

$$\gamma = \gamma_o(V/V_o)^q \tag{6}$$

where I assume q=1 ± 2 throughout, except in the case of $(Mg,Fe)SiO_3$ perovskite where this quantity has been measured [*Mao et al.*, 1991; *Stixrude et al.*, 1992].

The Helmholtz potential of species ij (3-6), most often seen in the form of the Mie-Grüneisen equation of state (subscripts ij on all material properties understood)

$$P = -(\partial F/\partial V)_T = P_C + (\gamma/V)[E_{TH}(V,T) - E_{TH}(V,T_o)] \tag{7}$$

where

$$P_C = 3K_o f\,(1 + 2f)^{5/2}(1 + a_1 f) \tag{8a}$$

using the Birch Murnaghan equation of state,

$$P_C = 3K_o \left(1 - \frac{X}{X^2}e^{\eta(1 - X)}\right) \tag{8b}$$

using the universal equation of state, and

$$E_{TH} = 9nRT(T/\theta)^3 \int_0^{\theta/T} t^3/(e^t - 1)\,dt, \tag{9}$$

has proved successful in reproducing a large body of thermodynamic data including equations of state,

heat capacities, unary phase equilibria and melting [*Shapiro and Knopoff*, 1969; *Knopoff and Shapiro,* 1969; *McQueen et al.*, 1970; *Jeanloz*, 1989; *Stixrude and Bukowinski*, 1990].

The Gibbs potential (1) is expressed in terms of its natural variables and thus contains all thermodynamic information about the model system; it is a fundamental thermodynamic relation in the terminology of *Callen* [1985]. All thermodynamic properties are given by pressure and temperature derivatives of (1). The potential formulation has important advantages over partial descriptions such as the equation of state (P-V-T relation) which contains no information about entropy. In addition to complete self-consistency between calculated densities, bulk sound velocities and mantle adiabats, the thermodynamic potentials used here generally require a small number of parameters since they are physically based. This allows us to constrain each parameter independently by a large number of experimental measurements. In contrast, perturbative schemes, either simple polynomials in pressure and temperature or more complex forms [*Plymate and Stout*, 1989 and references therein; *Akaogi et al.*, 1989; *Duffy and Anderson*, 1989; *Fei et al.*, 1991], generally require an additional, often poorly constrained parameter for each higher-order derivative property such as the temperature dependence of the bulk modulus or the pressure dependence of the thermal expansivity. The temperature derivative of the bulk modulus, for instance, which is unmeasured for nearly all mantle minerals, does not appear explicitly in our formulation but is determined by θ_o and γ_o, which are constrained by heat capacity and thermal expansivity data.

4.2   Calculation of density and elasticity

Due to the paucity of data for most mineral solutions of interest and the to simplicity of the resulting equations, I assume ideal behavior for all of the thermodynamic properties of interest here (first and higher order pressure and temperature derivatives of G). This is accomplished by setting the W_i equal to zero. As mentioned above, the W_i are used in the expression for G when calculating the partitioning of magnesium and iron between perovskite and magnesiowüstite.

Deviations from ideality are well documented in silicates [e.g. *Saxena*, [1973], but the effects on properties deduced from seismic observations are small compared with other uncertainties in mineralogical and seismic data. The deviation of molar volumes from ideal behavior at zero pressure (as much

as 0.2 %) is similar to the precision of high pressure volume determinations and substantially smaller

than the uncertainties in observed mantle densities (see the review of *Jeanloz and Thompson* [1983] and

the more recent work of *Hazen et al.* [1990] and *Mao et al.* [1991] on Mg-Fe solutions, *Ohashi and*

Finger [1975] and *Ohashi et al.* [1975] on the effect of Ca and the discussion of the molar volumes of

garnet-majorite solutions below). Available data on the bulk modulus of intermediate compositions

considered here are consistent with ideal behavior [*Jeanloz and Thompson*, 1983; *Richet et al.*, 1989;

O'Neill et al., 1989; *Hazen et al.*, 1990]. Excess entropies of mixing are much smaller than the ideal

mixing term in Mg-Fe solutions [e.g. *Wood and Kleppa*, 1981] but can be of comparable magnitude if

the radii of cations occupying the mixing site differ substantially (Ca-Mg solutions) [*Haselton and*

Newton, 1980]. Mixing entropies are smaller than entropy changes associated with phase transitions

and contribute less than 1.2 % to the total entropy. In general, variations in the entropy of mixing have

a small effect on the properties considered here, since their only influence is through slight changes in

adiabatic temperatures.

The entropy (S), heat capacity at constant volume (C_V), thermal expansivity (α), and isothermal

bulk modulus of species ij are given directly by the Helmholtz potential (subscripts ij on all material

properties understood)

$$S = -(\partial F/\partial T)_V = 9nRT(T/\theta)^3 \int_0^{\theta/T} [t/(e^t - 1) - \ln(1 - e^{-t})]t^2 dt \qquad (10)$$

$$C_V = -T(\partial^2 F/\partial T^2)_V = 9nRT(T/\theta)^3 \int_0^{\theta/T} e^t t^4 dt/(e^t - 1)^2 \qquad (11)$$

$$\alpha = -(\partial^2 F/\partial V \partial T)/K = \gamma C_V/KV. \qquad (12)$$

$$K = V(\partial^2 F/\partial V^2) = K_C + 9a_1 f^2] + (\gamma/V)[\gamma + 1 - q][E_{TH}(V,T) - E_{TH}(V,T_o)] - \qquad (13)$$
$$(\gamma^2/V)[TC_V(V,T) - T_o C_V(V,T_o)]$$

where, for the Birch Murnaghan equation of state,

$$K_C = K_0(1 + 2f)^{5/2}[1 + (7 + 2a_1)f + 9a_1 f^2] \qquad (13a)$$

and, for the universal equation of state,

$$K_C = (K_0/X^2)[2 + (\eta - 1)X - \eta X^2]e^{\eta(1 - X)} \qquad (13b)$$

The molar volume, isothermal bulk modulus, thermal expansivity, heat capacity, entropy, and adi-

abatic bulk modulus (K_S) of a mineral solid solution at a given pressure and temperature are also given

directly by the thermodynamic potentials. Using the expressions for the corresponding properties of the individual species j (2-12) and assuming ideality, we have (subscript i on all material properties understood)

$$V = (\partial G/\partial P)_T = \sum_{j=1}^{N} x_j V_j \tag{14}$$

$$K = -V/[(\partial^2 G/\partial P^2)_T] = V/(\sum_{j=1}^{N} x_j V_j/K_j) \tag{15}$$

$$\alpha = (\partial^2 G/\partial P \partial T)/V = (\sum_{j=1}^{N} x_j V_j \alpha_j)/V \tag{16}$$

$$C_V = -T(\partial^2 F/\partial T^2)_V = \sum_{j=1}^{N} x_j C_{Vj} \tag{17}$$

$$S = -(\partial G/\partial T)_P = \sum_{j=1}^{N} x_j S_j - sRx_j \ln x_j \tag{18}$$

$$K_s = K(1 + KTV\alpha^2/C_V) \tag{19}$$

Mineral properties are combined to calculate ρ, entropy and bulk sound velocity of mantle compositions. I use the Voight-Reuss-Hill method [*Watt et al.*, 1976] to determine the bulk modulus of the poly-phase aggregate, resulting in tight bounds on V_ϕ ($\pm$ 0.35% on average). The assumption that aggregates are isotropic and homogeneous, inherent in this, as well as other, more restrictive bounding schemes [e.g. *Hashin and Shtrikman*, 1963; see *Watt et al.*, 1976 and *Salerno and Watt*, 1986] is unlikely to significantly bias our comparisons with seismic data. Tomographic studies of the transition zone and lower mantle show that anisotropy is small or unresolvable in these regions [*Montagner and Tanimoto*, 1991] and studies of scattering attenuation show that inhomogeneities on the scale length of long period seismic waves (10-100 km) are small below 200 km [*Korn*, 1988]. Entropy and ρ for the aggregate are calculated by summing the molar properties of each individual mineral multiplied by the number of moles of that mineral present in the aggregate.

4.3   Determination of initial parameters

The model parameters for mantle species are given in Table 4.1. The molar volumes of most minerals are directly measured by x-ray diffraction, while those of fictive Fe end-members (Fe-wadsleyite, Fe-perovskite) are determined by measurements along the Mg-Fe join. The molar volumes of magnesium, iron, and calcium majorites were simultaneously inverted for using the diffraction data

TABLE 4.1 Parameters of the Thermodynamic Potential

Name	Formula	Abbrv	V_0^a (cc/mol)	K_0 (GPa)	K_0'	θ_0 (°K)	γ_0
Forsterite	Mg_2SiO_4	Ol	43.76	128[1,2]	5.0[1,3]	924[4,5]	1.14[4,5]
Fayalite	Fe_2SiO_4		46.27	127[6]	5.2[6,7]	688[8,9]	1.08[8,9]
Wadsleyite	Mg_2SiO_4	Wa	40.52	174[10]	4.0[11](4.8)[12]	974[5,13]	1.32[5,13]
	Fe_2SiO_4		43.22	174[14,b]	4.0[14,b](4.8)[b]	771[c]	1.32[b]
Spinel	Mg_2SiO_4	Sp	39.65	183[15]	4.1[16](5.0)[17]	1017[5,18]	1.21[5,18]
	Fe_2SiO_4		42.02	192[19]	4.1[20](5.0)[b]	805[9,18]	1.52[9,18]
Enstatite	$MgSiO_3$	Opx	31.33	106[21]	5.0[22,23]	935[24,25]	0.97[24,25]
Ferrosilite	$FeSiO_3$		32.96	101[26]	5.0[b]	676[9,27]	0.98[9,27]
Diopside	$CaMgSi_2O_6$	Ca-cpx	66.11[28]	114[29]	4.5[30]	941[25,28]	1.06[25,28]
Hedenbergite	$CaFeSi_2O_6$		67.84[31]	120[32]	4.5[b]	845[d,21,32]	0.95[31]
Pyrope	$Mg_3Al_2Si_3O_{12}$	Py	113.19	173[33]	3.8[34]	981[35,36]	1.24[35,36]
Almandine	$Fe_3Al_2Si_3O_{12}$		115.23	177[37]	4.0[e]	909[f,37]	1.06[38]
Grossular	$Ca_3Al_2Si_3O_{12}$	Gr	125.30[38]	168[37]	4.5[39]	904[40]	1.05[38]
Majorite	$Mg_4Si_4O_{12}$	Maj	114.15[g]	151[41] (173)[42]	4.0[e] (4.9)[22]	949[f,37,41]	1.24[h]
	$Fe_4Si_4O_{12}$		117.70[g]	146[i] (168)[i]	4.0[e] (4.9)[22]	820[f,i,37]	1.24[h]
Ca-Majorite	$Ca_4Si_4O_{12}$	Ca-maj	127.57[g]	135[i] (155)[i]	4.0[e] (4.9)[22]	850[f,i,37]	1.24[h]
Ilmenite	$MgSiO_3$	Il	26.35	212[43]	4.3[22]	1026[44]	1.48[44]
	$FeSiO_3$		26.85	212[b]	4.3[b]	753[j,k,43]	1.48[b]
Perovskite	$MgSiO_3$	Pv	24.46	263[45] ± 4	3.9[45] ± 0.3	1017[46,47] ± 4	1.96[46,47] ± 0.05
	$FeSiO_3$		25.49	263[b,48] ± 6	3.9[b,48] ± 0.4	749[k,l,49] ± 50	1.96[b] ± .25
Al-perovskite	$Mg_{3/4}Al_{1/2}Si_{3/4}O_3$	Al-Pv	24.84[50]	259[m] ± 10	3.9[b] ± 0.6	1010[l,n,49] ± 50	1.96[b] ± 0.25
	$Fe_{3/4}Al_{1/2}Si_{3/4}O_3$		25.87[50]	248[m] ± 10	3.9[b] ± 0.6	833[l,n,49] ± 50	1.96[b] ± 0.25
Ca-perovskite	$CaSiO_3$	Ca-Pv	27.27[51]	301[51] ± 12	3.8[51] ± 0.4	917[l,n,49] ± 50	1.96[b] ± 0.25
Periclase	MgO	Mw	11.25	160.4[52] ± 0.2	4.1[52] ± 0.1	777[4,40] ± 5	1.47[4,40] ± 0.01
Wustite	FeO		12.25	152.3[53] ± 0.2	4.9[53] ± 0.1	434[o,52,53] ± 50	1.48[54] ± 0.25

1 Graham and Barsch, 1969; 2 Issak et al., 1989; 3 Olinger, 1977; 4 Suzuki, 1975a; 5 Ashida et al., 1987; 6 Graham et al., 1988; 7 Williams et al., 1990; 8 Suzuki et al., 1981; 9 Watanabe, 1982; 10 Sawamoto et al., 1984; 11 Fei et al., 1992; 12 Gwanmesia et al., 1990; 13 Suzuki et al., 1980; 14 Hazen et al., 1990; 15 Weidner et al., 1984; 16 Sawamoto et al., 1986; 17 Rigden et al., 1991; 18 Suzuki, 1979; 19 Liebermann, 1975; 20 Bass et al., 1981; 21 Weidner et al., 1978; 22 Duffy and Anderson, 1989; 23 Watt and Ahrens, 1986; 24 Suzuki, 1975b; 25 Krupka et al., 1985; 26 Bass and Weidner, 1984; 27 Sueno et al., 1976; 28 Finger and Ohashi, 1976; 29 Levien et al., 1979; 30 Levien and Prewitt, 1981; 31 Cameron et al., 1973; 32 Kandelin and Weidner, 1988; 33 O'Neill et al., 1989; 34 Leger et al., 1990; 35 Suzuki and Anderson, 1983; 36 Robie et al., 1976; 37 Bass, 1989; 38 Skinner, 1956; 39 Weaver et al., 1976; 40 Krupka et al., 1979; 41 Bass and Kanzaki, 1990; 42 Yeganeh-Haeri et al., 1990; 43 Weidner and Ito, 1985; 44 Ashida et al., 1988; 45 Knittle and Jeanloz, 1987; Mao et al., 1991; see Hemley et al., 1992 46 Knittle et al., 1986; Mao et al., 1991; see Stixrude et al., 1992 47 Ito and Takahashi, 1989; 48 Mao et al., 1991; 49 Yeganeh-Haeri et al., 1989; 50 Weng et al., 1982; 51 Mao et al., 1989; 52 Jackson, 1982; 53 Jackson, 1990; 54 Touloukian et al., 1977.

a. Unless otherwise noted, volumes are from Jeanloz and Thompson, 1983; b. Assumed to be the same as the Mg end-member; c. Dependence on Mg/Fe ratio assumed the same as for spinel; d. Calculated from Eq. 13 and the properties of diopside; e. Assumed similar to pyrope; f. Calculated from Eq. 13 and the properties of pyrope; g. This work, see text; h. Assumed to be the same as pyrope; i. Bulk and shear moduli calculated from Eq. 12 and the properties of Mg-Majorite; j. Calculated from Eq. 13 and the properties of Mg-perovskite; k. Effect of Fe on shear modulus assumed the same as for enstatite; l. Calculated from Eq. 13 and the properties of Mg-perovskite; m. Calculated from Eq. 12 and the properties of Mg-perovskite; n. Shear modulus calculated from Eq. 12 and the properties of Mg-perovskite; o. Elastic value.

on a suite of garnets and the known volumes of pyrope, almandine and grossular [Ita and Stixrude, 1992].

Where available, K_o values are taken from ultrasonic or Brillouin scattering measurements. When experimental constraints were unavailable, we estimated the bulk and shear moduli by:

$$M_o V_o = M_{oR} V_{oR} \tag{20}$$

where M_o is the unknown modulus of a mineral, V_o is its molar volume and M_{oR} and V_{oR} are the corresponding known properties of a reference mineral [see also *Duffy and Anderson*, 1989]. Assumed values of K_o' were chosen to provide the best fit to compression data for the values of K_o used here. I prefer this approach, also advocated by *Bass et al.* [1981], to determinations of K_o' based on relatively low pressure ultrasonic measurements of K [e.g. *Gwanmesia et al.*, 1990], since it is based on direct measurement of an observable mantle property (ρ) at mantle pressure conditions.

For most minerals, values of θ_o and γ_o are constrained by heat capacity and thermal expansivity data as described by *Stixrude* and *Bukowinski* [1990]. When heat capacity data are not available, θ_o is estimated by:

$$\theta_o / \theta_o^e = \theta_{oR} / \theta_{oR}^e \tag{21}$$

where θ_o is the unknown thermal Debye temperature of a mineral, θ_o^e is its known elastic Debye temperature and θ_{oR} and θ_{oR}^e are the corresponding known properties of a reference mineral [see also *Watanabe*, 1982].

Due to the lack of a proper analog, the K_o and K_o' of majorites are treated as variable within the range of current estimates and adjusted to provide the best fit with seismic properties. Thus they also represent the greatest source of uncertainty in the upper mantle. The effect of this uncertainty in modeling mantle properties is discussed in chapter five.

Chapter 5

Comparison of Theory and Observation

5.1 Comparison

Isentropes of the three compositions are determined from the same fundamental thermodynamic relations used in the mineral elasticity calculations. This is accomplished by finding contours of constant entropy in pressure - temperature space. Isentropes should closely approximate geotherms since, for mantle conditions, the effects of viscous dissipation are only significant in thermal boundary layers [*Machetel* and *Yuen*, 1989]. The calculated geotherms are deflected by the heat of reaction during phase transitions [*Verhoogen*, 1965; *Jeanloz and Thompson*, 1983]. The exothermic nature of phase transitions below 21 GPa causes positive temperature jumps and high gradients in this region compared with the adiabatic compression of individual phases (Figure 5.1). The transformation of garnet and spinel into perovskite + magnesiowüstite is a strongly endothermic reaction and causes the substantial negative jump seen between pressures of 21 and 25 GPa. Higher pressures induce no further transitions and temperature changes slowly with pressure.

Based on the summary phase diagrams (Figures 3.1 and 3.2), I estimate relative mineral fractions in the upper mantle and upper part of the lower mantle along a representative adiabat (initial temperature at 180 km depth of 1700 K; *Jeanloz and Morris*, 1986). Abundances of individual garnet and perovskite species are shown in Figure 5.2 to illustrate their relative effects on their respective solid solutions. The larger Si # in composition B causes a larger pyroxene to garnet ratio at low pressures and a larger ratio of majorite to Al-rich garnet components at higher pressures. Below 900 km depth, the phase assemblage remains unchanged, but their relative proportions will change slightly due to differences in compressibility and thermal expansivity.

Figures 5.3 and 5.4 show the predicted density and bulk sound velocity profiles, respectively, of compositions A-C together with the expected profiles and the estimated standard deviations in the expected profiles. The predicted density of composition A agrees very well with the expected density
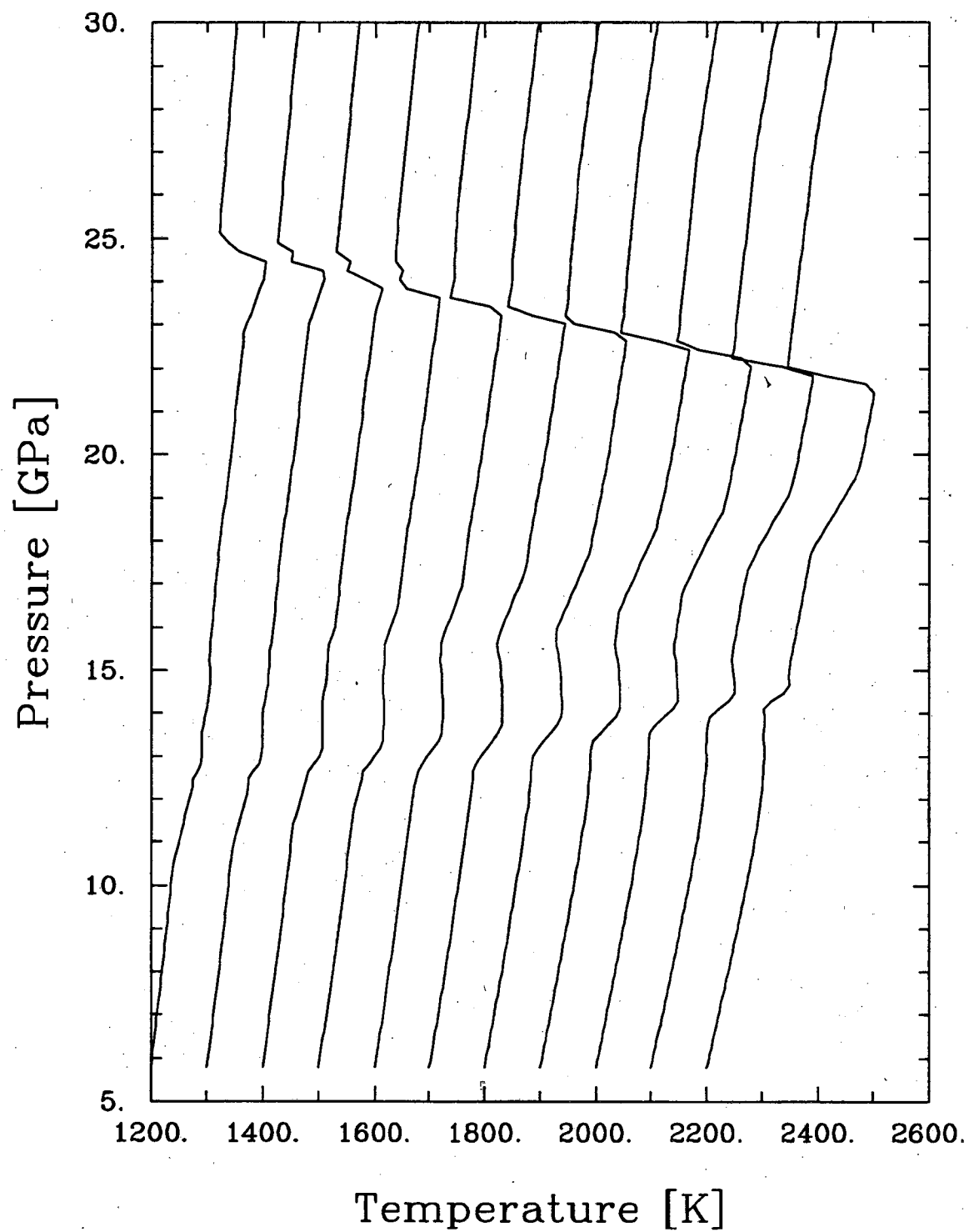
Fig. 5.1. Isentropes of composition A.

COMPOSITION A MINERAL PROPORTIONS
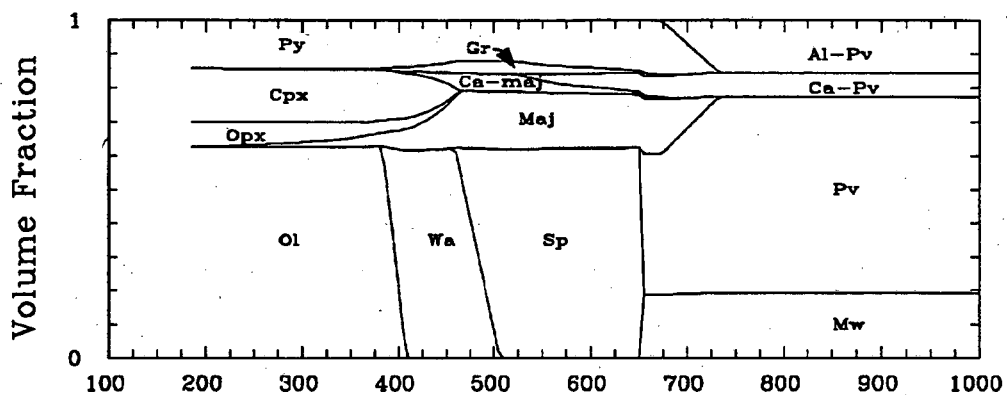
COMPOSTITON B MINERAL PROPORTIONS
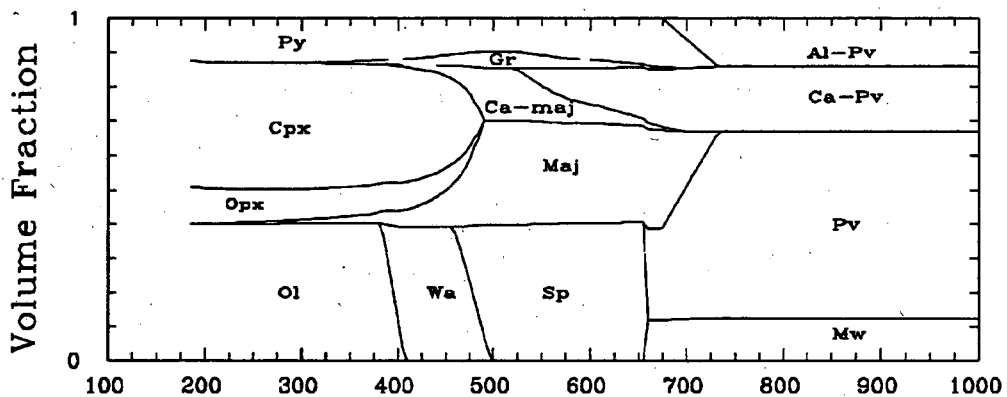
COMPOSITION C MINERAL PROPORTIONS
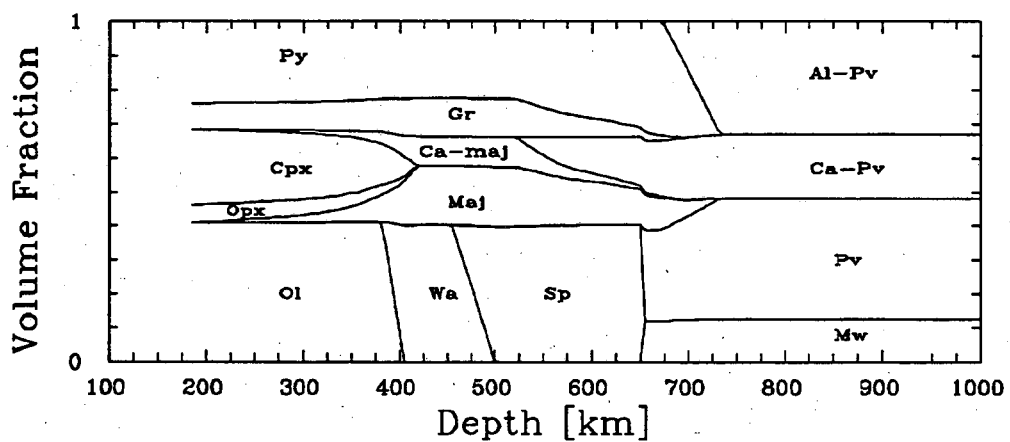
Fig. 5.2. Volume percentage of the minerals present in compositions A, B, and C as a function of depth.
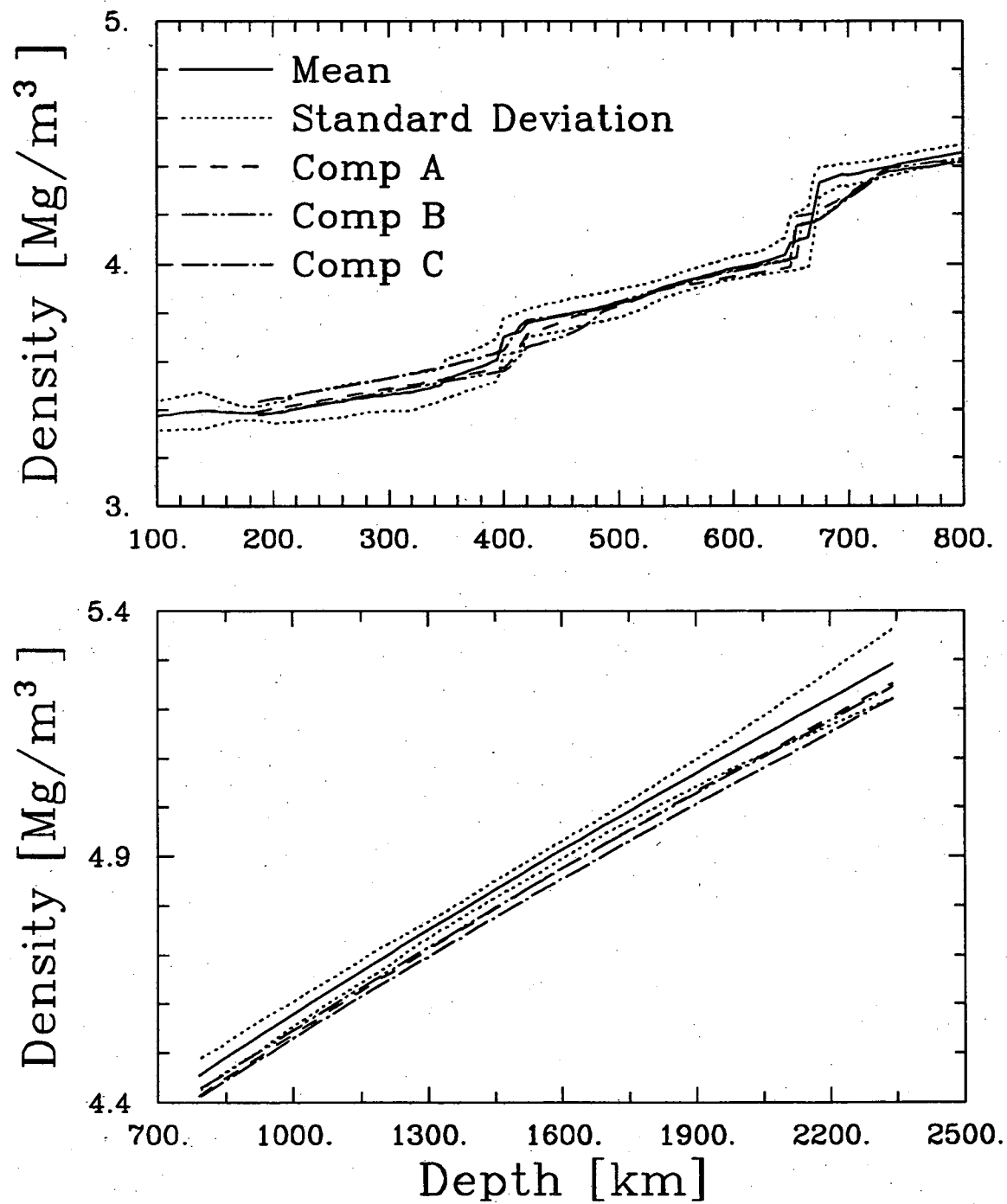
Fig. 5.3. Comparison of the expected density profile and its standard deviation with the predicted densities of compostitions A, B, and C.
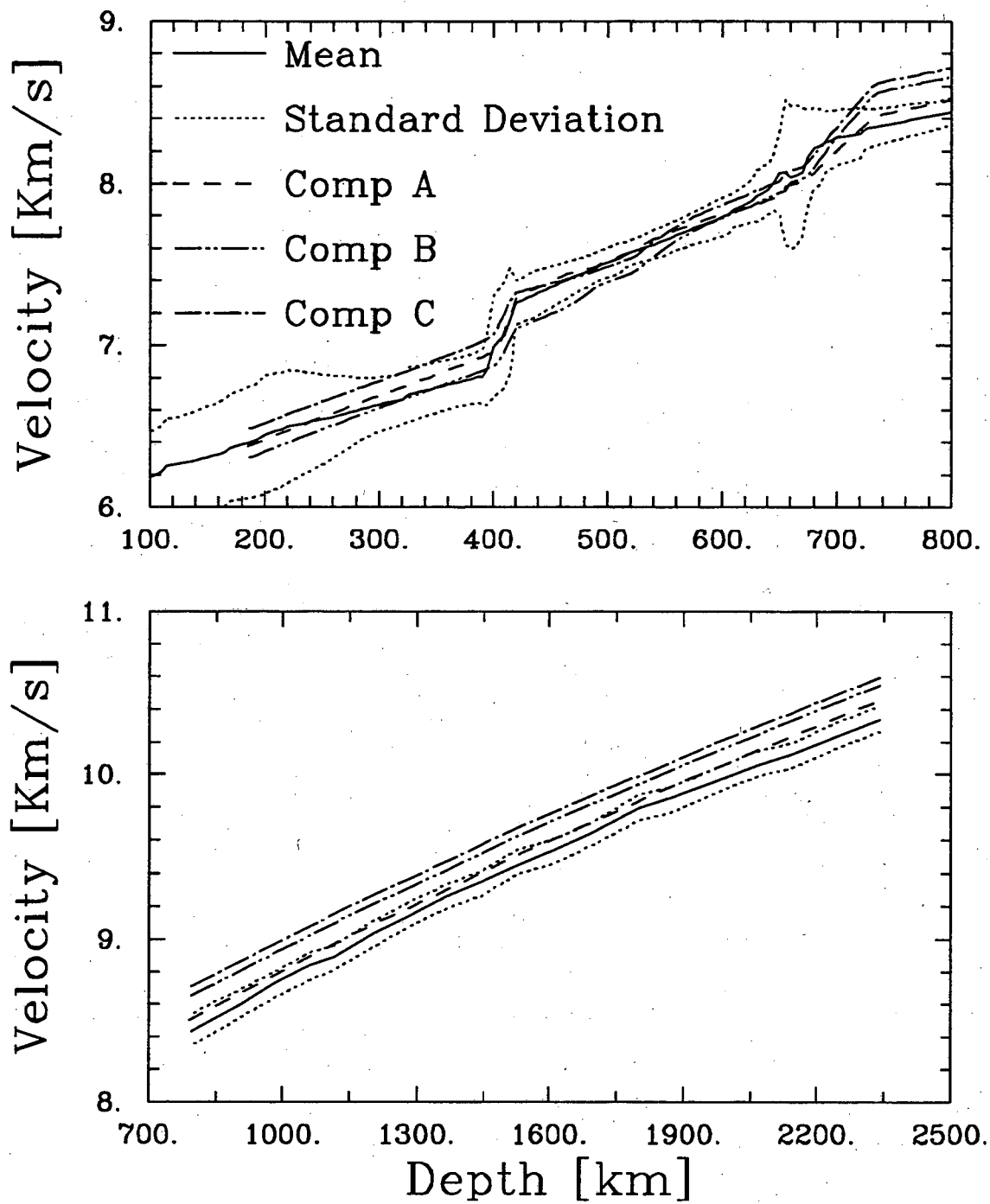
Fig. 5.4. Comparison of the expected V_Φ profile and its standard deviation with the predicted profiles for compositions A, B, and C.

profile throughout the upper mantle, but falls outside the estimated standard deviation of the expected profile through most of the lower mantle (Figure 5.3). Composition C also falls within the estimated standard deviation in the upper mantle but the agreement above 400 km is marginal. It also predicts densities that differ by more than one standard deviation from the expected profile for most of the lower mantle. Composition B matches the estimated ρ profile of the uppermost mantle, the lower part of the transition zone and the lower part of the lower mantle, but departs significantly from expected properties between 400 and 500 km and 900 to 2150 km depth given the estimates of the uncertainty.

In the uppermost mantle, the predicted bulk sound velocity (Figure 5.4) of all assemblages falls within one standard deviation of the expected velocity profile. Near the 400 km discontinuity, the character of B differs significantly from the other two. Composition B predicts a jump that is only two-thirds of the expected value. The velocity remains consistently low for the next 50 km and then rises to the expected value within a 30 km depth range. A rise in velocity occurs near the proposed 520 km seismic discontinuity [*Shearer*, 1990] in all assemblages due to the dissolution of Ca-perovskite. It is more pronounced in B and C due to their higher calcium contents. The rise is then followed by predicted values that agree with the mean velocity in the rest of the transition zone. In the lower mantle, the velocities predicted by A fall within one standard deviation of the expected profile except in the lowermost regions while B and C fall systematically above the range of uncertainty.

The predicted properties shown in the figures were calculated using the Birch-Murnaghan equation of state. As seen in Figure 5.5, using the universal equation of state has a negligible effect in the upper mantle. In the lower mantle the effects are noticable, but seemingly not large enough to alter the character of the fits. I will give a more quantitative evaluation on the impact of the form of equation of state used in the lower mantle in the discussion below.

5.2 Discussion - Upper Mantle

The results show that it is possible to account for the anomalously high velocity gradients in the transition zone with a uniform composition. In excellent agreement with *Birch's* [1952] explanation for the seismic properties of this region, I find that a series of phase transitions, including pyroxene to garnet, wadsleyite to spinel and the exsolution of Ca-perovskite, readily account for the expected density
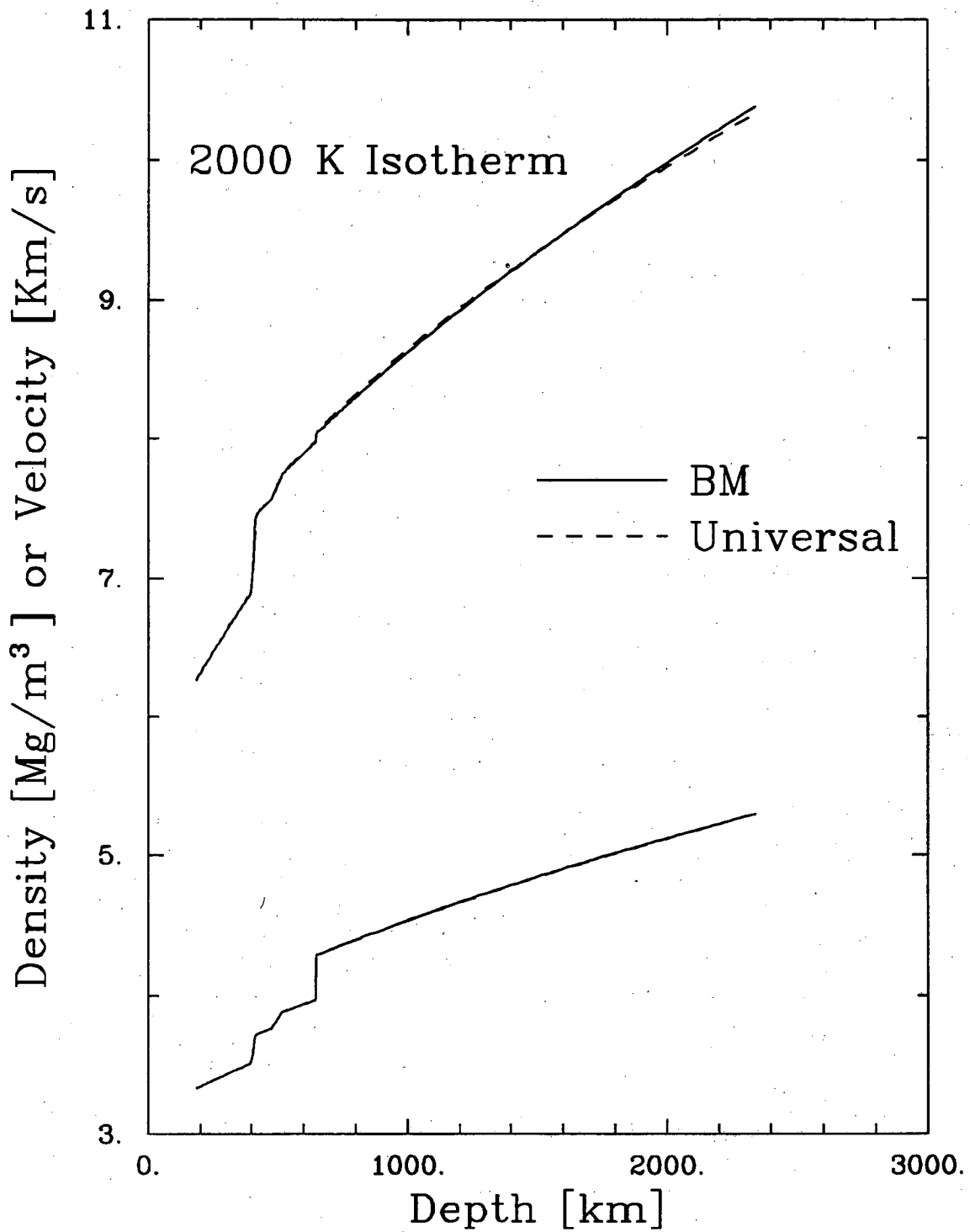
Fig. 5.5. Composite value of the density (ρ) and acoustic velocity (V_Φ) along the 2000 K adiabat for a pure olivine composition using the Birch-Murnaghan finite strain equation of state (solid line) and the Universal equation of state (dashed line).
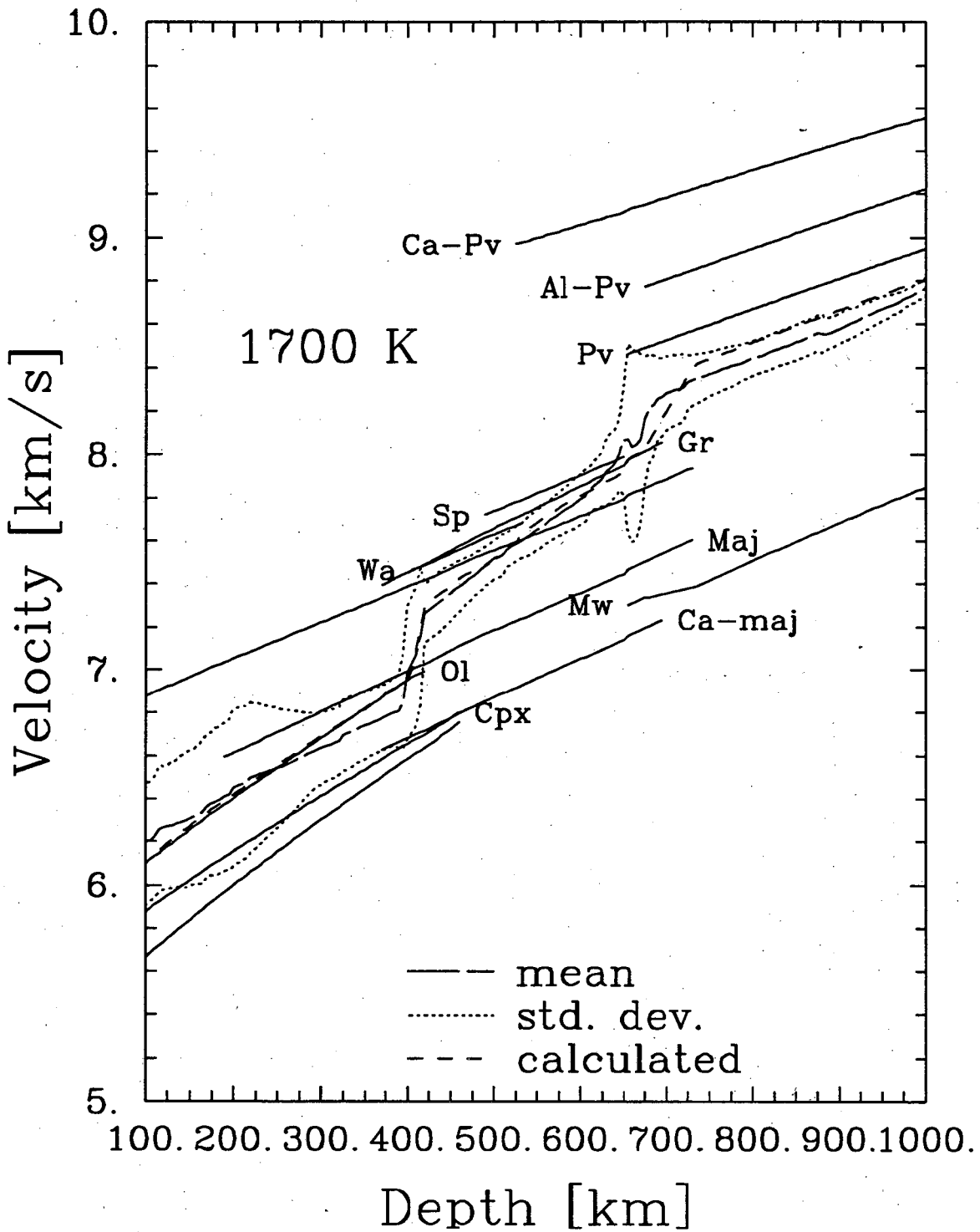
Fig. 5.6. Acoustic velocity of individual phases (solid lines) and the composite velocity of pyrolite (short dashed line). The mean and standard deviation of bulk sound velocity calculated from various seismic studies are represented by the long dashed and dotted lines, respectively.
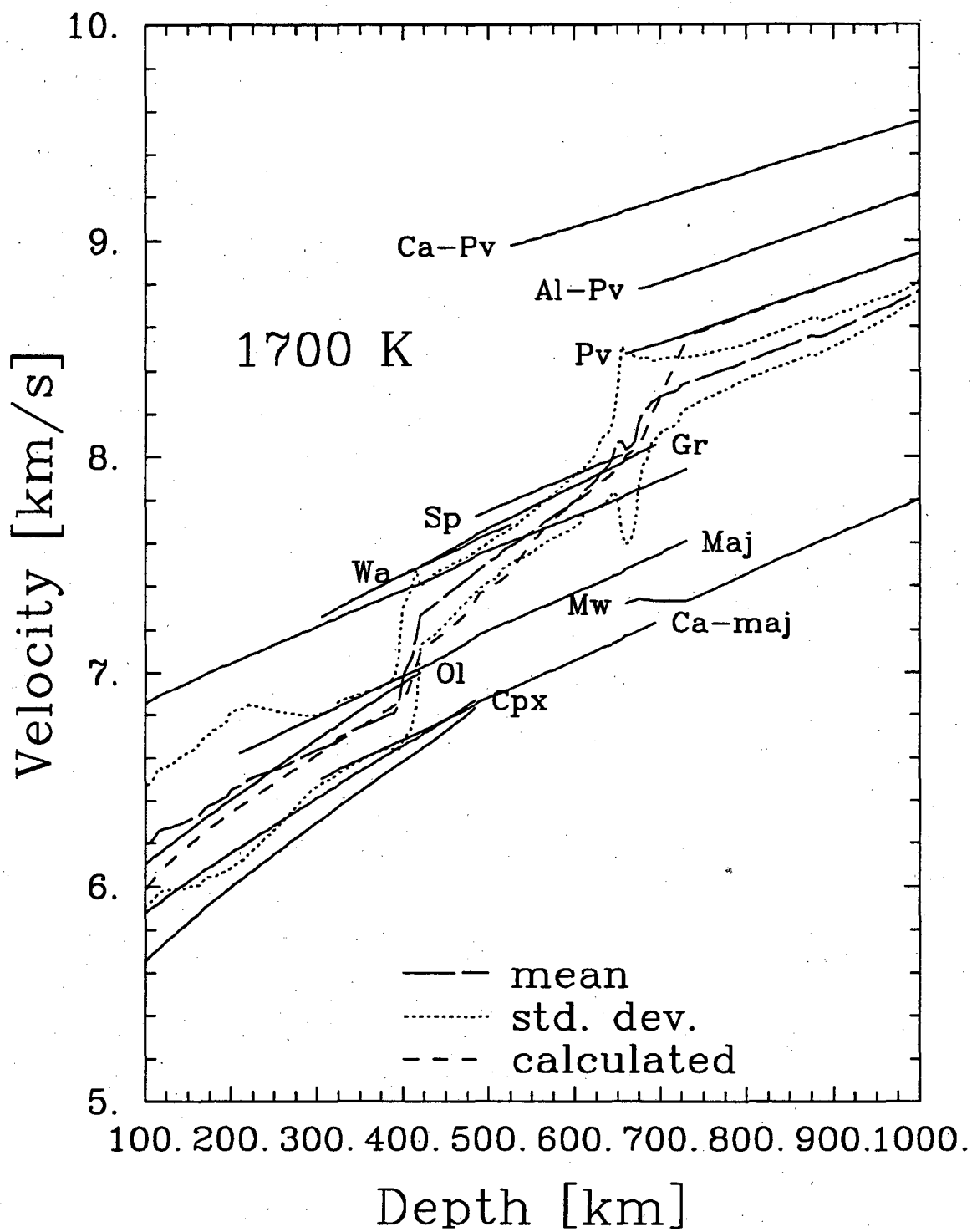
Fig. 5.7. Same as Figure 5.6 for composition B.
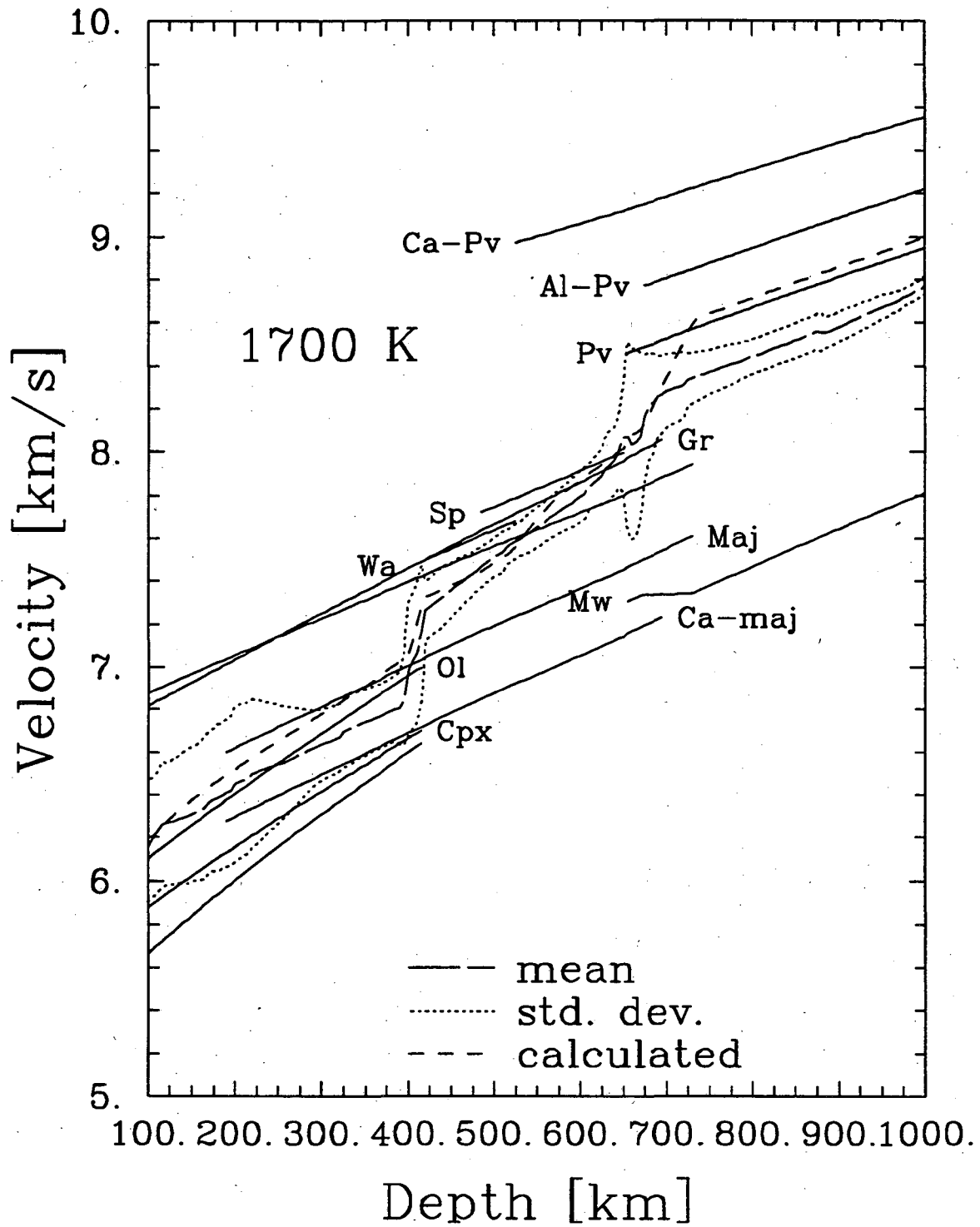
Fig. 5.8. Same as Figure 5.6 for composition C.

and velocity in this region (see Figures 5.6-5.8). A compositional gradient through the transition zone is not required in order to predict the expected properties in this region.

I find that pyrolite (composition A) provides an excellent account of the expected properties in the upper mantle and the transition zone. This is in agreement with the results of *Weidner* [1985] and *Weidner* and *Ito* [1987] who also concluded that seismic observations are consistent with a pyrolite composition to at least 670 km depth. Olivine-poor compositions, however, are also able to account for the expected profiles.

In all compositions, the transition of olivine to wadsleyite causes rapid increases in velocity over a 20 km interval near 400 km. This is consistent with the depth (390-420 km) and width (10-20 km) of the discontinuity in most seismic models [*Walck,* 1984; *Paulssen,* 1987]. The much sharper gradient found by *Leven* [1985] (less than 6 km wide) may not be representative of the normal mantle because the earthquakes used in this study were located in or near a subduction zone. High thermal gradients present in these areas may tend to sharpen the discontinuity by narrowing the dissolution width of relevant phase changes or give the appearance of a sharp discontinuity by focusing seismic energy at higher frequencies. Composition A predicts a 4.5 % velocity jump at the discontinuity, in excellent agreement with recent P and S wave velocity profiles, which predict a jump in bulk sound velocity of 4.5 to 6 % (Figure 2.4) [*Walck,* 1984; *Grand and Helmberger,* 1984a; *Leven,* 1985; *Paulssen,* 1987; *Lefevre and Helmberger,* 1989; *Kennett and Engdahl,* 1991]. In composition C, the effect of this transition is muted because of its lesser olivine content. However, its greater Al content, relative to compositions A and B, lead to a shallower pyroxene to garnet transition. The combined effect of the olivine to wadsleyite and pyroxene to garnet transitions in composition C leads to good agreement with the expected magnitude of the discontinuity. The smaller amount of Al in B delays the pyroxene to garnet transition to higher pressures (Figure 5.8) causing a much smaller velocity jump (3.3 %) than expected. Nevertheless, this is marginally consistent with observed conversions at the discontinuity [*Bock and Kind,* 1991]. However, due to the delayed transition, the predictions of composition B continues to deviate significantly from the expected velocities and densities 80 km below below the discontinuity.

Velocity and density profiles predicted by the compositions also display a small rise near 520 km

depth. The rise is caused by the dissolution of Ca - perovskite from Ca rich garnets and majorites (Figure 5.2). The depth and character coincides well with new evidence for a discontinuity near that depth from investigations of long period body waves [*Shearer*, 1990; *Revenaugh and Jordan*, 1991]. Shorter period studies find little or no evidence for the discontinuity suggesting that it very diffuse (> 50 km thick) [*Cumminsetal.*, 1992; *Jones et al.*, 1992] in agreement with the behavior predicted here. The small amplitude of the rise (1 to 3%) is also consistent with the amplitude of the seismic reflections [*Cumminsetal.*, 1992].

To account for the uncertainties of the thermodynamic parameters in the upper mantle and transition zone, alternative estimates of K_o for the majorite species and K_o' for the majorites, wadsleyite, and spinel are considered (Table 4.1). Variation of other parameters within their uncertainties has a comparatively small effect on derived mantle velocities. For pyrolite, values of K_0 of majorites and K_o' of majorites, wadsleyite and spinel at the lower extreme of current estimates were used to generate Figures 5.3 and 5.4. Higher majorite bulk moduli lead to higher bulk sound velocities in the transition zone, causing pyrolite to deviate significantly from the observed profile (Figure 5.9). Although raising mantle temperatures can reconcile calculated velocities with observation, higher temperatures lead to disagreement with observed densities. Adopting high values of K_o' for wadsleyite does not affect the acceptability of pyrolite, although high values of K_o' for spinel cause significant disagreement just above the 670 km discontinuity. Pyrolite provides an acceptable fit to upper mantle and transition zone properties for values of majorite bulk moduli and spinel K_o' in the lower half of the range considered here. Similar behavior is seen in the calculations for composition C.

Average values of majorite bulk moduli and values of K_o' of majorite, wadsleyite and spinel at the lower extreme of current estimates were used to generate the values predicted by composition B. Lower and higher majorite bulk moduli lower and raise transition zone velocities, respectively, and magnify the disparity between the predicted and expected bulk sound velocity profiles (Figure 5.9). Again, agreement with velocities can be improved by raising or lowering assumed mantle temperatures but only at the expense of the density comparison. Alternative values of K_o' of wadsleyite and spinel improve agreement with the bulk sound velocity profile but magnify the discrepancy in density between
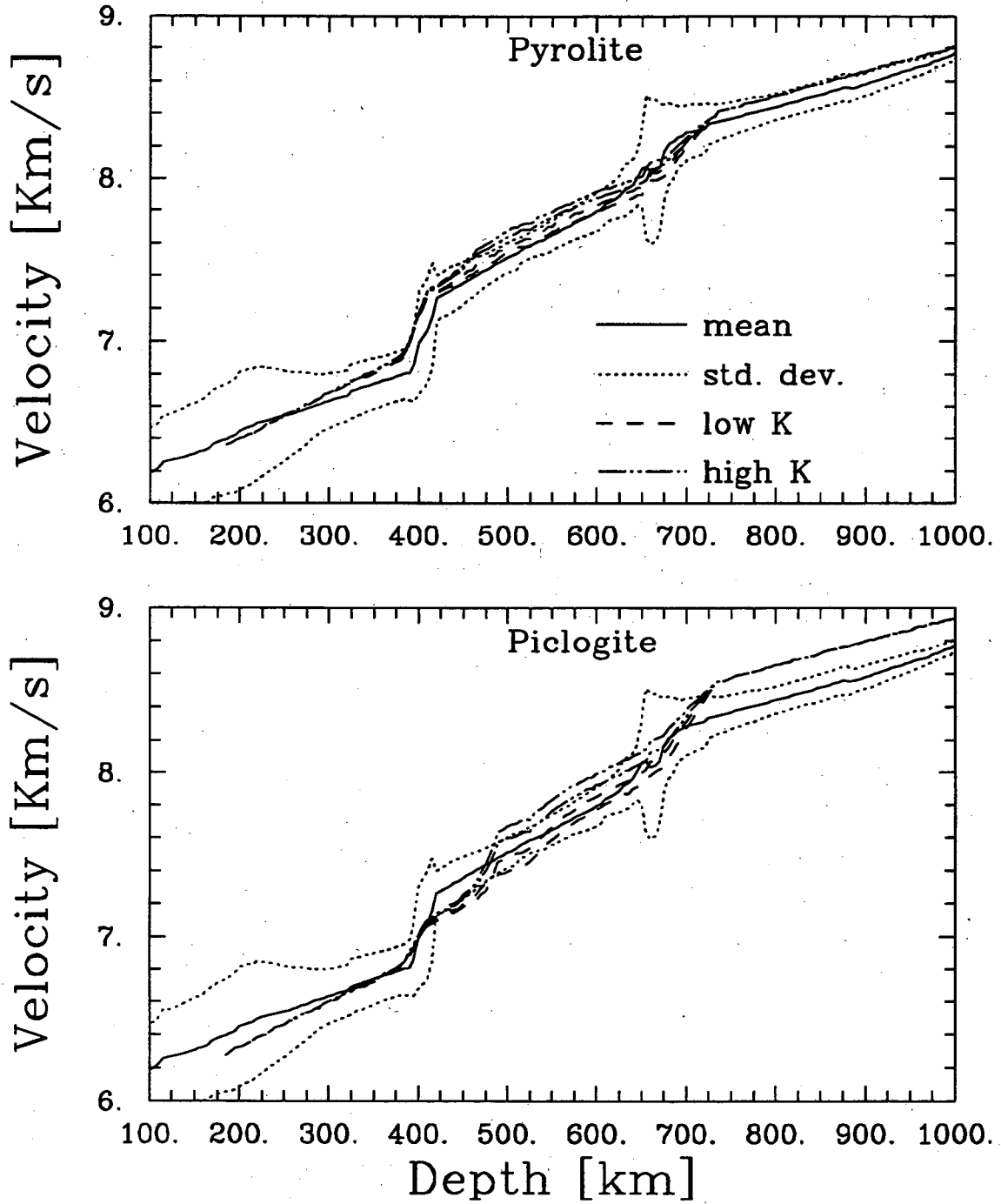
Fig. 5.9. Effect of the uncertainty in the majorite elastic parameters on the composite profile. High and low values of K produce the higher and lower pairs of dashed curves, respectively. High and low values of K' produce the higher and lower curves for each pair. The mean and standard deviation of observed velocities are represented by the solid and dotted lines, respectively.
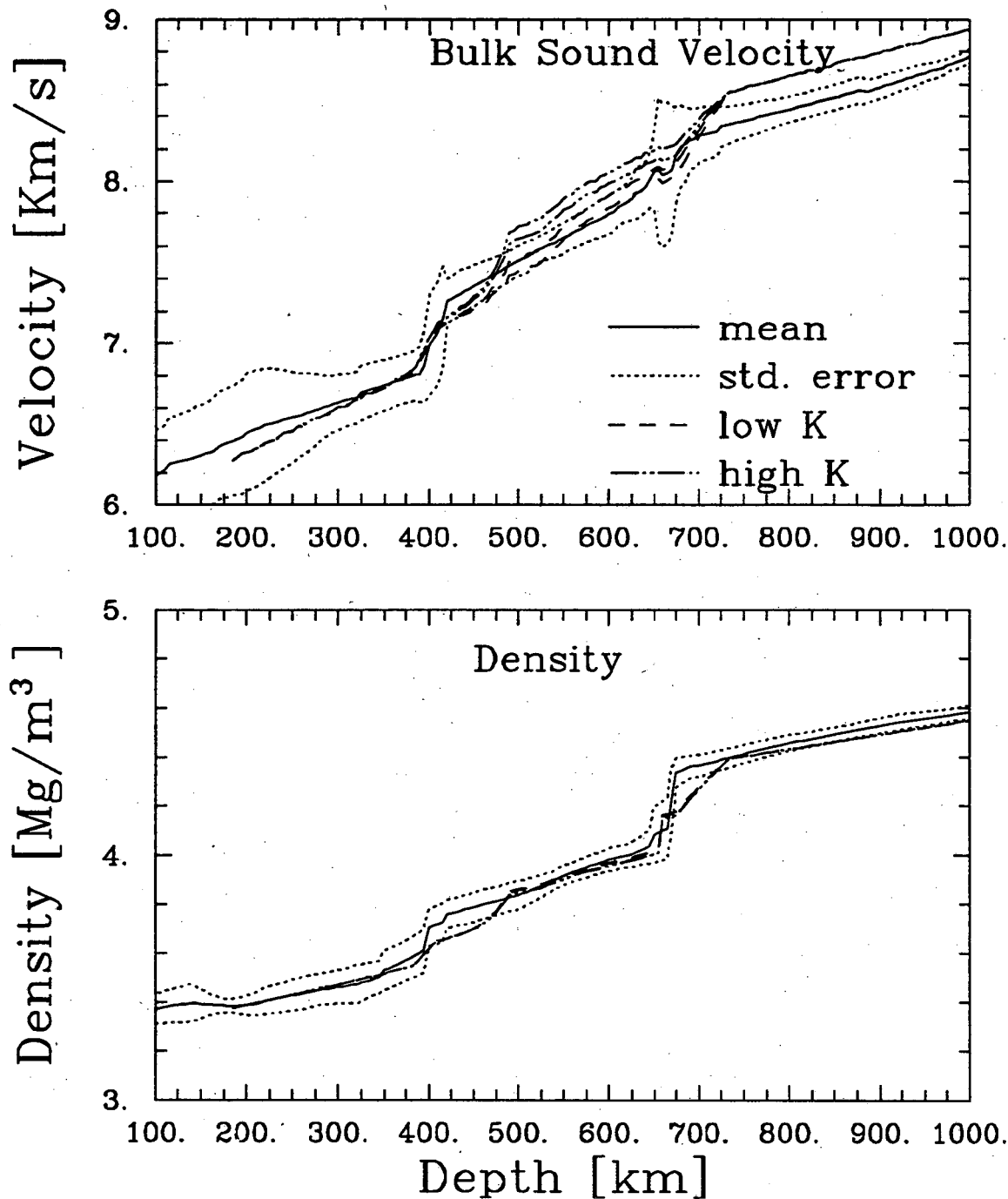
Fig. 5.10. Effect of the uncertainty in the majorite elastic parameters coupled with a K' value of 4.8 and 5.0 for wadsleyite and spinel, respectively, on the bulk sound velocity and density of composition B. High and low values of majorite bulk moduli produce the higher and lower pairs of dashed curves, respectively. High and low values of K' produce the higher and lower curves for each pair. The mean and standard deviation of observed velocities and densities are represented by the solid and dotted lines, respectively.

400 and 500 km (Figure 5.10). Regardless of variations in the thermodynamic parameters or temperature, composition B does not provide an acceptable fit to both bulk sound velocity and density profiles.

5.3 Discussion - Lower Mantle

In agreement with many previous studies, the $MgO-FeO-SiO_2$ fraction of the compositions considered here is marginally consistent with observed lower mantle properties [e.g. *Jackson* 1983; *Bukowinski and Wolf*, 1990]. However, consideration of the CaO component degrades the comparison. Through Ca-perovskite, likely the fastest mantle mineral (highest bulk sound velocity, Figures 5.6-5.8), the CaO component causes complete pyrolite, piclogite and Al-rich piclogite to overestimate bulk sound velocities at the top of the lower mantle by 1 %, 2 %, and 3 %, respectively, the larger differences for the latter two reflecting their greater CaO content. Lower mantle densities are also underestimated by all three models.

The effects of the uncertainties in the lower mantle parameters on calculated properties tend to be larger, but are well characterized. The recent abundance of data in the $Mg0-FeO-SiO_2$ system relevant to the desired thermodynamic properties allow a quantitative error analysis. Experimental measurements of thermal expansion and heat capacity constrain θ and γ, compression data determine the errors associated with the values of K and K', and phase equilibria measurements provide constraints on the interaction parameters and the reference free energies. The best fitting values and their associated errors are found by minimizing the value of χ^2 between the experimental and calculated values [see Table 4.1, *Stixrude and Bukowinski*, 1992 and *Stixrude and Bukowinski*, 1990 for details and results]. Elasticity data is also available for the Ca- and Al-bearing perovskites. However, their thermal properties have been estimated and thus assigned generous uncertainties (Table 4.1).

I use the variance and covariance of the thermodynamic parameters determined in this way as generating functions in a Monte Carlo algorithm to simulate the probability distribution of the density and bulk modulus of mineral assemblages at elevated pressures and temperatures. The simulation results show that the distributions of ρ and K are, to a good approximation gaussian. Thus the non-linearities inherent in the thermodynamic and mechanical mixing of end-member species do not cause errors in the predicted lower mantle ρ and V_ϕ estimates to significantly deviate from a normal distribution.

Considering these errors in the comparison, I find that the bounds on the expected profiles and the profiles predicted by composition C overlap (figure 5.11). Over the depth range of the lower mantle, the average relative error of the expected ρ and V_Φ is approximately 0.7% and 0.8%, respectively. The predicted ρ and V_Φ have an average relative error of 0.6% and 1.8%, respectively. The errors are clearly of the same order and both should be taken into account when making these comparisons.

A formal measure of the significance of the difference between the predicted and expected profiles is given by the χ^2 statistic:

$$\chi^2 = (\vec{p} - \vec{e}) \cdot (\Lambda_p + \Lambda_e)^{-1} \cdot (\vec{p} - \vec{e}) \tag{15}$$

where $\vec{p}$ and $\vec{e}$ are vectors of length N whose elements are the predicted and expected values, respectively, of ρ or V_Φ at N depth points and Λ_p and Λ_e are their associated covariance matrices. Predicted and expected profiles are compared at sixteen depth points located 100 km apart for V_Φ and five depth points located 300 km apart for ρ. The spacing was chosen based on the expected resolution of ρ and V_Φ in the lower mantle appropriate for the estimated uncertainties in the expected profiles [*Tralli and Johnson*, 1986; *Gilbert et al.*, 1973].

For the purpose of illustration, I note that χ^2 is less than the number of degrees of freedom (N) for all compositions (Table 5.1), as suggested by the overlap of error bounds shown in Figure 5.11. This means that with at least 68% confidence the following hypothesis (H1) can be rejected: the predicted and expected profiles are drawn as random samples from different parent probability distributions. This test would be relevant, for example, in the case of comparing a single experimental measurement of density at a given pressure and temperature with a seismological determination of density at the corresponding depth. However, the expected and predicted profiles are based on many measurements so that I have some confidence in their mean values and the shapes of their probability distributions. In this case, it is appropriate to test the following hypothesis (H2): the means of the predicted and expected probability distributions are determined by repeated sampling of different parent probability distributions. Clearly this is a more restrictive test since the range of values within which the mean of a finite sample of the parent distribution is expected to fall for a given level of confidence is smaller than the expected range for any single event in that sample at the same confidence level.
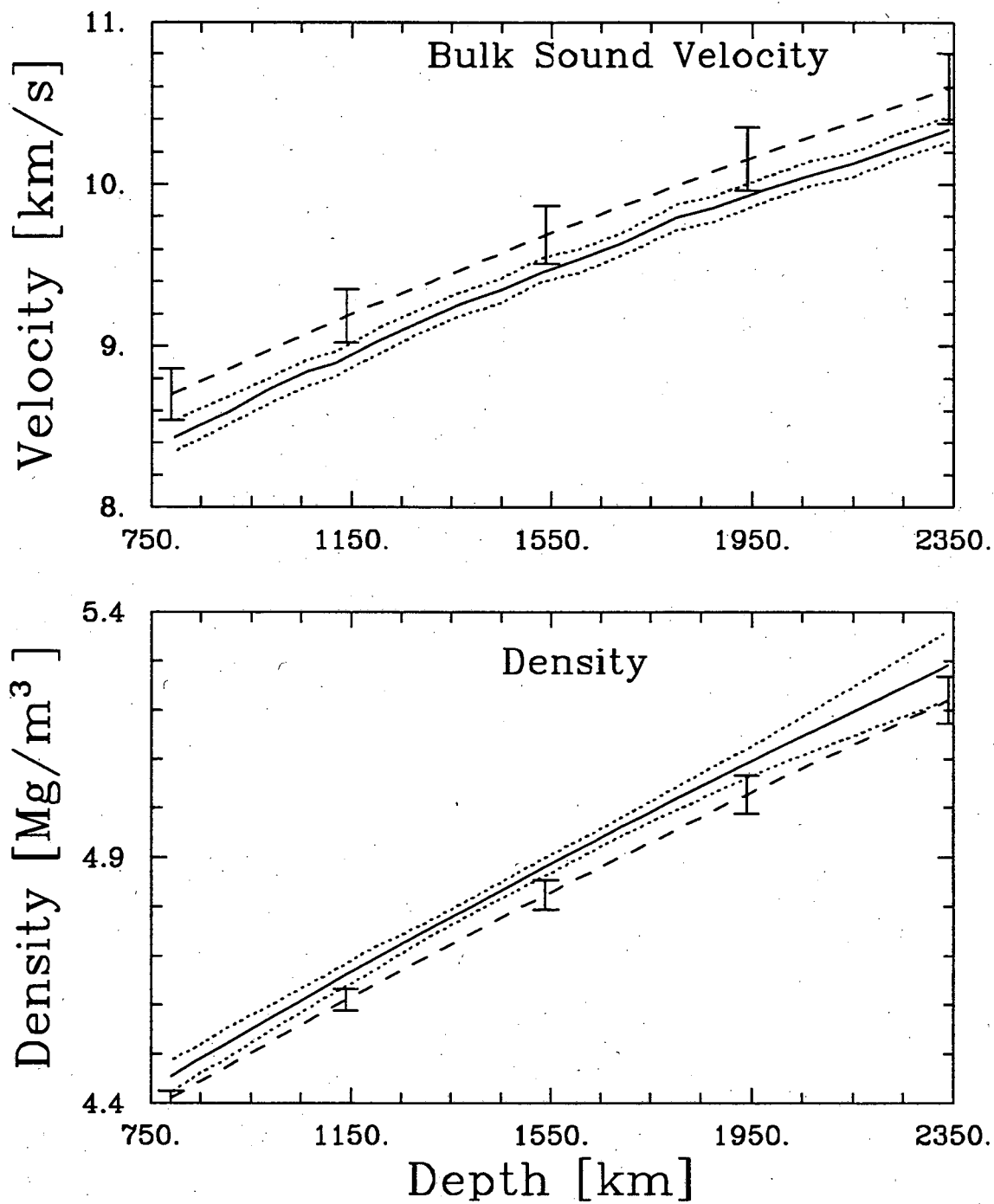
Fig. 5.11. Comparison of the the expected mean (solid line) and standard deviation (dotted line) with the predicted properties of composition C (dashed line) and their associated uncertainties (error bars).

Composition	Eq. of State	Best Fit	χ^2_{BF}	χ^2_{UM}	68% Low	Conf High	95% Low	Conf High
A	BM	1575	1.36	3.55	1410	1750	1260	1880
	UN	1585	1.73	3.69	1425	1765	1265	1895
no covariance	BM	1780	7.60	9.90	1690	1875	1580	1975
no predict. error	BM	1675	15.68	16.04	1570	1780	1465	1885
B	BM	1690	4.05	4.65	1530	1870	1375	2050
	UN	1725	4.51	5.05	1565	1895	1340	2160
C	BM	1570	5.36	7.28	1385	1765	1215	1970
	UN	1605	6.26	7.64	1430	1800	1250	2000

TABLE 5.1. Temperatures at the foot of the spectrum of lower mantle adiabats (K) determined from the error analysis. BM refers to the Birch-Muraghan equation of state. UN refers to the universal equaiton of state. χ^2_{BF} is the χ^2 value of the best fitting adiabat and χ^2_{UM} is the value for the adiabat projected from the upper mantle.

The modelling procedure of *Press et al.*, [1986, pp. 534-5] is adopted to determine the temperature at the foot of the lower mantle adiabat (670 km depth) which minimizes χ^2 for each composition and the uncertainty in this best-fitting temperature. This is equivalent to determining the range of adiabats which do not satisfy H2 in the case that the best fitting temperature yields a perfect fit between predicted and expected profiles (minimum value of χ^2=0). The results of this procedure are shown in Table 5.1.

The adiabat which produced the best fits to expected properties of the upper mantle and transition zone (1700 K at 185 km depth, e.g. Figure 5.1) implies a temperature of 1822 to 1841 K at the top of the lower mantle. Table 5.1 shows that temperatures which produce the best fits to lower mantle observations using the Birch-Murnaghan equation of state are 250 to 260 K colder. The best fitting temperature is bounded by profiles which raise the χ^2 level by 1 at the 68% confidence level and by 4 at the 95% confidence level. Thus we see that the difference between the best fitting and upper mantle profiles is not significant at the 95% confidence level, but is significant at greater than the 68% confidence level in the case of compositions A and C, the two which produced acceptable fits to the upper mantle and transition zone. Employing the universal equation of state produces temperatures which are 20 to 35 degrees higher, but this affect does not alter the conclusions of the prior analysis. Minimum misfits for compositions B and C also lie outside the 68% confidence level of composition A indicating the these compositions cannot adequately reproduce the properties of the lower mantle at any temperature.

None of the compositional models considered here match expected profiles over the entire depth range of the mantle at the 68% confidence level. The extent to which this result is affected by possible, as yet undiscovered, phase transitions in the perovskite species and magnesiowüstite or the possible significance of higher order thermodynamic parameters (e.g. volume dependence of q) at very high pressures and temperatures will require further experimental and theoretical investigation. Seismological observations, in particular the expected density profile, are also not free of systematic uncertainty. If the 14 density profiles I have considered here are not significantly biased by attenuation and I assume that their mean best represents the expected density profile, rather than PREM, best fitting temperatures for compositions A-C are raised by approximately 100 K, making them consistent with the best fitting

upper mantle adiabat.

The effect of neglecting covariance and uncertainties in the predicted profiles is also shown in Table 5.1. If the off-diagonal terms in Λ are ignored, H2 and the less restrictive hypothesis, H1, are satisfied at the 95% confidence level for both compositions B and C regardless of temperature. The best fitting temperature for composition A is higher if covariance is ignored, but its upper bound is still well below what one would expect from the best fitting upper mantle adiabat. Ignoring uncertainties in the predicted profiles also causes B and C to satisfy H2 and H1 at the 95% confidence level. The best fitting temperature for A is higher in this case because higher temperatures lead to better agreement with the expected V_ϕ profile at the expense of the ρ profile. The V_ϕ profile is weighted more strongly if predicted errors are ignored since its error is reduced by a greater percentage than that of density.

5.4 Geophysical Implications

In the upper mantle, pyrolite offers an excellent explanation of the expected properties but not a unique one. Olivine poor compositions can be reconciled with seismic observations if they are substantially enriched in Al at the expense of Si. This lowers the pressure of the pyroxene to garnet dissolution, raising velocities immediately below the 400 km discontinuity. Recently discovered kimberlite xenoliths, thought to have originated near 400 km depth, also suggest Al rich compositions [*Sautter et al.,* 1991], although these may not be representative of the bulk transition zone. Sodium enrichment also lowers the pyroxene to garnet transition and may also improve agreement with a piclogite-type composition [*Gasparik,* 1990]. Furthermore, Ca-perovskite may provide an explanation of the proposed 520 km seismic discontinuity [*Shearer,* 1990]. The transformation of garnet to Ca-perovskite near 18 GPa produces anomalous velocity gradients in all the compositions considered here which may account for the observed reflections (Figures 5.6-5.8).

For the range of compositions considered here, a chemically layered upper mantle is unlikely. Adiabats initiating at 1700-1800 ° K at 185 km lead to the best agreement with observed transition zone properties regardless of composition. These temperatures agree very well with independent determinations from geothermometry [see *Jeanloz and Knittle,* 1989]. A chemical boundary at 400 km, however, requires layered convection and a thermal boundary at this depth of 500-1000 ° K [*Jeanloz and*

Richter, 1979]. Retaining a 1700 ° K adiabat in the uppermost mantle, one finds that transition zone properties along a 2200 ° K adiabat are in severe disagreement with observed densities (Figure 5.12). Furthermore, these high temperatures may cause wide spread partial melting of the transition zone (Figure 3.2) leading to shear velocities much lower than observed. Alternatively, if one assumes a 1700 ° K adiabat in the transition zone, the uppermost mantle follows a 1200 ° K adiabat which is marginally consistent with seismic data for some compositions (Figure 5.12) but inconsistent with geothermometry.

Best estimates of predicted and expected profiles and their uncertainties indicate that the composition of the lower mantle may differ from that of the upper mantle if one accepts a PREM density distribution in the lower mantle. This conclusion is considerably strengthened if a thermal boundary layer exists at 670 km. Recent studies of mantle convection indicate that the thermal energy of perovskite forming reactions may be sufficient, even in an isochemical mantle, to induce two-layer convection [*Machetel* and *Weber*, 1991]. This would raise lower mantle temperatures by 500-1000 K, [*Jeanloz* and *Richter*, 1979], increasing the discrepancy between compositions A-C and seismic observations. If a compositional difference does exist, the lower mantle is most likely enriched in SiO_2 or FeO components, which would lead to inherently denser and faster assemblages which would match lower mantle observations along the relatively hot mantle adiabats required by a thermal boundary layer [*Jeanloz and Knittle*, 1989; *Bina and Silver*, 1990; *Stixrude et al.*, 1992].
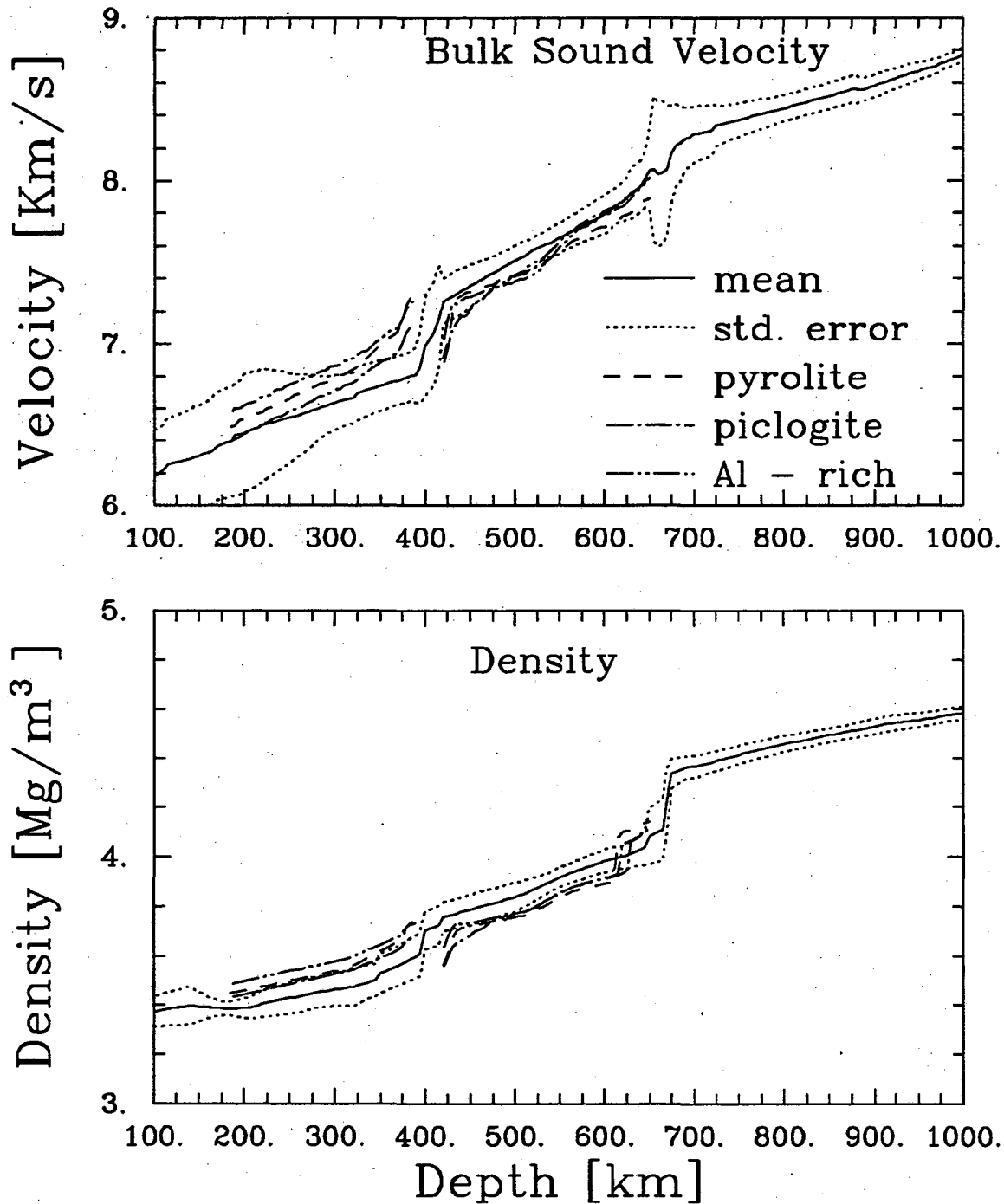
Fig. 5.12. Effect of a thermal boundary layer on calculated mantle properties. For the three compositions considered here, upper mantle properties are shown along the 1200 K adiabat. Transition zone properties are shown along the 2200 K adiabat. The mean and standard deviation of acoustic velocity and density are represented by the solid and dotted lines (see text for discussion).

Chapter 6

Subduction Zones

6.1 Introduction

As demonstrated in the preceding chapter, phase equilibria studies of minerals thought to exist in the mantle are significant in that they can help determine bulk compositions of mantle rocks by comparing the elastic properties of the observed assemblages to those observed in the mantle. These studies may also be useful in determining the fate of the subducting oceanic lithosphere (slabs). Given a certain chemical model of a slab, its mineralogy and density can be determined. Isobaric phase changes may affect seismic velocity estimates within subducting slabs used to determine depths of penetration into the lower mantle [*Anderson*, 1987]. Given slab density, one can calculate the buoyancy of the slab relative to the rest of the mantle. Phase changes can give rise to density changes which may significantly affect on the slab's ability to sink into the lower mantle (Christensen and Yuen, 1984). In this chapter, I calculate the effect of phase changes on velocity and density and discuss their impact on interpretation of seismological data and implications for mantle dynamics.

6.2 Slab Mineralogy

In order to apply the phase diagrams developed in chapter 3, a temperature versus depth model of the earth was calculated with the method utilized by *Creager and Jordan* [1984, 1986]. They employ a simple kinematic, thermal diffusion model to quantify perturbations to a potential temperature profile caused by the injection of cold oceanic lithosphere. An error function with an asymptote of 1573 K is used to represent the presubduction potential temperature profile. The thermal diffusivity used to compute the post subduction potential temperature profile is $1 \times 10^{-6} \mathrm{m}^2/\mathrm{s}$ which is within the known uncertainties for the minerals expected to be present in the slab [*Jeanloz and Thompson*, 1983]. The final thermal model was computed by converting potential temperature to real temperature via the geotherm predicted by composition A (pyrolite) and is shown in Figure 6.1. As discussed previously, of the three
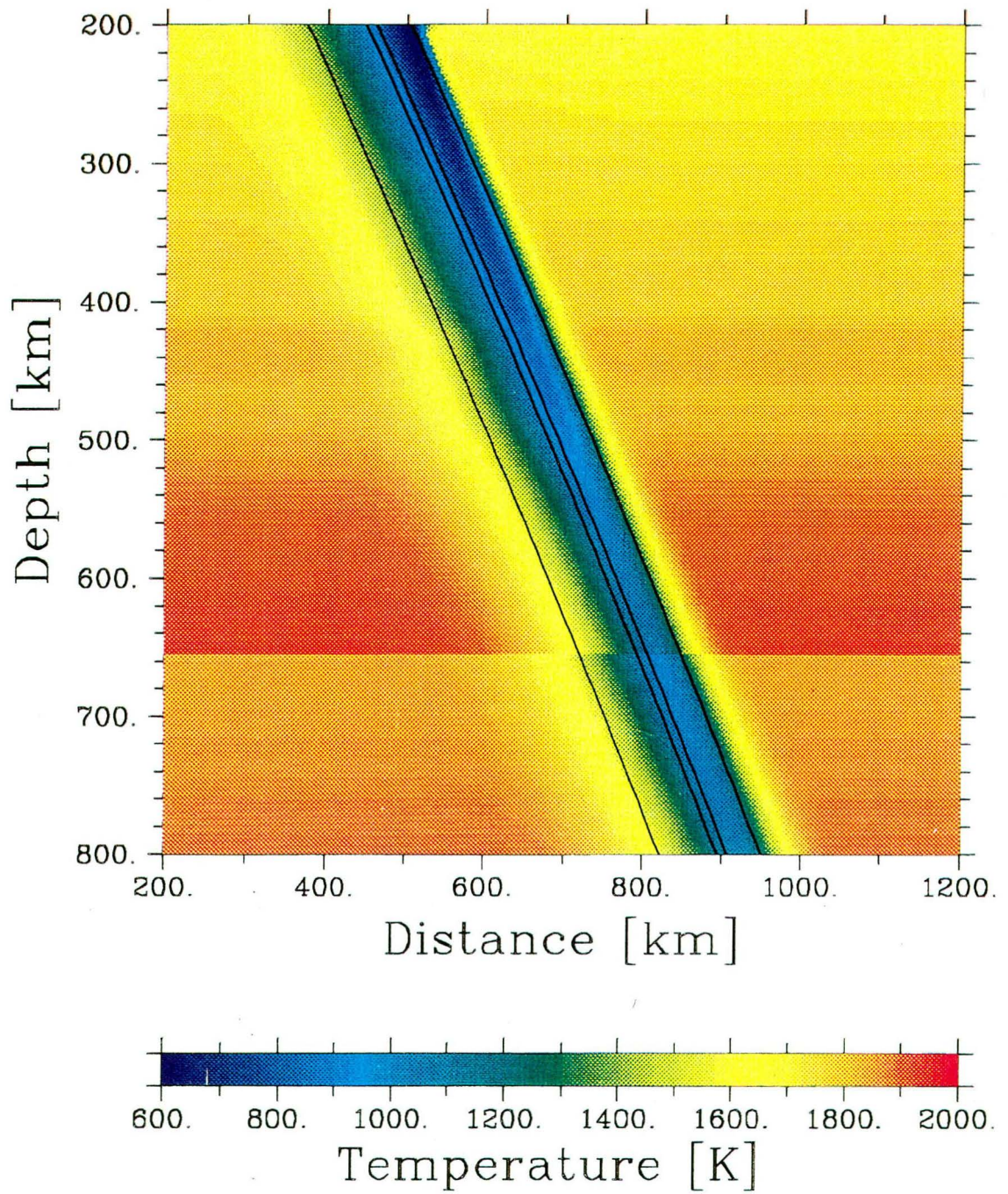
Fig. 6.1. Thermal model of the downgoing slab. Lines represent, from left to right, the bottom of the pyrolite layer, the bottom and top of the lherozilte layer, and the top of the harzburgite layer.

models, pyrolite provides the best fit to the predicted mantle properties and should thus best represent the effects of thermal perturbations in the mantle. Given the above temperature field, the mineralogy of the olivine component of the slab takes on the form shown in figure 6.2. The residuum component is shown in figure 6.3. The temperature gain or loss in the material due to isobaric phase changes is omitted in this analysis. In the upper mantle, temperature induced perturbations in the deflection of an adiabat by heats of reaction is fairly minor, although the changes in pressure at which the deflections occur can be noticeable (Figure 6.1). However, for my purposes, these affects can be safely ignored.

To assure the spatial smoothness of the phase fields in Figure 6.3, a chemical transition from harzburgite to pyrolite must occur in the lherzolite layer (Figure 3.1). The transition is outlined in the phase diagrams shown in Figure 6.4a-f. The diagrams are formed by linearly interpolating the phase boundaries shown in Figures 3.3 and 3.4 as a function of position between the upper and lower lherzolite boundaries. In Figure 6.4b, the phase field of wadsleyite + stishovite + garnet is inhibited due to the increasing Mg and Ca content, while the and upper and lower boundaries of the spinel + stishovite + garnet field remain constant [*Akaogi et al*, 1987]. The rest of the phase boundaries are assumed to vary linearly with composition which is reasonable given the uncertainties in the phase equilibria. The wadsleyite + stishovite + garnet field is assumed to disappear when harzburgite contains 15 % pyrolitic material. Beyond this point the spinel + stishovite + garnet field also becomes inhibited due to the increasing Ca and Mg content [*Akaogi et al*, 1987] as shown in Figure 6.4c and vanishes when approximately 60 % of the residuum component is derived from pyrolite. From that point on, only the phase fields representative of a pyrolitic composition are present. It is also at this point that the Ca-Perovskite is assumed to appear.

As one can see in Figure 6.2 possible variations in the from of the phase diagram for the olivine subsystem has a noticeable effect on the slab phase assemblage. These differences are of great importance to the material properties of the slab due to the increased amount of olivine component in the harzburgite layer. Volumetrically, the olivine component comprises 82% of the assemblage (Figure 6.5). Kinetic hinderence of the olivine to wadsleyite transition allows metastable olivine to persist down to 550 km (Figure 6.5b) completely removing the the wadsleyite field that would otherwise be present
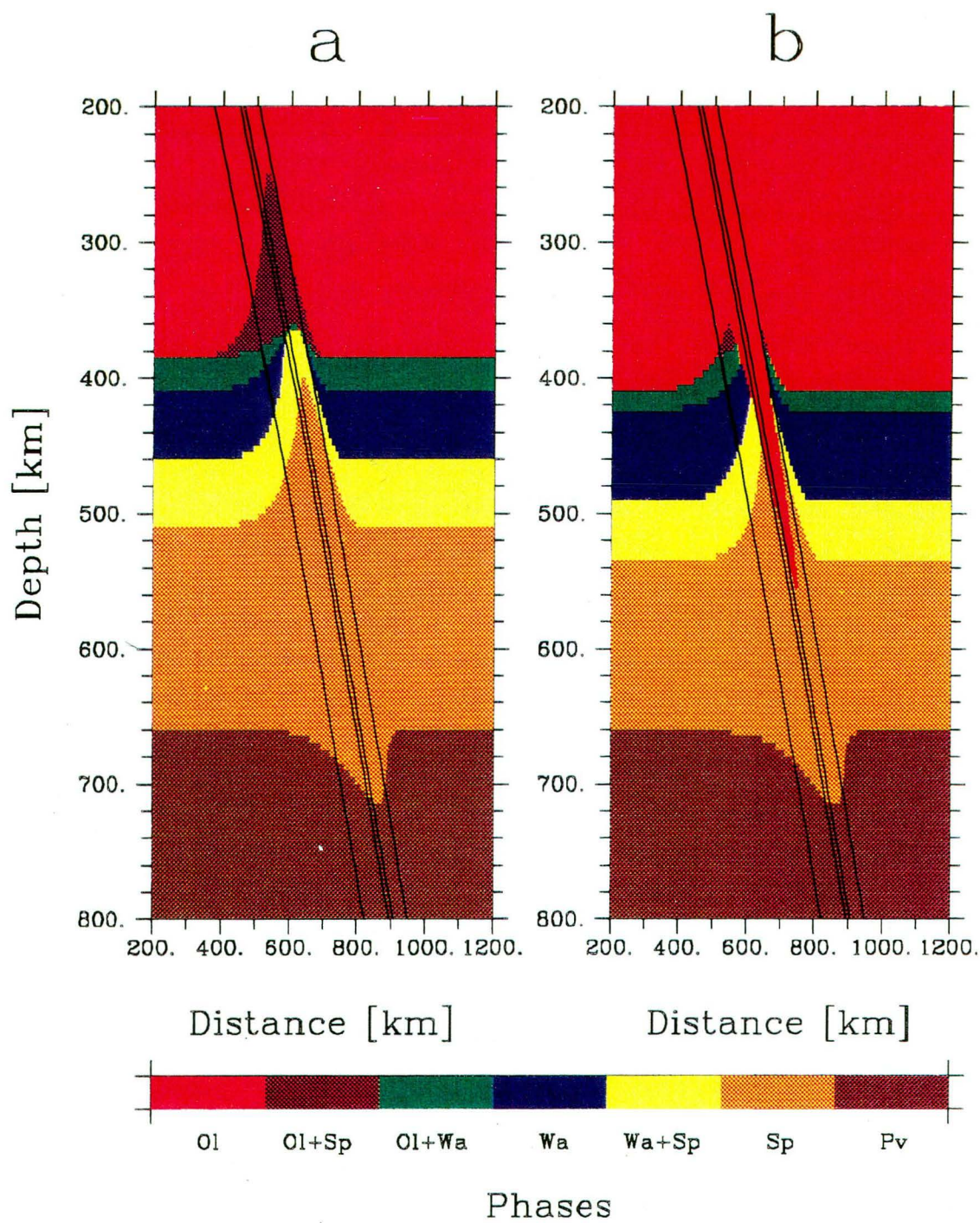
Fig. 6.2. Phase fields of $(Mg,Fe)_2SiO_4$ in the thermal regime of the slab. Lines are the same as those in Figure 6.1. (a) Equilibrium model. (b) Metastable model.
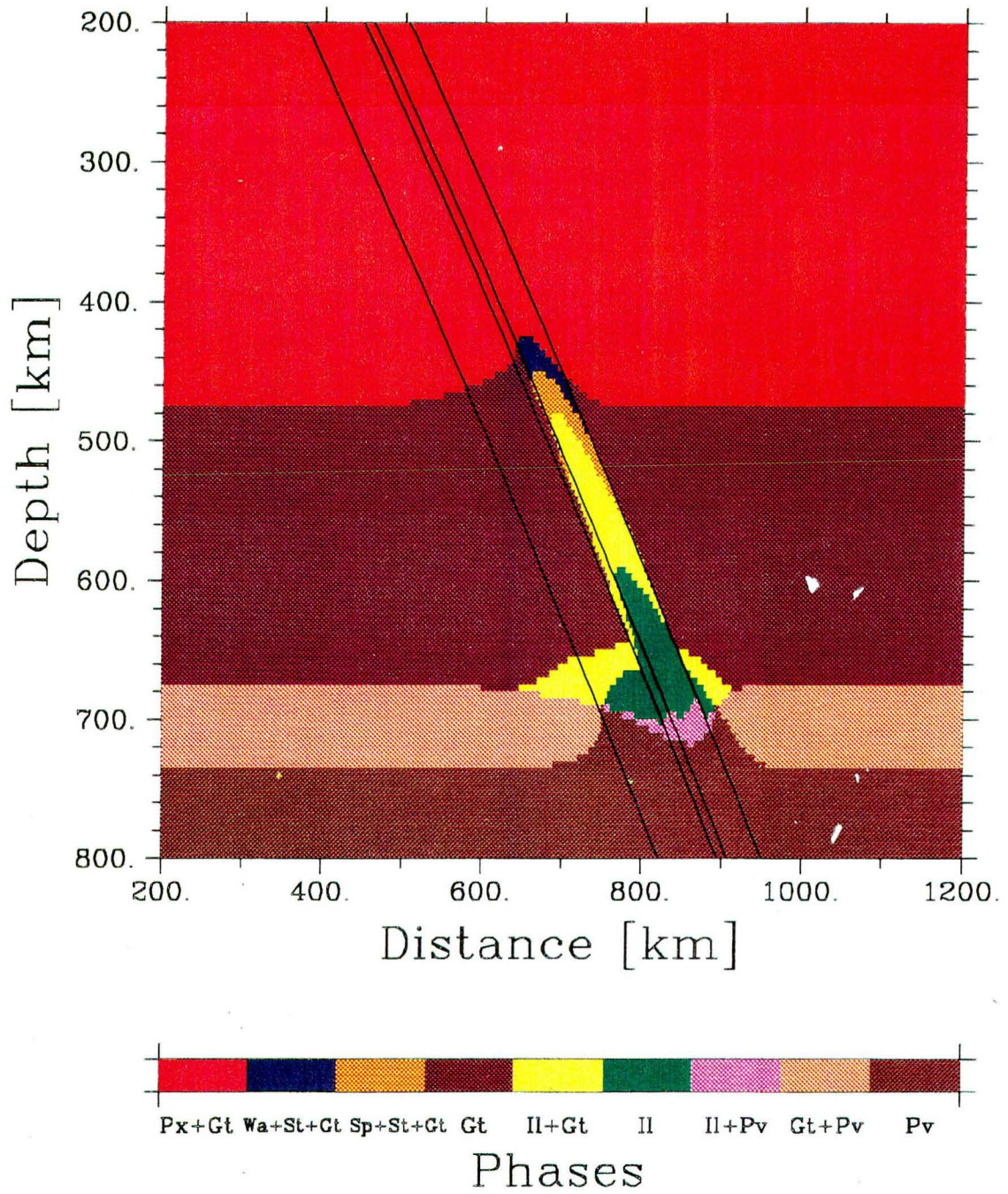
Fig. 6.3. Phase fields of the residuum in the thermal regime of the slab. Lines are the same as those in Figure 6.1.
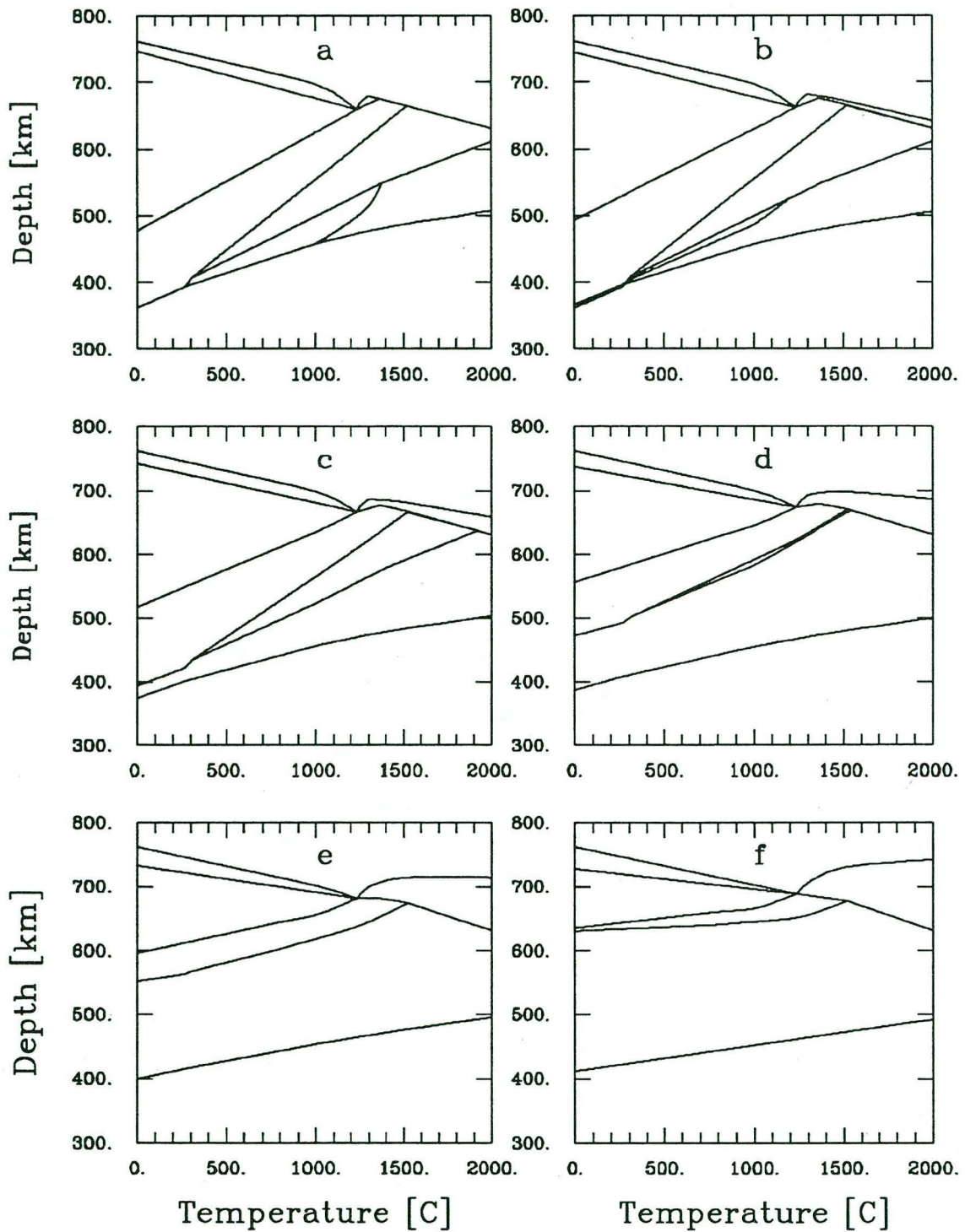
Fig. 6.4. Pressure - temperature diagrams for the residdum as a function of position from the top to the bottom of the lherozolite layer. Top of the layer (a), 90% from the top (b), 75% (c), 50% (d), 25% (e), bottom of the layer (f).

a
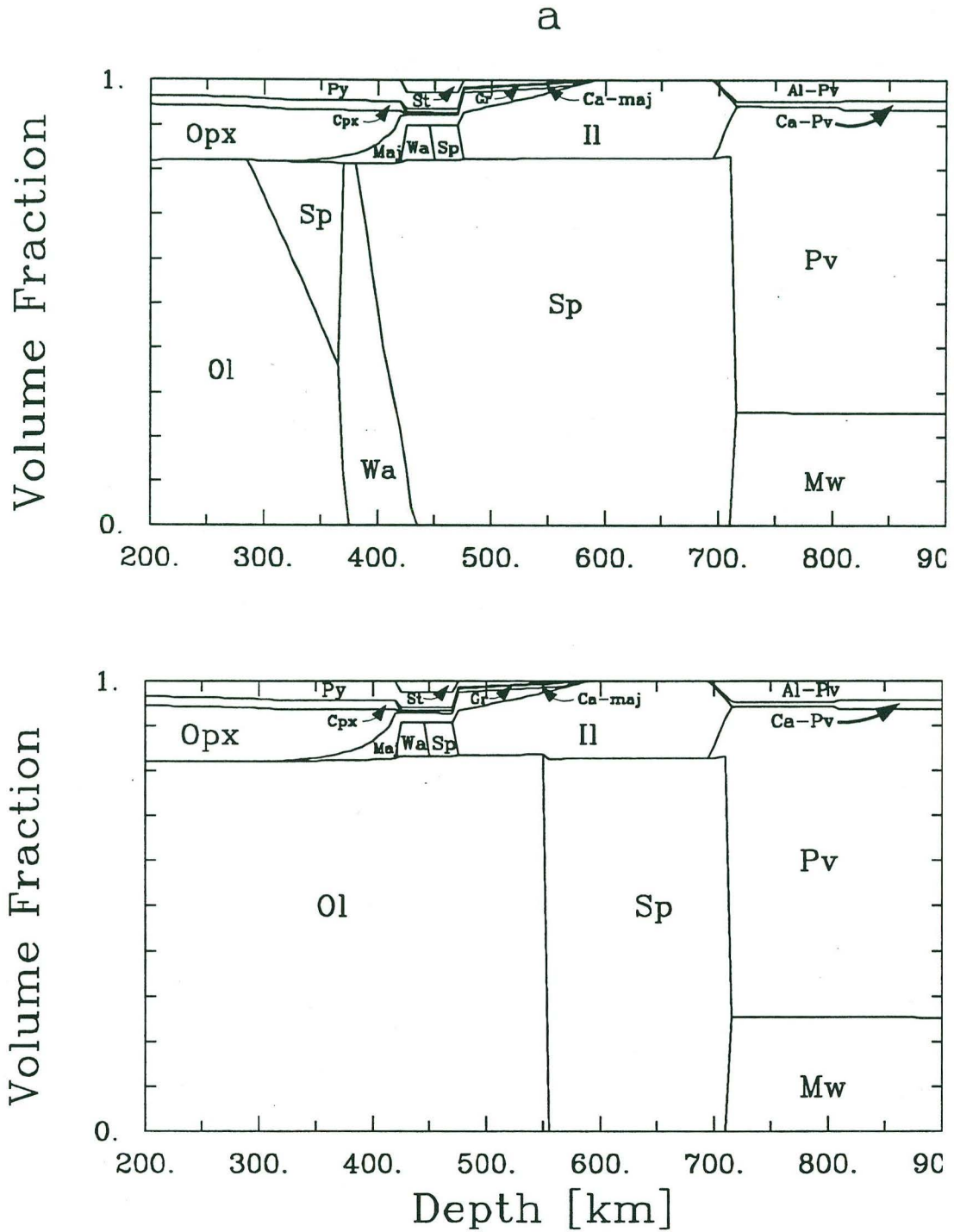
Fig. 6.5. Volume percentage of the minerals present in the cold core of the slab. (a) Equilibrium model. (b) Metastable model.

(Figure 6.5a). As we shall see below, this has great consequences for the velocity and density distribution within subducting slabs.

In addition, the position and types of phase fields vary significantly between the mantle and subducting slabs. Comparing Figure 6.5 with Figure 5.2, we see that the harzburgite layer contains fields of ilmenite, stishovite, wadsleyite and spinel not found in the pyrolite layer as well as a more restricted field of Al and Ca garnet. This is caused by the relative decreased in Ca and Al in the residuum component of harzburgite compared to that of pyrolite. Under equilibrium conditions, the olivine to wadsleyite transition is shifted upward by approximately 30 km and the spinel to perovskite transition is shifted downward by 50 km due to the thermal gradient between the slab geotherm and that of the mantle.

6.3   Velocity and Density Structure

The velocities calculated along the geotherm are shown in figure 6.6. Assuming equilibrium conditions in the olivine system, the core of the slab is faster the surrounding mantle throughout the upper mantle (Figure 6.6a). A ramp in the velocity extends from 290 km to 370 km depth due to the stabilization of the spinel phase at low temperature. The "400" km discontinuity (olivine to wadsleyite transition) appears at this point. The transition is sharper in the cold core though the velocity jump is greatly reduced. Next, a small jump seen near 425 km depth due to formation of stishovite in the harzburgite residuum. The velocity jump at the "650" km discontinuity is shifted downward with the delayed spinel to perovskite transition mentioned above. Metastable conditions alter the velocities significantly. Elevated velocities remain in the uppermost mantle, but the increase in velocity below 300 km is suppressed due to the persistence of olivine. In the upper half of the transition the velocity returns to that normally seen in the mantle. Near 550 km depth, the transition to spinel occurs and the velocity returns to the level predicted for the equilibrium assemblage.

Effects of mineralogy and temperature is best seen in the complete velocity profile of the slab shown in Figure 6.7. The velocity gradient in the pyrolite layer of the slab is purely a thermal effect. As noted above, the large increase in velocity just above 400 km depth in figure 6.7a is due to the stabilization of wadsleyite and spinel by the decrease in temperature (Figure 6.2a). The sudden increase in

a

b

Depth [km]
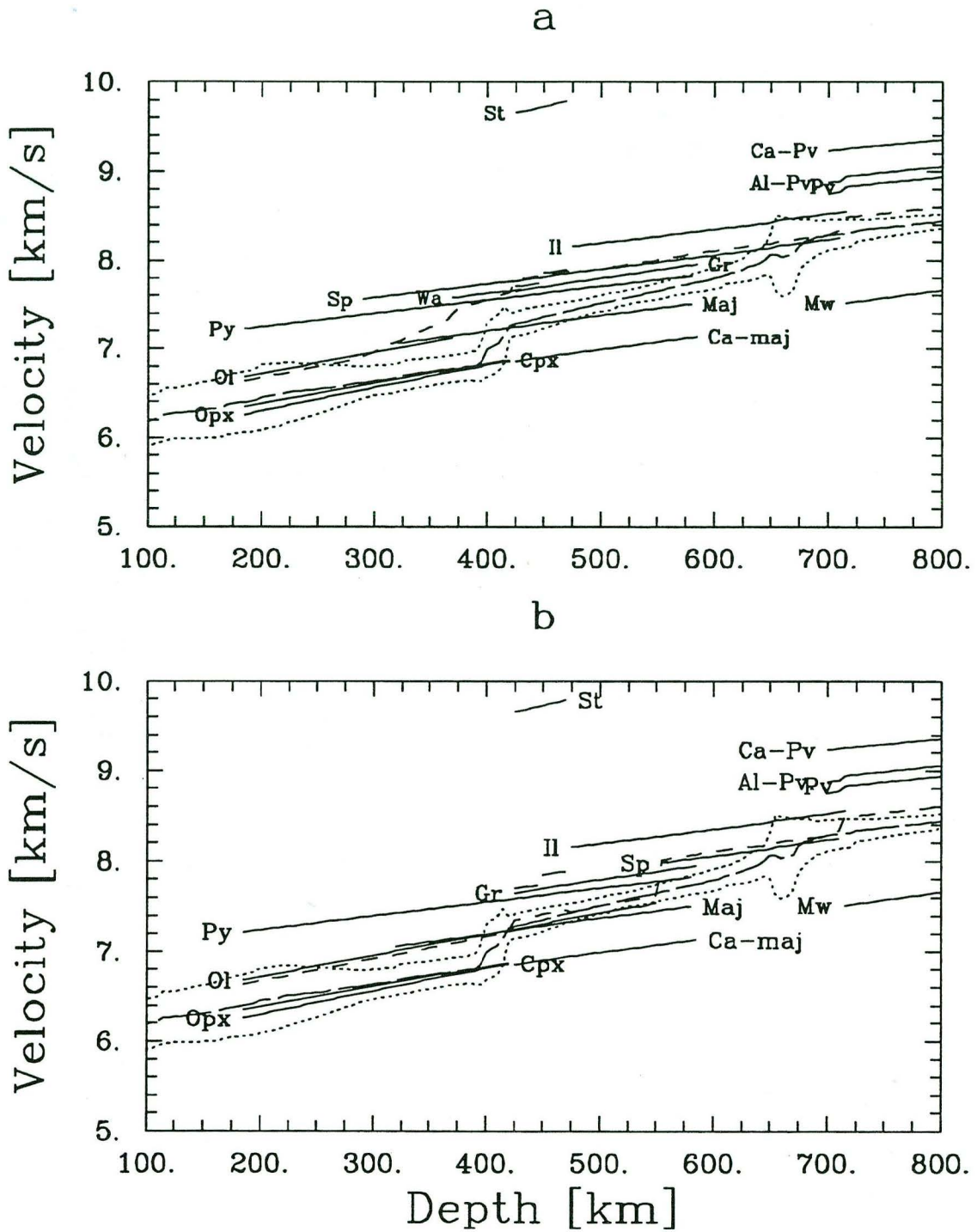
Fig. 6.6. Comparison of the predicted velocities of the individual minerals (solid lines) present in the cold core of the slab and their composite value (short-dashed line) with the mean (long-dashed line) and standard deviation (dotted line) of the mantle. (a) Equilibrium model. (b) Metastable model.
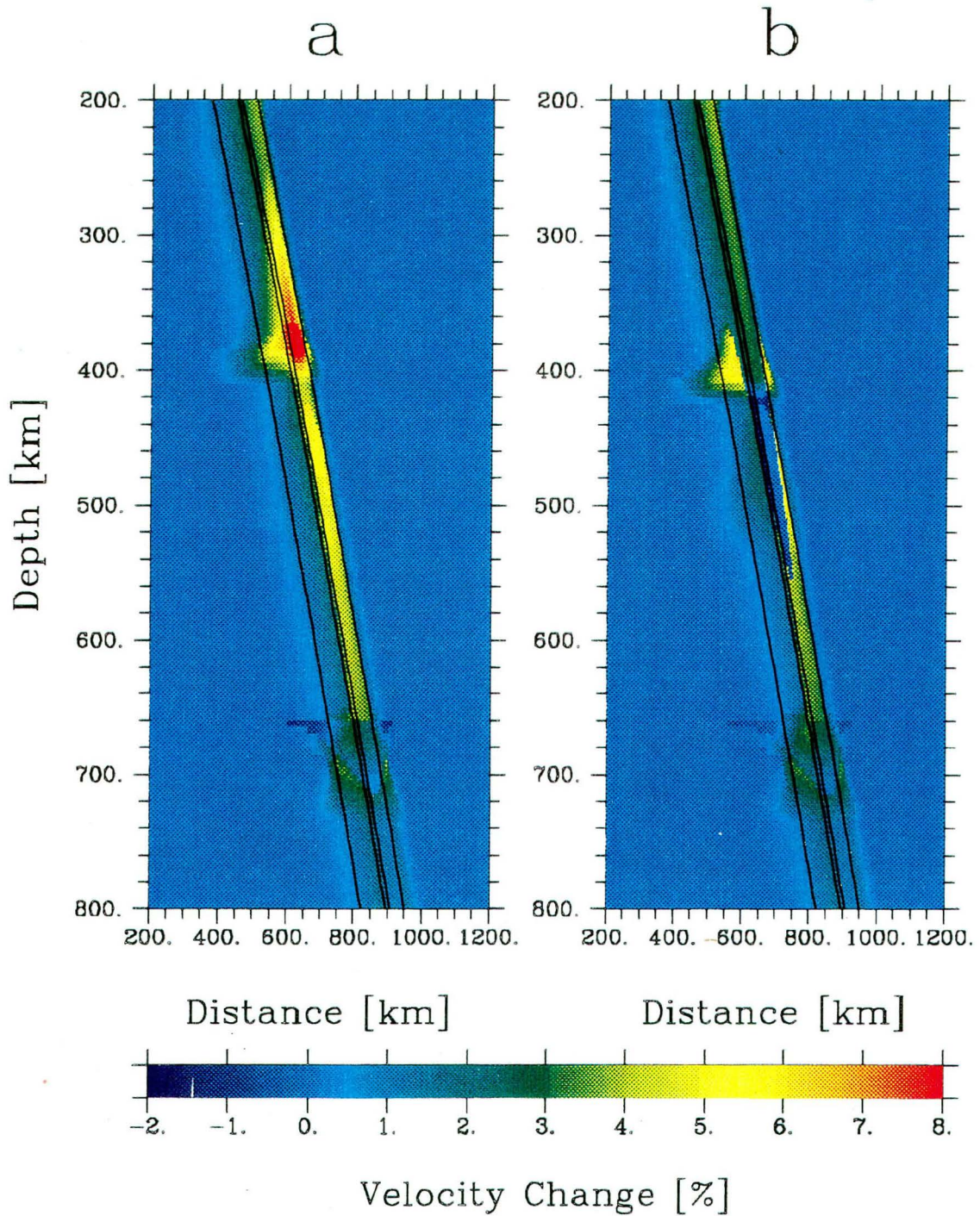
Fig. 6.7. Velocity profile of the subducting slab and surrounding mantle. (a) Equilibrium model. (b) Metastable model.

gradient in the harzburgite layer below 400 km is caused by the introduction of higher velocity phases such as wadsleyite, spinel and ilmenite at the expense of lower velocity garnets and pyroxenes. Between 660 and 710 km, the the velocity contrast drops due to the thermal depression of the spinel to perovskite transition. Below this point the velocities in the harzburgite layer are slightly lower than the immediately surrounding material. This is attributed to the increased magnesiowüstite to perovskite ratio associated with the greater olivine component in this layer. The presence of metastable olivine obliterates most of the higher velocities regions just above 400 km depth (Figure 6.7b). Below this point, the higher velocity ilmenite material offsets the presence of lower velocity olivine resulting in near normal mantle velocity profile. The appearance of higher velocities near 550 km depth marks the dissolution of olivine to spinel.

Density in the subduction region has the same character as velocity. As with velocity, very elevated contrasts are found just above 400 km under equilibrium conditions (Figure 6.8). In the metastable model, the velocity contrast approaches zero below 400 km depth while the density contrast actually becomes negative. Below 660 km, the contrast decreases and the value actually becomes negative there as well. Near 710 km, the contrast again becomes positive, but tends to more neutral values in the harzburgite layer in response to the increased amount of the olivine component.

6.4 Discussion

It is clear from the previous analysis that isobaric phase changes can have a strong effect on the velocity structure in subducting slabs. The thermal variation of phase assemblages gives rise to strong, short wavelength velocity anomalies both laterally and vertically within the slab. Whether the equilibrium or metastable model is most representative of slab behavior is unclear. Tomographic images of downgoing slabs on the Asian side of the Pacific rim show both kinds of behavior [*Zhou and Clayton,* 1990; *van der Hilst et al.,* 1991; *Fukao et al.,* 1992]. Resolution tests indicate that the structure can be imaged between 400 and 600km depth. However, large block sizes and disadvantageous source-receiver geometry may preclude the detection of the narrow, reduced velocity contrast predicted by the metastable model in some instances. The same arguments could also be used to explain metastable like anomalies seen in these regions. Regardless, the metastable model provides an explanation for the
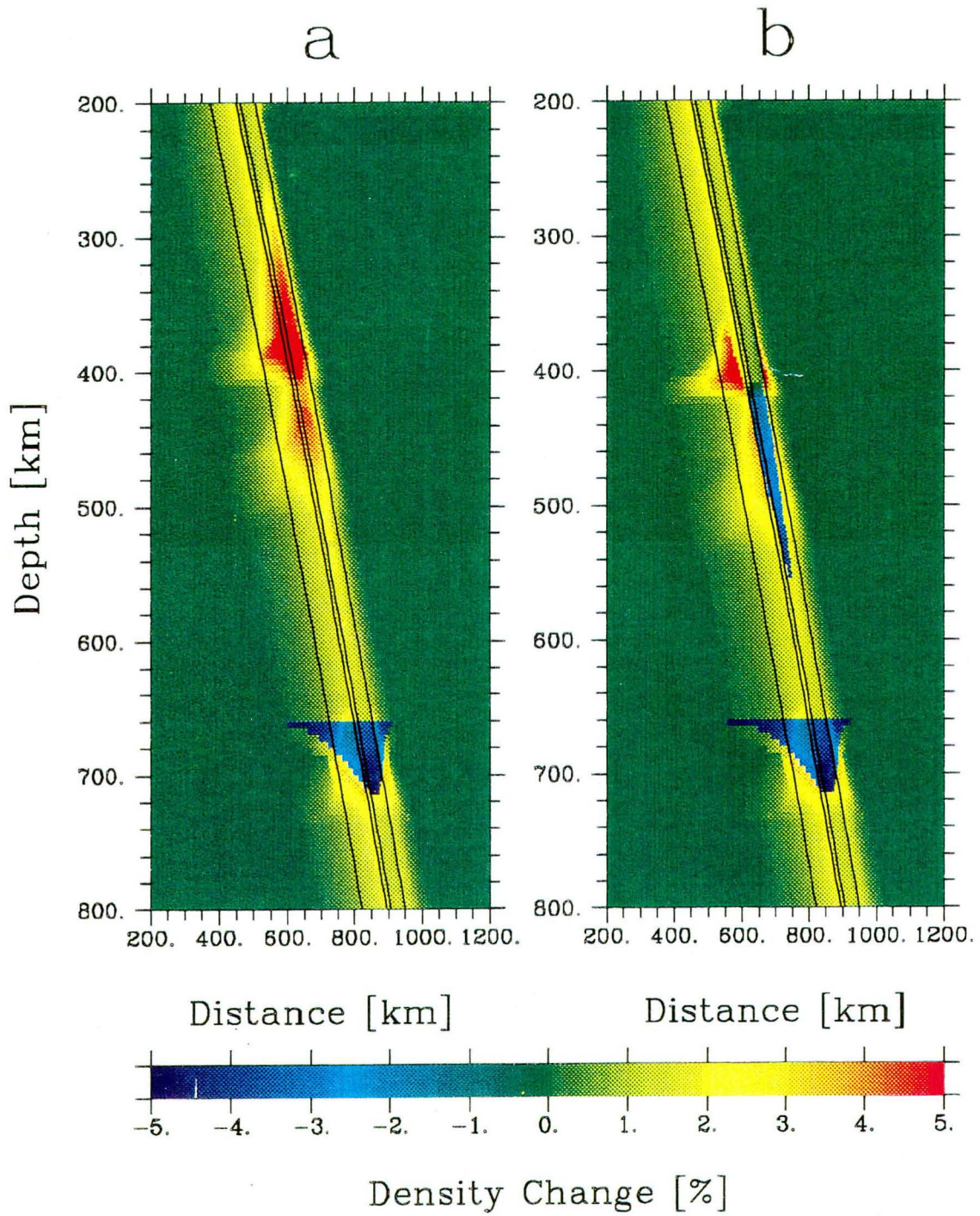
Fig. 6.8. Density profile of the subducting slab and surrounding mantle. (a) Equilibrium model. (b) Metastable model.

reduced velocity zones without invoking more ad hoc arguments such as detachment of the lower part of the slab from the upper.

The high variability in velocity contrast in subduction zones could also affect studies of depth penetration of subducting slabs mentioned in chapter one. These studies considered only the thermal perturbations to velocity in their analysis. Such an assumption may be justified for very deep earthquakes (>600 km depth) but conclusions based on shallower events should be treated with scepticism.

Fluctuations in the density profile also have important implications for the dynamics and structure of the Earth's interior. Recently, *Machetel and Weber* [1991] have demonstrated that an endothermic phase with a Clapeyron slope similar to that of the spinel to perovskite transition gives rise to layered convection. Surprisingly, studies by *Peltier and Solhiem* [1992] and *Zhao et al.* [1992] indicate that exothermic phase changes in the upper mantle do not hinder, and may actually encourage, dynamic layering in the mantle. A common element in these investigations is that they assume that the viscosity of the mantle is constant. The very presence of tectonic plates clearly shows that this assumption does not hold for the Earth. *King* [1991] found that a temperature dependent viscosity allowed slabs to penetrate chemical boundaries more easily than constant viscosity models. The increased strength of the slab allows the integrated body force on the slab caused by it's temperature induced rise in density to be transmitted downward allowing the slab to pierce the boundary. Constant viscosity models localize the effect of the mass anomalies in the slab decoupling them from one another.

Given that subduction mass anomalies most likely affect one another, the behavior of the olivine subsystem will be instrumental in controlling the style of mantle convection. A system in equilibrium will produce a slab with elevated densities overlying the negative density perturbation found between 650 and 700 km depth. This system would require a strongly endothermic phase transition to arrest its downward descent. Alternatively, the metastable model contains negative densities higher in the profile. The presence of the metastable wedge would partially offset the effect of the positive anomalies reducing the value of the Clapeyron slope needed to induce mantle layering. More realistic convection models are needed to quantify the importance of multiple phase transitions in the Earth, but their general character should be similar to that described here.

Chapter 7

Conclusions

Proposed upper mantle compositions are evaluated here using a potential formulation to accurately assess most thermodynamic properties of interest. This formulation allows a self-consistent calculation of temperature, density and velocity profiles throughout the mantle. The physical basis of the formulation allows the use of a minimal number of input parameters and reduces the reliance on estimates of the pressure and temperature dependance of elastic constants which are unknown for most minerals thought to exist in the mantle. Both the Birch-Murnaghan and Univeral equation of state are employed in the thermodynamic potentials, but the results of this investigation prove insensitive to the form used.

Comparisons are made between the predicted and expected properties taking into account their associated uncertainties. Uncertainties in the predicted properties are produced by propagating errors in the input parameters through the thermodynamic potentials. Given the lack of error estimates of the expected properties from previous investigations with adequate resolution, they are estimated here based on the statistical properties of profiles published in the geophysical literature.

These comparisons show that pyrolite-like compositions (A) agree very well with seismically observed properties throughout the upper mantle and transition zone. A piclogite-like composition (C) also matches the seismic data primarily because its high Al content causes the pyroxene to garnet transition to occur near the 400 km discontinuity. Olivine-poor, pyroxene-rich compositions (B) significantly underestimate velocities and densities between 400 and 500 km. Thus, seismic and mineral physics data are able to reject some models but they cannot uniquely determine the composition of the transition zone given their present precision. Consideration of shear wave velocities may further limit the range of acceptable compositions. The lack of laboratory measurements of shear moduli under mantle pressure conditions currently limits this approach.

One common element between the compositions considered here is the presence of anomalous velocity gradients near 18 GPa due to the transformation of garnet to Ca-perovskite. This transformation may explain the proposed 520 km seismic discontinuity. The chemical models also equally reject the possibility of chemical layering in the upper mantle.

Adiabats which yield the best agreement above 670 km lead to disagreement with expected profiles in the lower mantle, although possible biases in the density profile may obviate this conclusion. The high bulk sound velocity of Ca-perovskite causes overestimated velocities in the upper part of the lower mantle for all compositions, though this difference is only significant for compositions B and C. A thermal boundary layer at 670 km considerably strengthens the possibility of chemical segregation, so that a dynamically stratified isochemical mantle is highly unlikely. If the mantle is dynamically and compositionally stratified, the lower mantle is mostly likely enriched in SiO_2 and/or FeO components.

Thermally and chemically induced isobaric phase changes are found to have a significant effect on the density and velocity structure of subducting slabs. A mantle which is in thermodynamic equilibrium predicts elevated contrasts within subduction zones throughout the upper mantle except near the 670 km discontinuity, where the depression of the perovskite phase boundary allows spinel to persist to 710 km depth resulting in neutral to negative contrasts. Alternatively, kinetic hindrance of the olivine to spinel phase transtions also produces neutral to negative contrasts below 400 km depth. The variations in velocity seen in the upper mantle induced by changes in mineralogy indicate that modeling of the thermal perturbation to velocity, an assumption made in most seismic studies of subduction zones to date, is inadequate. Density variations will have a noticable impact on convective dynamics. An equilibrium phase assemblage will retard the formation of dynamic stratification while the metastable presence of olivine would encourage its formation. Convective modelling which accounts for phase induced changes in density is needed to clarify what consequences this has for the structure of the Earth's interior.

REFERENCES

Akaogi, M., and S. Akimoto, Pyroxene-garnet solid-solution equilibria in the systems $Mg_4Si_4O_{12} - Mg_3Al_2Si_3O_{12}$ and $Fe_4Si_4O_{12} - Fe_3Al_2Si_3O_{12}$ at high pressures and temperatures, *Phys. Earth Planet. Inter., 15,* 90-106, 1977.

Akaogi, M., and S. Akimoto, High-Pressure phase equilibria in a garnet lherzolite, with special reference to $Mg^{2+} - Fe^{2+}$ partitioning among constituent minerals, *Phys. Earth Planet. Inter., 19,* 31-51, 1979.

Akaogi, M., E. Ito, and A. Navrotsky, Olivine - modified spinel - spinel transitions in the system $Mg_2SiO_4 - Fe_2SiO_4$: Calorimetric measurements, Thermochemical calculation, and geophysical application,
J. Geophys. Res., 94, 15671-15686, 1989.

Akaogi, M., A. Navrotsky, T. Yagi, and S. Akimoto, Pyroxene-garnet transition: Thermochemistry and elasticity of garnet solid solutions, an application to a pyrolite mantle, in *High Pressure Research in Mineral Physics,* edited by M. H. Manghnani and Y. Syono, pp. 427-438, TERRAPUB/AGU, Tokoyo/Washington, 1987.

Allègre, C. J., and D. L. Turcotte, Geodynamic mixing in the mesosphere boundary layer and the origin of oceanic islands, *Geophys. Res. Lett., 12,* 207-210, 1985.

Anderson, D. L., Phase change in the upper mantle, *Science, 157,* 1165-1173, 1967.

Anderson, D. L., Thermally induced phase changes, lateral heterogeneity of the mantle, continental roots, and deep slab anomalies, *J. Geophys. Res., 92,* 13,968-13,980, 1987.

Anderson, D. L., Composition of the Earth *Science, 243,* 367-370, 1989.

Anderson, D. L., and J. D. Bass, Mineralogy and composition of the upper mantle *Geophysical Research Letters, 11,* 637-640, 1984.

Anderson, D. L., and J. D. Bass, Transition region of the Earth's upper mantle, *Nature, 320,* 321-328, 1986.

Ashida, T., S. Kume, and E. Ito, Thermodynamic aspects of phase boundary among α, β, and γ Mg_2SiO_4 , in *High Pressure Research in Mineral Physics,* edited by M. H. Manghnani and Y. Syono, pp. 427-438, TERRAPUB/AGU, Tokoyo/Washington, 1987.

Ashida, T., S. Kume, E. Ito, and A. Navrotsky, $MgSiO_3$ ilmenite: Heat capacity, thermal expansivity, and enthalpy of transformation, *Phys. Chem. Min., 16,* 239-245, 1988.

Bass, J. D., Elasticity of grossular and spessartite garnets by Brillouin spectroscopy, *J. Geophys. Res., 94,* 7621-7628, 1989.

Bass, J. D., and D. L. Anderson, Composition of the upper mantle: Geophysical tests of two petrological models, *Geophysical Research Letters, 11,* 229-232, 1984.

Bass, J. D. and M. Kanzaki, Elasticity of a majorite-pyrope solid solution, *Geophys. Res. Lett., 17,* 1989-1992, 1990.

Bass, J. D., R. C. Liebermann, D. J. Weidner, and S. J. Finch, Elastic Properties from acoustic and volume compression experiments, *Phys. Earth Planet. Int., 25,* 140-158, 1981.

Bass, J. D. and D. J. Weidner, Elasticity of single-crystal orthoferrosilite, *J. Geophys. Res., 89,* 4359-4371, 1984.

Bernal, J. D., *Observatory, 59,* 268, 1936.

Bessonova, E. N., V. M. Fishman, L. R. Johnson, M. G. Shnirman, and G. A. Sitnikova, The tau method for inversion of travel times II. Earthquake data, *Geophys. J. R. astr. Soc., 36,* 377-398, 1976.

Bevington, P. R., *Data Reduction and Error Analysis for the Physical Sciences,* 336 pp., McGraw-Hill, New York, 1969.

Bina, C. R. and P. G. Silver, Constraints on lower mantle composition and temperature from density and bulk sound velocity profiles, *Geophys. Res. Lett., 17,* 1153-1156, 1990.

Bina, C. R. and B. J. Wood, Olivine-spinel transitions: Experimental and thermodynamic constraints and implications for the nature of the 400 km seismic discontinuity, *J. Geophys. Res., 92,* 4853-4866, 1987.

Birch, F., Elasticity and constitution of the Earth's interior, *J. Geophys. Res., 57,* 227-286, 1952.

Bock, G., and R. Kind, A global survey of S to P and P to S conversions in the upper mantle transition zone, *Geophys. J. Int., 107,* 117-129, 1991.

Bowman, J. R., and B. L. N. Kennett, An investigation of the upper mantle beneath NW Australia using a hybrid seismograph array, *Geophys. J. Int., 101,* 411-424, 1990.

Buchbinder, G. G. R., A Velocity Structure of the Earth's Core, *Bull. Seis. Soc. Am., 61,* 429-456, 1971.

Bukowinski, M. S. T., and G. H. Wolf, Thermodynamically consistent decompression: Implications for lower mantle composition, *J. Geophys. Res., 95,* 12583-12593, 1990.

Burdick, L. J., A comparison of the upper mantle structure beneath north America and Europe, *J. Geophys. Res., 86,* 5926-5936, 1981.

Burdick, L. J., and D. L. Anderson, Interpretation of velocity profiles of the mantle, *J. Geophys. Res., 80,* 1070-1074, 1975.

Burdick, L. J., and D. V. Helmberger, The upper mantle P velocity structure of the western United States, *J. Geophys. Res., 83,* 1699-1712, 1978.

Butler, R., and D. L. Anderson, Equation of state fits to the lower mantle and outer core, *Phys. Earth Planet Inter., 17,* 147-162, 1978.

Callen, H. B., *Thermodynamics and an introduction to thermostatistics*, 493 pp., John Wiley & Sons, New York, 1985.

Cameron, M., S. Sueno, C. T. Prewitt and J. J. Papike, High-temperature crystal chemistry of acmite, diopside, hedenbergite, jadeite, spodumene, and ureyite, *Am. Mineral.*, *58*, 594-618, 1973.

Chinnery, M. A., and M. N. Toksoz, P-wave velocities in the mantle below 700 km, *Bull. Seis. Soc. Am.*, *57*, 199-226, 1967.

Craven, P., and G. Wahba, Smoothing noisy data with spline functions, *Numerische Mathematik*, *31*, 377-403, 1979.

Creager, K. C., and T. H. Jordan, Slab penetration into the lower mantle, *J. Geophys. Res.*, *89*, 3031-3049, 1984.

Creager, K. C., and T. H. Jordan, Slab penetration into the lower mantle beneath the Mariana and other island arcs of the northwest pacific, *J. Geophys. Res.*, *91*, 3573-3589, 1986.

Cummins, P. R., B. L. N. Kennett, J. R. Bowman, and M. G. Bostock, The 520 Km discontinuity?, *Bull. Seis. Soc. Am.*, *82*, 323-336, 1992.

DePaolo, D. J., Geochemical evolution of the crust and mantle, *Revs. Geophys. Space Phys.*, *21*, 1347-1358, 1983.

Derr, J. S., Internal structure of the Earth inferred from free oscillations, *J. Geophys. Res.*, *74*, 5202-5220, 1969.

Dey-Sarkar, S. K., and R. A. Wiggins, Upper mantle structure in western Canada, *J. Geophys. Res.*, *81*, 3619-3632, 1976.

Dost, B., Upper mantle structure under western Europe from fundamental and higher mode surface waves using the NARS array, *Geophys. J. Int.*, *100*, 131-151, 1990.

Duffy, T. S., and D. L. Anderson, Seismic velocities in mantle minerals and the mineralogy of the upper mantle, *J. Geophys. Res.*, *94*, 1895-1912, 1989.

Dziewonski, A. M., and D. L. Anderson, Preliminary reference Earth model, *Phys. Earth Planet. Inter.*, *25*, 297-356, 1981.

Fairborn, J. W., Shear wave velocities in the lower mantle, *Bull. Seis. Soc. Am.*, *59*, 1983-1999, 1969.

Fei, Y., H. K. Mao, B. O. Mysen, Experimental determination of element partitioning and calculation of phase relations in the $MgO-FeO-SiO_2$ system at high pressure and high temperature, *J. Geophys. Res.*, *96*, 2157-2170, 1991.

Fei, Y., H. K. Mao, J. Shu, G. Parthasarathy, W. Bassett, and J. Ko, Simultaneous high-P, high-T X-ray diffraction study of β - $(Mg,Fe)_2SiO_4$ to 26 GPa and 900 K, *J. Geophys. Res.*, *97*, 4489-4496, 1992.

Finger, L. W., and Y. Ohashi, The thermal expansion of diopside to 800 C and a refinement of the crystal structure at 700 C. *Am. Mineral., 61,* 303-310, 1976.

Fischer, K. M., K. C. Creager, and T. H. Jordan, Mapping the Tonga slab, *J. Geophys. Res., 96,* 14403-14427, 1991.

Fukao, Y., Upper mantle P structure on the ocean side of the Japan-Kurile arc, *Geophys. J. R. astr. Soc., 50,* 621-642, 1977.

Fukao, Y., T. Nagahashi, and S. Mori, Shear velocity in the mantle transition zone, in *High Pressure Research in Geophysics,* by S. Akimoto and M. H. Manghnani, Center for Academic Publications, Tokyo, Japan, 1982.

Fukao, Y., M. Obayashi, H. Inoue, and M. Nenbai Subducting slabs stagnant in the mantle transition zone, *J. Geophys. Res., 97,* 4809-4822, 1992.

Gaherty, J. B., T. Lay, and J. E. Vidale, Investigation of deep slab structure using long-period S waves, *J. Geophys. Res., 96,* 16349-16367, 1991.

Gasparik, T., Phase relations in the transition zone, *J. Geophys. Res., 95,* 15751-15769, 1990.

Giardini, D., and J. H. Woodhouse, Deep seismicity and modes of deformation in Tonga subduction zone, *Nature, 307,* 505-509, 1984.

Giardini, D., and J. H. Woodhouse, Horizontal shear flow in the mantle beneath the Tonga arc, *Nature, 319,* 551-555, 1986.

Gilbert, F., and A. M. Dziewonski, An application of normal mode theory to the retrieval of structural parameters and source mechanisms from seismic spectra, *Phil. trans. Royal Soc., London A, 278,* 187-269, 1975.

Gilbert, F., A. M. Dziewonski, and J. Brune, An information solution to a seismological inverse problem, *Proc. Natl. Acad. Sci. USA, 70,* 1410-1413, 1973.

Given, J. W., and D. V. Helmberger, Upper mantle structure of northwestern Eurasia, *J. Geophys. Res., 85,* 7183-7194, 1980.

Grad, M., Seismic model of the Earth's crust and upper mantle for the east European platform, *Phys. Earth Planet. Inter., 51,* 182-184, 1988.

Graham, E., and G. Barsch, Elastic constants of single-crystal forsterite as a function of temperature and pressure, *J. Geophys. Res., 74,* 5949-5960, 1969.

Graham, E., J. Schwab, S. Sopkin, and H. Takei, The pressure and temperature dependence of the elastic properties of single-crystal fayalite Fe_2SiO_4 , *Phys. Chem. Miner., 16,* 186-198, 1988.

Grand, S. P., and D. V. Helmberger, Upper mantle shear structure of North America, *Geophys. J. R. astr. Soc., 76,* 399-438, 1984a.

Grand, S. T., and D. V. Helmberger, Upper mantle shear structure beneath the northwest Atlantic ocean, *J. Geophys. Res., 89*, 11465-11475, 1984b.

Graves, R. W., and D. V. Helmberger, Upper mantle cross section from Tonga to Newfoundland, *J. Geophys. Res., 93*, 4701-4711, 1988.

Guggenheim, E. A., *Mixtures,* 270 pp., Clarendon, Oxford, 1952.

Gurnis, M., and G. F. Davies, Mixing in numerical models of mantle convection incorporating plate kinematics, *J. Geophys. Res., 91*, 6375-6395, 1986.

Gurnis, M., and B. H. Hager, Controls of the structure of subducted slabs, *Nature, 335*, 317-321, 1988.

Gwanmesia, G., S. Rigden, I. Jackson, and R. Liebermann, Pressure dependence of elastic wave velocity for $\beta-Mg_2SiO_4$ and the composition of the Earth's mantle. *Science, 250*, 794-797, 1990.

Haddon, R. A. W., and K. E. Bullen, An Earth model incorporating free oscillation data, *Phys. Earth Planet. Inter., 2*, 35-49, 1969.

Hager, B. H., Subducted slabs and the geoid: Constraints on mantle rheology and flow, *J. Geophys. Res., 89*, 6003-6015, 1984.

Hager, B. H., and M. A. Richards, Long-wavelength variations in Earth's geoid: Physical models and dynamical implications, *Philos. Trans. R. Soc. London, Ser. A, 328*, 309-327, 1989.

Haggerty, S. E., and V. Sautter, Ultradeep (greater than 300 kilometers), ultramafic upper mantle xenoliths, *Science, 248*, 993-996, 1991.

Hales, A. L., J. R. Cleary, and J. L. Roberts, Velocity distributions in the lower mantle, *Bull. Seis. Soc. Am., 58*, 1975-1989, 1968.

Hales, A. L., K. J. Muirhead, and J. M. W. Rynn, A compressional velocity distribution for the upper mantle, *Tectonophysics, 63*, 309-348, 1980.

Hales, A.L., and J.L. Roberts, Shear velocities in the lower mantle and the radius of the core, *Bull. Seis. Soc. Am., 60*, 1427-1436, 1970.

Hart, R. S., Shear velocity in the lower mantle from explosion data, *J. Geophys Res., 80*, 4889-4894, 1975.

Hart, R. S., D. L. Anderson, and H. Kanamori, Shear velocity and density of an attenuating Earth, *Earth Planet. Sci. Let., 32*, 25-34, 1976.

Haselton, H. T., and R. C. Newton Thermodynamics of pyrope-grossular garnets and their stabilities at high temperatures and high pressures, *J. Geophys. Res., 85*, 6873-6982, 1980.

Hashin, Z., and S. Shtrikman, A variational approach to the elastic behavior of multiphase materials, *J. Mech. Phys. Solids, 11*, 127-140, 1963.

Hazen, R. M., J. Zhang, and J. Ko, Effects of Fe/Mg on the compressibility of synthetic wadsleyite: $\beta - (Mg_{1-x}Fe_x)SiO_4$ (x < 0.25), *Phys. Chem. Min., 17*, 416-419, 1990.

Hemley, R. J., L. Stixrude, Y. Fei, and H. K. Mao, Constraints on lower mantle composition from P-V-T measurements of $(Fe,Mg)SiO_3$ perovskite and $(Fe,Mg)O$ magnesiowüstite, in *High Pressure Research: Application to Earth and Planetary Sciences*, edited by Y. Syono and M. H. Manghnani (in press), 1992.

Herrin, E. Introduction to "1968 Seismological Tables for P Phases" *Bull. Seis. Soc. Am., 58*, 1193-1242, 1968.

Irifune, T., An experimental investigation of the pyroxene - garnet transformation in a pyrolite composition and its bearing on the constitution of the mantle, *Phys. Earth Planet. Inter., 45*, 324-336, 1987.

Irifune, T., and A. E. Ringwood, Phase transformations in a harzburgite composition to 26 GPa: implications for dynamical behaviour of the subducting slab, *Earth Planet. Sci. Lett. ,, 86*, 365-376, 1987a.

Irifune, T., and A. E. Ringwood, Phase transformations in primitive MORB and pyrolite compositions to 25 GPa and some geophysical implications, in *High Pressure Research in Mineral Physics*, edited by M. H. Manghnani and Y. Syono, pp. 427-438, TERRAPUB/AGU, Tokoyo/Washington, 1987b.

Irifune, T., J. Susaki, T. Yagi, and H. Sawamoto, Phase transformations in diopside $CaMgSi_2O_6$ at pressures up to 25 GPa, *Geophys. Res. Let., 16*, 187-190, 1989.

Isaak, D. G., O. Anderson, and T. Goto, Elasticity of single-crystal forsterite measured to 1700 K, *J. Geophys. Res., 94*, 5895-5906, 1989.

Isacks, B. L., and P. Molnar, Distribution of stresses in the descending lithosphere from a global survey of focal mechanism solutions of mantle earthquakes, *Rev. Geophys., 9*, 103-174, 1971.

Ita, J. J., and L. Stixrude, Petrology, Elasticity, and Composition of the Mantle Transition Zone, *J. Geophys. Res., 97*, 6849-6866, 1992.

Ito, E., and E. Takahashi, Ultrahigh - pressure phase transformations and the constitution of the deep mantle, in *High Pressure Research in Mineral Physics*, edited by M. H. Manghnani and Y. Syono, pp. 427-438, TERRAPUB/AGU, Tokoyo/Washington, 1987a.

Ito, E., and E. Takahashi, Melting of peridotite at uppermost lower-mantle conditions, *Nature, 328*, 514-517, 1987b.

Ito, E., and E. Takahashi, Postspinel Transformations in the system Mg_2SiO_4 - Fe_2SiO_4 and some geophysical implications, *J. Geophys. Res., 94*, 10637-10646, 1989.

Jackson, I., Some geophysical constraints on the chemical composition of the earth's lower mantle, *Earth Planet. Sci. Lett., 62*, 91-103, 1983.

Jackson, I., Elasticity and polymorphism of wüstite $Fe_{1-x}O$, *J. Geophys. Res.*, *95*, 21671-21685, 1990.

Jackson, I., and H. Niesler, The elasticity of periclase to 3 GPa and some geophysical implications, in *High Pressure Research in Geophysics*, edited by S. Akimoto and M. H. Manghnani, pp. 93-113, Center for Academic Publications, Tokoyo, 1982.

Jarrard, R. D., Relations among subduction parameters, *Rev. Geophys.*, *24*, 217-284, 1986.

Jeanloz, R., Shock wave equation of state and finite strain theory, *J. Geophys. Res.*, *94*, 5873-5886, 1989.

Jeanloz, R., and E. Knittle, Density and composition of the lower mantle, *Phil. Trans. R. Soc. Lond. A*, *328*, 377-389, 1989.

Jeanloz, R., and S. Morris, Temperature distribution in the crust and mantle, *Ann. Rev. Earth Planet. Sci.*, *14*, 377-415, 1986.

Jeanloz, R., and F. M. Richter, Convection, composition, and the thermal state of the lower mantle, *J. Geophys. Res.*, *84*, 5497-5504, 1979.

Jeanloz, R., and A. B. Thompson, Phase transitions and mantle discontinuities, *Rev. Geophys. Space. Phys.*, *21*, 51-74, 1983.

Jones, L. E., J. Mori, and D. V. Helmberger, Short-period constraints on the proposed transition zone discontinuity, *J. Geophys. Res.*, *97*, 8765-8774, 1992.

Jordan, T. H., and D. L. Anderson, Earth structure from free oscillations and travel times, *Geophys. J. R. astr. Soc.*, *36*, 411-459, 1974.

Kandelin, J., and D. J. Weidner, Elastic properties of hedenbergite, *J. Geophys. Res.*, *94*, 1063-1072, 1988.

Kanzaki, M., Ultrahigh - pressure phase relations in the system $Mg_4Si_4O_{12}$ - $Mg_3Al_2Si_3O_{12}$, *Phys. Earth Planet. Inter.*, 49, 168-175, 1987.

Kato, T., A. E. Ringwood, and T. Irifune, Experimental determination of element partitioning between silicate perovskites, garnets and liquids: constraints on early differentiation of the mantle, *Earth Planet. Sci. Lett.*, *89*, 123-145, 1988.

Katsura, T., and E. Ito, The system Mg_2SiO_4–Fe_2SiO_4 at high pressures and temperatures: Precise determination of stabilities of olivine, modified spinel, and spinel, *J. Geophys. Res.*, *94*, 15663-15670, 1989.

Kennett, B. L. N., and E. R. Engdahl, Traveltimes for global earthquake location and phase identification, *Geophys. J. Int.*, *105*, 429-465, 1991.

Kim, Y., L. C. Ming, and M. H. Manghnani, A study of phase transformation in hedenbergite to 40 GPa at 1200 ° C, *Phys. Chem. Minerals*, *16*, 757-762, 1989.

Kind, R., and G. Muller, Computations of SV waves in realistic Earth models, *J. Geophys., 4*, 149-172, 1975.

King, S. D., *The interaction of subducting slabs and the 670 kilometer discontinuity*, Phd. thesis, California Institute of Technology, Pasadena, 1991.

King, D. W., and G. Calcagnile, P-wave velocities in the upper mantle beneath Fennoscandia and western Russia, *Geophys. J. R. astr. Soc., 46*, 407-432, 1976.

Kirby, S. H., W. B. Durham, and L. A. Stern, Mantle phase changes and deep-earthquake faulting in subducting lithosphere, *Science, 252*, 216-225, 1991.

Knittle, E., R. Jeanloz, and G. L. Smith, Thermal expansion of silicate perovskite and stratification of the Earth's mantle, *Nature, 319*, 214-216, 1986.

Knittle, E., and R. Jeanloz, Synthesis and equation of state of $(Mg,Fe)SiO_3$ perovskite to over 100 gigapascals, *Science, 235*, 666-670, 1987.

Knopoff, L., and J. N. Shapiro, Comments on the interrelationships between Grüneisen's parameter and shock and isothermal equations of state, *J. Geophys. Res., 74*, 1439-1450, 1969.

Korn, M., P-wave coda analysis of short-period array data and the scattering and absorptive properties of the lithosphere, *Geophys. J. R. astr. Soc., 93*, 437-449, 1988.

Krupka, K. M., B. S. Hemingway, R. A. Robie, and D. M. Kerrick, High temperature heat capacities and derived thermodynamic properties of anthophyillite, diopside, dolomite, enstatite, bronzite, talc, tremolite, and wollastonite, *Am. Mineral., 70*, 261- 271, 1985.

Krupka, K. M., R. A. Robie, and B. S. Hemingway, High temperature heat capacities of corundum, periclase, anorthite, $CaAl_2Si_2O_8$ glass, muscovite, pyrophyillite, $KAlSi_3O_8$ glass, grossular, and $NaAlSi_3O_8$ glass, *Am. Mineral., 64*, 86-101, 1979.

Lay, T., and C. J. Young, The effect of SKS scattering on models of the shear velocity-structure of the D'' region, *J. Geophys., 59*, 11-15, 1986.

Lees, A. C., M. S. T. Bukowinski, and R. Jeanloz, Reflection properties of phase transitions and compositional change models of the 670-km discontinuity, *J. Geophys. Res., 88*, 8145-8159, 1983.

Lefevre, L. V., and D. V. Helmberger, Upper mantle P velocity structure of the Canadian shield, *J. Geophys. Res., 94*, 17749-17765, 1989.

Leger, J. M., A. M. Redon, and C. Chateau, Compressions of synthetic pyrope, spessartine and uvarovite garnets up to 25 GPa, *Phys. Chem. Minerals, 17*, 161-167, 1990.

Lerner-Lam, A. L., and T. H. Jordan, How Thick Are the Continents?, *J. Geophys. Res., 92*, 14,007-14026, 1987.

Leven, J. H., The application of synthetic seismograms to the interpretation of the upper mantle P - wave velocity structure in northern Australia, *Phys. Earth Planet. Int., 38*, 9-27, 1985.

Levien, L. R., and C. T. Prewitt, High pressure structural study of diopside, *Am. Mineral., 66*, 315-323, 1981.

Levien, L., D. J. Weidner, C. T. Prewitt, Elasticity of diopside, *Phys. Chem. Min., 4*, 105-113, 1979.

Liebermann, R. C., Elasticity of olivine (α), beta (β), and spinel (γ) polymorphs of germanates and silicates. *Geophys. J. R. astr. Soc., 42*, 899-929, 1975.

Lyon-Caen, H., Comparison of the upper mantle shear wave velocity structure of the Indian Shield and the Tibetan Plateau and tectonic implications, *Geophys. J. R. astr. Soc., 86*, 727-749, 1986.

McMechan, G. A., An amplitude constrained P-wave velocity profile for the upper mantle beneath the eastern United States, *Bull. Seis. Soc. Am., 69*, 1733-1744, 1979.

McMechan, G. A., Mantle P-wave velocity structure beneath Antarctica, *Bull. Seis. Soc. Am., 71*, 1061-1074, 1981.

McQueen, R. G., S. P.Marsh, J. W. Taylor, J. N. Fritz, and W. J. Carter, The equation of state of solids from shock wave studies, in *High Velocity Impact Phenomena*, edited by R. Kinslow, pp. 294-419, Academic, San Diego, 1970.

Machetel, P., and P. Weber, Intermittent layered convection in a model mantle with an endothermic phase change at 670 km, *Nature, 350*, 55-57, 1991.

Machetel, P., and D. A. Yuen, Penetrative convective flows induced by internal heating and mantle compressibility *J. Geophys. Res., 94*, 10609-10626, 1989.

Mao, H. K., L. C. Chen, R. J. Hemley, A. P. Jephcoat, Y. Wu, and W. A. Basset, Stability and equation of state of CaSiO$_3$ - perovskite to 134 GPa, *J. Geophys. Res., 94*, 17889-17894 , 1989.

Mao, H. K., R. J. Hemley, Y. Fei, J. F. Shu, L. C. Chen, A. P. Jephcoat, Y. Wu and W. A. Bassett, Effect of pressure, temperature and composition on lattice parameters and density of (Fe,Mg)SiO$_3$ -perovskites to 30 GPa, *J. Geophys. Res., 96*, 8069-8080, 1991.

Mizutani, H., and K. Abe, An Earth model consistent with free oscillation and surface wave data, *Phys. Earth Planet. Inter., 5*, 345-356, 1971.

Montagner, J., and D. L. Anderson, Constrained reference mantle model, *Phys. Earth Planet. Inter., 58*, 205-227, 1989.

Montagner, J. P., and T. Tanimoto, Global upper mantle tomography of seismic velocities and anisotropies, *J. Geophys. Res., 96*, 20337-20351, 1991.

Nakada, M., and M. Hashizume, Upper mantle structure beneath the Canadian shield derived from higher modes of surface waves, *J. Phys. Earth, 31*, 387-405, 1983.

Ohashi, Y., C. W. Burnham, and L. Finger, The effect of Ca-Fe substitution on the clinopyroxene crystal structure, *Am. Mineral., 60*, 423-434, 1975.

Ohashi, Y., and L. Finger, The effect of Ca substitution on the structure of clinoenstatite, *Carn. Inst. Wash. Yearbook,* 75, 743-746, 1976.

Ohtani, E., Chemical stratification of the mantle formed by melting in the early stage of the terrestrial evolution, *Tectonophysics, 154,* 201-210, 1988.

Olinger, B., Compression studies of forsterite (Mg_2SiO_4) and enstatite ($MgSiO_3$), in *High-Pressure Research: Applications in Geophysics,* edited by M. H. Manghnani and S. Akimoto, pp. 255-266, Academic, San Diego, Calif. 1977.

O'Neill, B., J. D. Bass, J. R. Smyth, and M. T. Vaughan, Elasticity of grossular-pyrope-almandine garnet, *J. Geophys. Res., 94,* 17819-17824, 1989.

O'Neill, B., and R. Jeanloz, Experimental petrology of the lower mantle: a natural peridotite taken to 54 GPa *Geophys. Res. Lett., 17,* 1477-1480, 1990.

Paulssen, H. Lateral heterogeneity of Europe's upper mantle as inferred from modeling of broad-band body waves, *Geophys. J. R. astr. Soc, 91,* 171-199, 1987.

Peltier, W. R., and L. P. Solheim, Mantle phase transitions and layered chaotic convection, *Geophys. Res. Lett., 19,* 321-324, 1992.

Plymate, T. G., and J. H. Stout, A five-parameter temperature corrected Murnaghan equation for P-V-T surfaces, *J. Geophys. Res., 94,* 9477-9483, 1989.

Press, F., Earth models consistent with geophysical data, *Phys. Earth Planet. Int., 3,* 3-22, 1970.

Press, W. H., B. P. Flannery, S. A. Teukolsky, W. T. Vetterling, *Numerical Recipes,* 818 pp., Cambridge University Press, Cambridge, 1986.

Randall, M.J., A Revised Travel-Time Table for S *Geophys. J. R. astr. Soc., 22,* 229-234, 1971.

Revenaugh, J., and T. H. Jordan, Mantle layering from Scs reverberations, 2., The transition zone, *J. Geophys. Res., 96,* 19763-19780, 1991.

Richet, P., H. Mao, and P. M. Bell, Bulk moduli of magnesiowüstites from static compression measurements, *J. Geophys. Res., 94,* 3037-3045, 1989.

Rigden, S. M., G. D. Gwanmesia, J. D. Fitz Gerald, I. Jackson, and R. C. Liebermann, Spinel elasticity and seismic structure of the transition zone of the mantle, *Nature, 354,* 143-145, 1991.

Ringwood, A. E., A model for the upper mantle, *J. Geophys. Res., 67,* 857-866, 1962.

Ringwood, A. E., *Composition and Petrology of the Earth's Mantle,* 618 pp., McGraw-Hill, New York, 1975.

Ringwood, A. E., Phase transformations and differentiation in subducted lithosphere: implications for mantle dynamics, basalt petrogenesis and crustal evolution, *J. Geol., 90,* 611-643, 1982.

Robie, R. A., B. S. Hemingway, and J. R. Fisher, Thermodynamic properties of minerals and related substances at 298.15 K and 1 bar (10^5 Pascals) pressure and higher temperatures, *U. S. Geol. Survey, Dept. of the Interior Bull. 1452*, 456 pp, 1976.

Robinson, R., and R. L. Kovach, Shear velocities in the Earth's mantle, *Phys. Earth Planet. Inter., 5*, 30-44, 1972.

Salerno, C. M., and J. P. Watt, Walpole bounds on the effective elastic moduli of isotropic multicomponent composites, *J. Appl. Phys., 60*, 1618-1624, 1986.

Sautter, V., S. E. Haggerty, and S. Field, Ultradeep (>300 kilometers) ultramafic xenoliths: petrological evidence from the transition zone, *Science, 252*, 827-830, 1991.

Sawamoto, H., D. Weidner, S. Sasaki, and M. Kumazawa, Single-crystal elastic properties of the modified spinel (beta) phase of Mg_2SiO_4, *Science, 224*, 749-751, 1984

Sawamoto, H., M. Kozaki, A. Jujimura, and T. Akamatsu, Precise measurement of compressibility of $\gamma - Mg_2SiO_4$ using synchrotron radiation, paper presented at 27th High Pressure Conference Sapporo, Japan, 1986; as quoted by *Akaogi et al.* [1989].

Saxena, S. K., *Thermodynamics of Rock-forming Minerals*, 188 pp., Springer-Verlag, New York, 1973.

Schulze, D. J., Constraints on the abundance of eclogite in the upper mantle, *Geophys. Res. Let., 94*, 4205-4212, 1989.

Schwartz, S. Y., T. Lay, and S. L. Beck, Shear wave travel time, amplitude and waveform analysis for earthquakes in the Kurile slab: constraints on deep slab structure and mantle heterogeneity, *J. Geophys. Res., 96*, 14445-14460, 1991.

Sengupta, M. K., and B. R. Julian, Radial variation of compressional and shear velocities in the Earth's lower mantle, *Geophys. J. R. astr. Soc., 54*, 185-219, 1978.

Shapiro, J. N., and L. Knopoff, Reduction of shock-wave equations of state to isothermal equations of state, *J. Geophys. Res., 74*, 1435-1438, 1969.

Shearer, P. M., Seismic imaging of upper-mantle structure with new evidence for a 520-km discontinuity, *Nature, 344*, 121-126, 1990.

Silver, P. G., R. W. Carlson, and P. Olson, Deep slabs, geochemical heterogeneity, and the large-scale structure of mantle convection: Investigation of an enduring paradox, *Ann. Revs Earth Planet. Sci., 16*, 477-541, 1988.

Silver, P. G., and W. W. Chan Observations of body wave multipathing from broadband seismograms: evidence for lower mantle slab penetration beneath the Sea of Okhotsk, *J. Geophys. Res., 91*, 13787-13802, 1986.

Skinner, B. J., Physical properties of end-members of the garnet group, *Am. Mineral., 41*, 428-436, 1956.

Stixrude L., and M. S. T. Bukowinski, Fundamental thermodynamic relations and silicate melting with implications for the constitution of D'', *J. Geophys. Res.* , *95*, 19311-19326, 1990

Stixrude, L., and M. S. T. Bukowinski, Thermodynamic analysis of the system $MgO-FeO-SiO_2$ at high pressure and the structure of the lowermost mantle *this volume,* 1992.

Stixrude, L., R. J. Hemley, Y. Fei, and H. K. Mao, Thermoelasticity of silicate perovskite and magnesiowüstite and stratification of the Earth's lower mantle, *Science, 257* 1099-1101, 1992.

Sueno, S., M. Cameron, and C. T. Prewitt, Orthoferrosilite: High temperature crystal chemistry, *Am. Mineral., 61,* 38-53, 1976.

Sung, C.-M., and R. G. Burns, Kinetics of high-pressure phase transformations: implications to the evolution of the olivine $\rightarrow$ spinel transition in the downgoing lithosphere and its consequences on the dynamics of the mantle, *Tectonophysics , 31,* 1-32, 1976.

Suzuki, I., Thermal expansion of olivine and periclase and their anharmonic properties, *J. Phys. Earth , 25,* 145-159, 1975a.

Suzuki, I., Cell parameters and linear thermal expansion coefficients of orthopyroxenes, *J. Seismol. Soc. Jpn., 28,* 1-9, 1975b.

Suzuki, I., Thermal expansion of $\gamma - Mg_2SiO_4$. *J. Phys. Earth, 27,* 53-61, 1979.

Suzuki, I., and O. L. Anderson, Elasticity and thermal expansion of a natural garnet up to 1000 K, *J. Phys. Earth., 31,* 125-138, 1983.

Suzuki, I., E. Ohtani, and M. Kumazawa, Thermal expansion of modified spinel, $\beta - Mg_2SiO_4$, *J. Phys. Earth, 28,* 273-280, 1980.

Suzuki, I., K. Seya, H. Takei, and Y. Sumino, Thermal expansion of fayalite, *Phys. Chem. Minerals, 7,* 60-63, 1981.

Takahashi, E. and E. Ito, Mineralogy of mantle peridotite along a model geotherm up to 700 km depth, in *High Pressure Research in Mineral Physics,* edited by M. H. Manghnani and Y. Syono, pp. 427-438, TERRAPUB/AGU, Tokoyo/Washington, 1987.

Tamai, H. and T. Yagi, High - pressure and high - temperature phase relations in $CaSiO_3$ and $CaMgSi_2O_6$ and elasticity of perovskite - type $CaSiO_3$, *Phys. Earth Planet. Int., 54,* 370-377, 1989.

Tanimoto, T., Waveform inversion for three-dimensional density and S wave structure, *J. Geophys. Res., 96,* 8167-8189, 1991.

Tonks, W. B., and H. J. Melosh, The physics of crystal settling and suspension in a turbulent magma ocean, in *Origin of the Earth,* edited by H. E. Newsom and J. H. Jones, pp. 151-174, Oxford University Press, New York, 1990.

Tralli, D. M., and L. R. Johnson, Lateral variations in mantle P velocity from tectonically regionalized tau estimates, *Geophys. J. R. astr. Soc., 86,* 475-489, 1986.

Uhrhammer, R., Shear-wave velocity structure for a spherically averaged earth, *Geophys. J. R. astr. Soc., 58*, 749-767, 1979.

van der Hilst, R., R. Engdahl, W. Spackman, and G. Nolet, Tomographic imaging of subducted lithosphere below northwest Pacific island arcs, *Nature, 353*, 37-43, 1991.

Vassiliou, M. S., B. H. Hager, and A. Raefsky, The distribution of earthquakes with depth and stress in subducting slabs, *J. Geodynam., 1*, 11-28, 1984.

Verhoogen, J., Phase changes and convection in the Earth's mantle, *Phil. Trans. R. Soc. London, A, 258*, 276-283, 1965.

Vinet, P., J. Ferrante, J. H. Rose, and J. R. Smith, Compressibility of solids, *J. Geophys. Res., 92*, 9319-9326, 1987.

Vinnik, L. P., and V. Z. Ryaboy, Deep structure of the east European platform according to seismic data, *Phys. Earth Planet. Inter., 25*, 27-37, 1981.

Walck, M. C., The P-wave upper mantle structure beneath an active spreading center: The Gulf of California, *Geophys. J. R. astr. Soc. , 76*, 697-723, 1984.

Walck, M. C., The upper mantle beneath the north-east Pacific rim: a comparison with the Gulf of California, *Gephys. J. R. astr. Soc., 81*, 243-276, 1985.

Walker, D., and C. Agee, Partitioning "equilibrium", temperature gradients, and constraints on Earth differentiation, *Earth Planet. Sci. Lett., 96*, 49-60, 1989.

Wang, C., A simple Earth model, *J. Geophys. Res., 77*, 4318-4329, 1972.

Watanabe, H., Thermochemical properties of synthetic high-pressure compounds relevant to the Earth's mantle, in *High Pressure Research in Geophysics,* edited by S. Akimoto and M. H. Manghnani, pp. 93-113, Center for Academic Publications, Tokoyo, 1982.

Watt, J. P., and T. J. Ahrens, Shock wave equation of state of enstatite, *J. Geophys. Res, 91*, 7495-7503, 1986.

Watt, J. P., G. F. Davies, and R. J. O'Connell, The elastic properties of composite materials, *Rev. Geophys. Space. Phys , 14*, 541-563, 1976.

Weaver, J. S., T. Takahashi, and J. Bass, Isothermal compression of grossular garnets to 250 kbars and the effect of calcium on the bulk modulus, *J. Geophys. Res., 81*, 2475-2482, 1976.

Weidner, D. J., A mineral physics test of a pyrolite mantle, *Geophys. Res. Lett., 12*, 417-420, 1985.

Weidner, D. J., and E. Ito, Elasticity of $MgSiO_3$ in the ilmenite phase, *Phys. Earth Planet. Inter., 40*, 65-70, 1985.

Weidner, D. J., and E. Ito, Mineral physics constraints on a uniform mantle composition, in *High Pressure Research in Mineral Physics,* edited by M. H. Manghnani and Y. Syono, pp. 427-438, TERRAPUB/AGU, Tokoyo/Washington, 1987.

Weidner, D. J., H. Sawamoto, and S. Sasaki, Single-crystal elastic properties of the spinel phase of Mg_2SiO_4, *J. Geophys. Res.*, *89*, 7852-7859, 1984

Weidner, D. J., H. Wang, and J. Ito, Elasticity of orthoenstatite, *Phys. Earth Planet. Int.*, *17*, P7-P13, 1978.

Weng, K., H. K. Mao, and P. M. Bell, Lattice parameters of the perovskite phase in the system $MgSiO_3$–$CaSiO_3$–Al_2O_3, *Carnegie Inst. Wash. Yearbook, 1981*, 273-277, 1982.

Wiggins, R. A., Monte Carlo inversion of body-wave observations, *J. Geophys. Res.*, *74*, 3171-3181, 1969.

Wiggins, R. A., The general linear inverse problem: implication of surface waves and free oscillations fro Earth structures, *Rev. Geophys. Space Phys.*, *10*, 251-285, 1972.

Wiggins, R. A., G. A. McMechan, and M. N. Toksoz, Range of Earth structure nonuniqueness implied by body wave observations, *Rev. Geophys. Space Phys.*, *11*, 87-113, 1973.

Williams, Q., E. Knittle, R. Reichlin, S. Martin, and R. Jeanloz, Structural and electronic properties of Fe_2SiO_4-fayalite at ultrahigh pressures: amorphization and gap closure, *J. Geophys. Res.*, *95*, 21549-21564, 1990.

Wood, B. J., Postspinel transformations and the width of the 670-km discontinuity: A comment on "Postspinel transformations in the system Mg_2SiO_4–Fe_2SiO_4 and some geophysical implications" by E. Ito and E. Takahashi, *J. Geophys. Res.*, *95*, 12681-12685, 1990.

Wood, B. J., and O. J. Kleppa, Thermochemistry of forsterite-fayalite olivine solutions, *Geochim. Cosmochim. Acta*, *45*, 529-534, 1981.

Wright, C., and J. R. Cleary, P wave travel-time gradient measurements for the Warramunga seismic array and lower mantle structure, *Phys. Earth Planet. Inter.*, *5*, 213-230, 1972.

Yeganeh-Haeri, A., D. J. Weidner, and E. Ito, Single crystal elastic moduli of magnesium metasilicate perovskite, in *Perovskite: A Structure of Great Interest to Geophysics and Materials Science*, edited by A. Navrotsky and D. J. Weidner, pp. 13-26, AGU, Washington, 1989.

Yeganeh-Haeri, A., D. J. Weidner, and E. Ito, Elastic properties of the pyrope-majorite solid solution series, *Geophys. Res. Lett.*, *17*, 2453-2456, 1990.

Zhao, W., D. A. Yuen and S. Honda, Multiple phase transitions and the style of mantle convection, *Phys. Earth Planet. Inter.*, *72*, 185-210, 1992.

Zhou, H. W., D. L. Anderson, and R. W. Clayton, Modeling of residual spheres for subduction zone earthquakes 1. Apparent slab penetration signatures in the NW Pacific caused by deep diffuse mantle anomalies. *J. Geophys. Res.*, *95*, 6799-6827, 1990.

Zhou, H. W., and R. W. Clayton, P and S wave travel-time inversions for subducting slabs under island arcs of the northwest pacific, *J. Geophys. Res.*, *95*, 6829-6851, 1990.

Zindler, A., and S. Hart, Chemical geodynamics, *Ann. Rev. Earth Planet. Sci., 14,* 493-571, 1986.

Appendix A

A common problem with estimating mean properties of the earth is the biased distribution of sources and recievers in certain tectonic regions. In order to overcome this obstacle, *Tralli and Johnson,* [1986] proposed a tectonic regionalization for the Earth. The then calculated pure region tau estimates and inverted them for the velocity structure in each region. using the areal distributions of these regions, a weighted global average can be computed in which the effects of the biased sampling have been accounted for. This is the approach I followed to calculate the mean P and S wave velocity profiles presented in chapter 2.

The regionalized tau estimates for S waves of *Tralli* [personal communication, 1991] were calculated according to the method outlined in *Tralli and Johnson,* [1986]. Tabulated values of P wave tau estimates can be found in *Tralli and Johnson,* [1986] while the S wave estimates are given in Tables A.1-7. I inverted these estimates for the average P and S velocity and their 68% confidence bounds using the method of *Bessonova et al.,* [1976]. The method requires and estimate of the velocity at the surface to begin the inversion. I used a simplex minimization routine described by *Press et al.,* [1986] to find the value which minimized the misfit of the tau values predicted by the resulting velocity profile and those used to determine the profile. The large amount of P wave arrival times resulted in very stable estimates of velocity. However, about an order of magnitude less data was available for the S wave tau estimates. It is assumed that this reduction in the amount of data is what gives rise to the numererous low velocity zones found in the profiles. In order to remove these anomalies, I again used the minimization routine mentioned above. The criteria I used simultaneously searched for pertubations to the expected tau values which minimized the difference between the expected and predicted tau values as well as minimizing the difference between the original and perturbed values. All perturbed values were required to stay within one standard deviation of the original values. The tau values that resulted fom this inversion are also reported in Tables A.1-7 and the velocity profiles are shown in Figures A.1-7.

p (s/deg)	τ (s)	τ_0 (s)	σ^2 (s^2)	N
23.75	16.959	16.265	5.767	47
23.00	36.392	40.272	5.973	22
22.40	50.030	50.615	4.961	41
21.20	70.886	68.525	4.848	47
20.30	87.000	87.265	4.926	231
19.40	108.039	108.415	4.269	60
18.80	120.955	120.527	3.730	32
17.60	148.534	148.782	3.348	11
16.80	166.094	165.625	2.361	65
16.20	179.540	180.444	2.858	33
15.65	190.791	190.482	2.311	62
15.35	201.519	201.459	3.538	54
15.05	211.552	211.371	3.009	108
14.75	222.459	222.112	2.592	87
14.45	237.467	237.960	2.598	50
14.15	250.081	249.589	2.362	49
13.85	266.237	267.344	2.472	41
13.55	280.202	281.095	2.621	71
13.25	295.137	289.781	2.124	8
12.95	313.058	316.849	3.341	40
12.65	332.283	332.784	2.330	101
12.35	350.086	350.373	2.989	82
12.05	367.959	365.928	2.580	116
11.75	388.282	387.603	2.511	92
11.45	411.745	413.634	3.078	115
11.15	432.520	431.711	2.665	64
10.85	455.898	455.750	2.703	121
10.55	479.151	480.384	3.807	70
10.25	503.301	502.244	2.100	60
9.95	529.321	529.616	2.215	43

TABLE A.1. Tau-p values for tectonic region 1. τ is the value of tau that was used in the velocity inversion, τ_0 is the original value of tau, σ^2 is the variance of tau, and N is the number of traveltimes that were used in the estimate of tau after uniform variance reduction (see Tralli and Johnson, 1986).

p (s/deg)	τ (s)	τ_0 (s)	σ^2 (s^2)	N
23.75	10.673	11.017	4.823	556
23.00	26.170	24.858	5.319	422
22.40	44.055	45.409	5.378	1260
21.20	68.001	67.778	3.353	257
20.30	86.197	86.410	4.130	1253
19.40	102.387	102.065	3.660	954
18.80	113.491	113.576	3.841	801
17.60	141.693	141.717	3.419	540
16.80	161.597	161.505	3.799	363
16.20	175.229	175.239	3.778	301
15.65	188.594	188.548	3.320	595
15.35	197.260	197.391	3.959	962
15.05	206.324	206.231	3.101	346
14.75	218.091	217.971	3.575	1176
14.45	232.432	232.617	3.689	1154
14.15	245.278	245.163	2.772	310
13.85	260.186	260.257	3.476	528
13.55	275.620	275.501	3.105	219
13.25	293.798	293.811	3.816	552
12.95	311.411	311.464	3.890	478
12.65	328.882	328.830	3.216	428
12.35	347.931	347.994	2.883	360
12.05	367.312	367.090	3.308	312
11.75	389.748	390.246	3.808	756
11.45	409.692	409.424	2.846	348
11.15	432.001	432.054	3.438	706
10.85	455.311	455.337	3.338	364
10.55	478.602	478.594	3.087	778
10.25	502.395	502.382	2.558	113
9.95	526.836	526.813	2.766	527

TABLE A.2. Same as Table A.1, but for tectonic region 2.

p (s/deg)	τ (s)	τ_0 (s)	σ^2 (s^2)	N
23.75	2.821	3.153	5.144	272
23.00	13.248	12.019	6.426	343
22.40	29.529	30.465	7.491	398
21.20	56.176	56.926	5.475	58
20.30	71.478	70.602	5.513	117
19.40	94.099	94.506	4.610	58
18.80	108.017	107.484	5.196	94
17.60	136.691	136.645	4.683	172
16.80	158.051	158.881	5.586	168
16.20	171.727	170.947	5.272	96
15.65	185.367	185.376	3.919	134
15.35	194.678	194.580	4.065	178
15.05	203.816	204.375	3.187	99
14.75	214.115	213.319	4.840	169
14.45	228.168	228.788	4.185	236
14.15	241.894	242.013	3.718	146
13.85	257.863	256.916	3.208	80
13.55	276.622	277.111	3.806	572
13.25	293.503	293.738	3.923	394
12.95	309.666	309.456	3.573	624
12.65	327.661	327.830	3.052	351
12.35	345.009	345.104	3.274	586
12.05	364.579	364.167	3.048	248
11.75	387.226	387.450	3.653	436
11.45	408.146	408.020	3.237	119
11.15	431.336	431.714	3.314	434
10.85	452.874	452.135	3.304	364
10.55	476.600	477.462	2.527	266
10.25	499.871	498.594	3.176	234
9.95	524.966	525.453	3.522	427

TABLE A.3. Same as Table A.1, but for tectonic region 3.

p (s/deg)	τ (s)	τ_0 (s)	σ^2 (s^2)	N
23.75	18.814	18.693	6.247	1967
23.00	34.838	35.450	6.273	985
22.40	44.740	44.095	6.544	2140
21.20	66.863	66.957	4.923	819
20.30	83.924	83.811	5.457	1083
19.40	101.819	101.912	4.425	1984
18.80	114.405	114.344	3.871	909
17.60	139.939	140.090	4.753	3597
16.80	156.122	155.978	4.327	595
16.20	170.189	170.213	3.442	428
15.65	187.119	187.235	3.691	1745
15.35	196.503	196.379	3.344	1272
15.05	207.735	207.770	2.513	380
14.75	219.896	219.849	3.884	1816
14.45	233.271	233.390	3.728	726
14.15	245.868	245.740	3.681	953
13.85	259.832	259.842	3.043	858
13.55	276.601	276.657	2.672	995
13.25	292.420	292.332	3.340	2445
12.95	310.121	310.151	3.015	1695
12.65	328.424	328.399	2.738	603
12.35	347.882	347.910	2.825	1206
12.05	367.204	367.169	3.280	1550
11.75	387.824	387.848	2.767	1029
11.45	408.197	408.167	3.130	630
11.15	429.918	429.915	2.995	1222
10.85	453.492	453.534	3.032	682
10.55	476.008	475.960	3.108	1136
10.25	499.326	499.346	2.983	825
9.95	524.037	524.037	3.056	564

TABLE A.4. Same as Table A.1, but for tectonic region 4.

p (s/deg)	τ (s)	τ₀ (s)	σ² (s²)	N
23.75	7.633	7.555	3.602	559
23.00	21.635	21.759	5.486	669
22.40	32.718	32.615	5.131	453
21.20	57.655	57.563	4.184	361
20.30	76.135	76.248	3.155	196
19.40	94.693	94.489	3.300	147
18.80	110.064	110.284	3.989	774
17.60	137.512	137.288	4.103	471
16.80	156.468	156.560	3.742	643
16.20	170.017	170.007	2.761	302
15.65	183.519	183.445	3.749	398
15.35	193.327	193.382	3.413	205
15.05	204.874	204.680	2.843	339
14.75	217.701	218.214	3.077	199
14.45	228.912	228.454	3.462	294
14.15	242.995	242.856	3.065	684
13.85	257.458	257.618	3.320	446
13.55	271.553	271.484	3.541	769
13.25	289.030	289.123	3.081	229
12.95	305.453	305.298	3.399	506
12.65	324.007	323.993	3.490	1032
12.35	344.224	344.312	3.349	696
12.05	363.015	362.922	3.561	891
11.75	384.430	384.455	3.091	367
11.45	404.818	404.773	3.238	557
11.15	426.437	426.450	2.999	718
10.85	449.253	449.272	3.487	941
10.55	472.342	472.291	3.355	1290
10.25	497.697	497.724	3.172	1216
9.95	523.016	523.032	3.862	675

TABLE A.5. Same as Table A.1, but for tectonic region 5.

p (s/deg)	τ (s)	τ_0 (s)	σ^2 (s^2)	N
23.00	10.145	9.102	9.127	322
22.40	21.460	22.302	8.421	264
21.20	47.175	46.556	7.713	365
20.30	69.440	69.689	6.904	94
19.40	92.167	91.878	5.095	84
18.80	108.306	108.474	4.628	96
17.60	137.240	137.046	3.581	43
16.80	157.707	157.536	3.678	41
16.20	173.103	173.627	2.912	47
15.65	185.274	184.551	3.310	67
15.35	193.734	193.940	4.412	112
15.05	204.244	203.950	3.373	176
14.75	217.289	217.833	2.808	29
14.45	228.579	228.010	3.041	78
14.15	242.068	242.155	2.525	71
13.85	256.051	255.785	2.938	77
13.55	273.153	273.210	2.179	89
13.25	289.414	289.363	2.876	115
12.95	307.126	307.177	3.210	79
12.65	325.902	325.826	2.965	76
12.35	346.189	346.236	2.783	115
12.05	366.544	366.363	3.645	242
11.75	389.022	389.149	2.294	184
11.45	410.702	410.322	2.530	240
11.15	435.462	436.173	2.933	56
10.85	457.033	456.443	3.107	170
10.55	480.640	480.635	1.865	66
10.25	504.475	504.492	2.291	190
9.95	528.237	528.240	2.544	133

TABLE A.6. Same as Table A.1, but for tectonic region 6.

p (s/deg)	τ (s)	τ_0 (s)	σ^2 (s^2)	N
23.75	22.317	21.989	3.987	171
23.00	35.249	35.883	4.515	235
22.40	44.901	44.150	3.825	323
21.20	66.545	67.328	3.649	397
20.30	80.874	80.255	3.045	371
19.40	98.319	98.156	3.248	1137
18.80	112.896	113.007	2.431	377
17.60	138.166	138.579	3.115	603
16.80	152.582	152.344	2.298	186
16.20	169.735	169.982	3.554	424
15.65	184.334	184.284	2.124	147
15.35	193.269	192.912	2.973	229
15.05	205.539	205.887	2.696	281
14.75	216.763	216.679	2.148	253
14.45	228.756	228.977	2.602	77
14.15	242.626	242.193	2.551	361
13.85	259.628	259.907	2.938	514
13.55	275.209	275.363	3.176	265
13.25	291.018	290.946	3.053	308
12.95	309.675	309.812	3.226	352
12.65	327.722	327.635	2.342	163
12.35	346.719	346.961	2.811	311
12.05	365.060	364.854	2.703	267
11.75	385.669	384.988	2.599	369
11.45	409.430	409.773	2.315	165
11.15	430.363	430.387	2.704	236
10.85	452.961	453.154	2.309	138
10.55	475.910	475.423	2.287	131
10.25	501.192	501.227	2.154	155
9.95	526.427	526.445	2.518	118

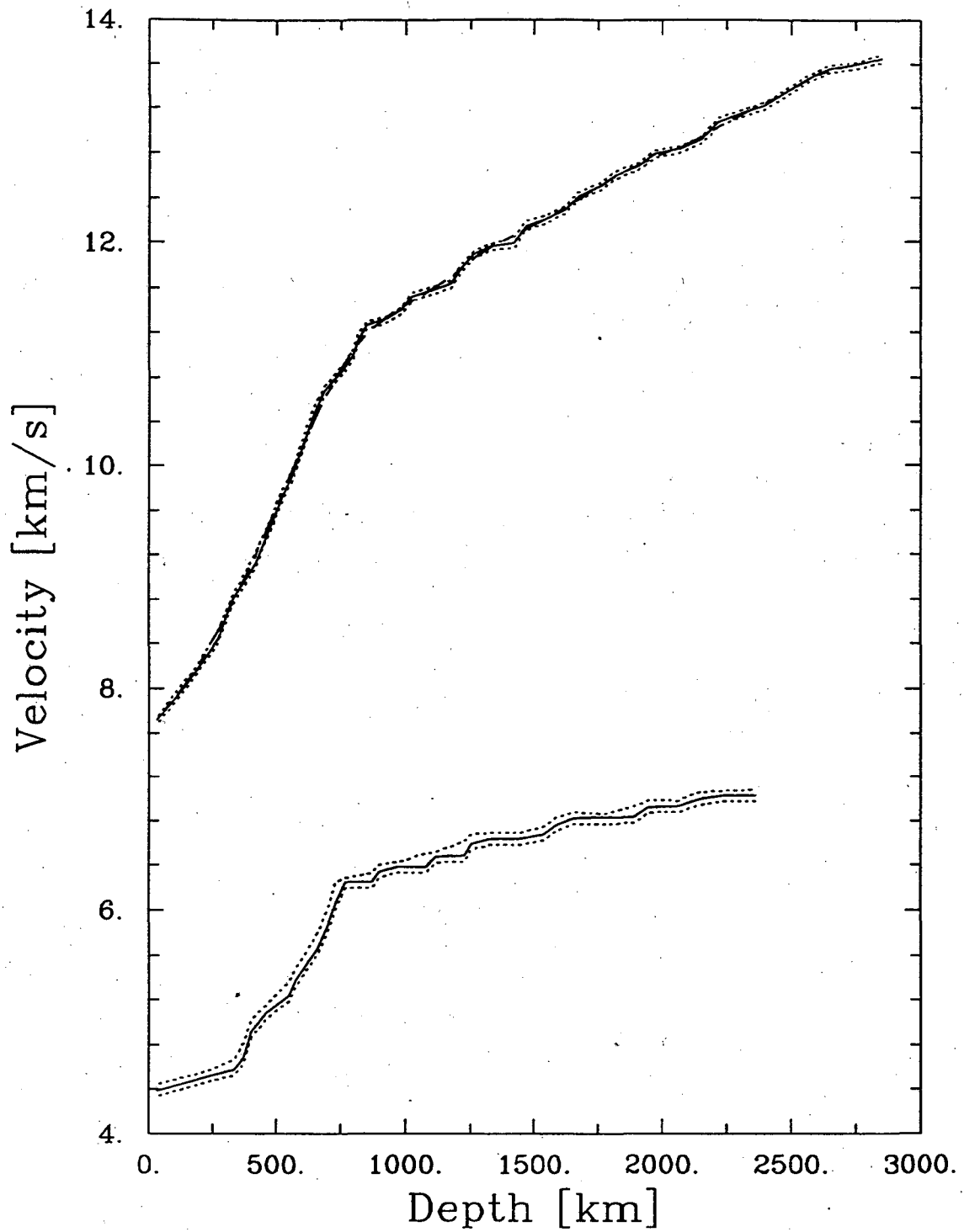TABLE A.7. Same as Table A.1, but for tectonic region 7.

Fig. A.1. P and S wave velocity profiles before smoothing (solid lines), after smoothing (dashed lines) and their 68 % uncertainties (dotted lines) in tectonic region 1.
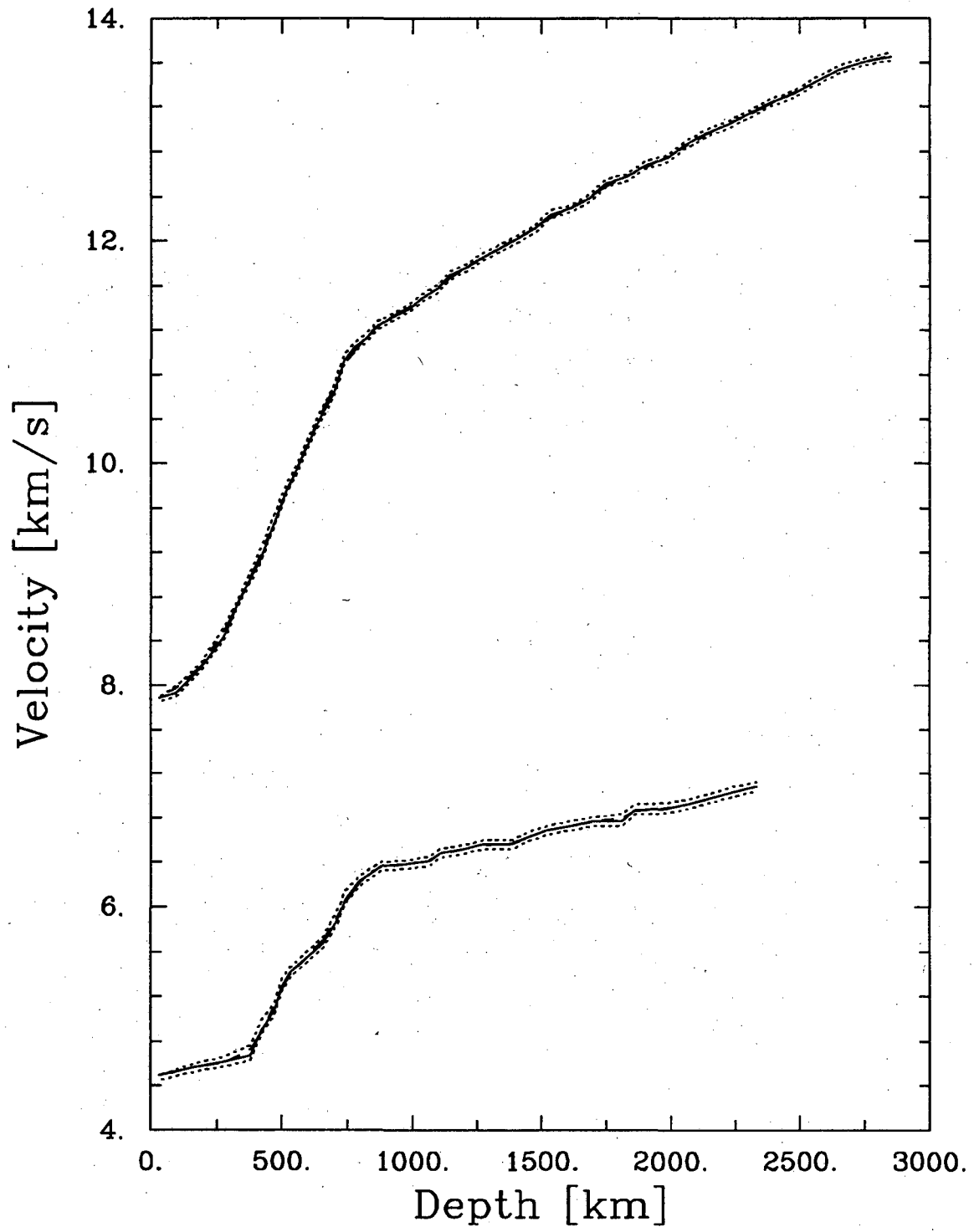
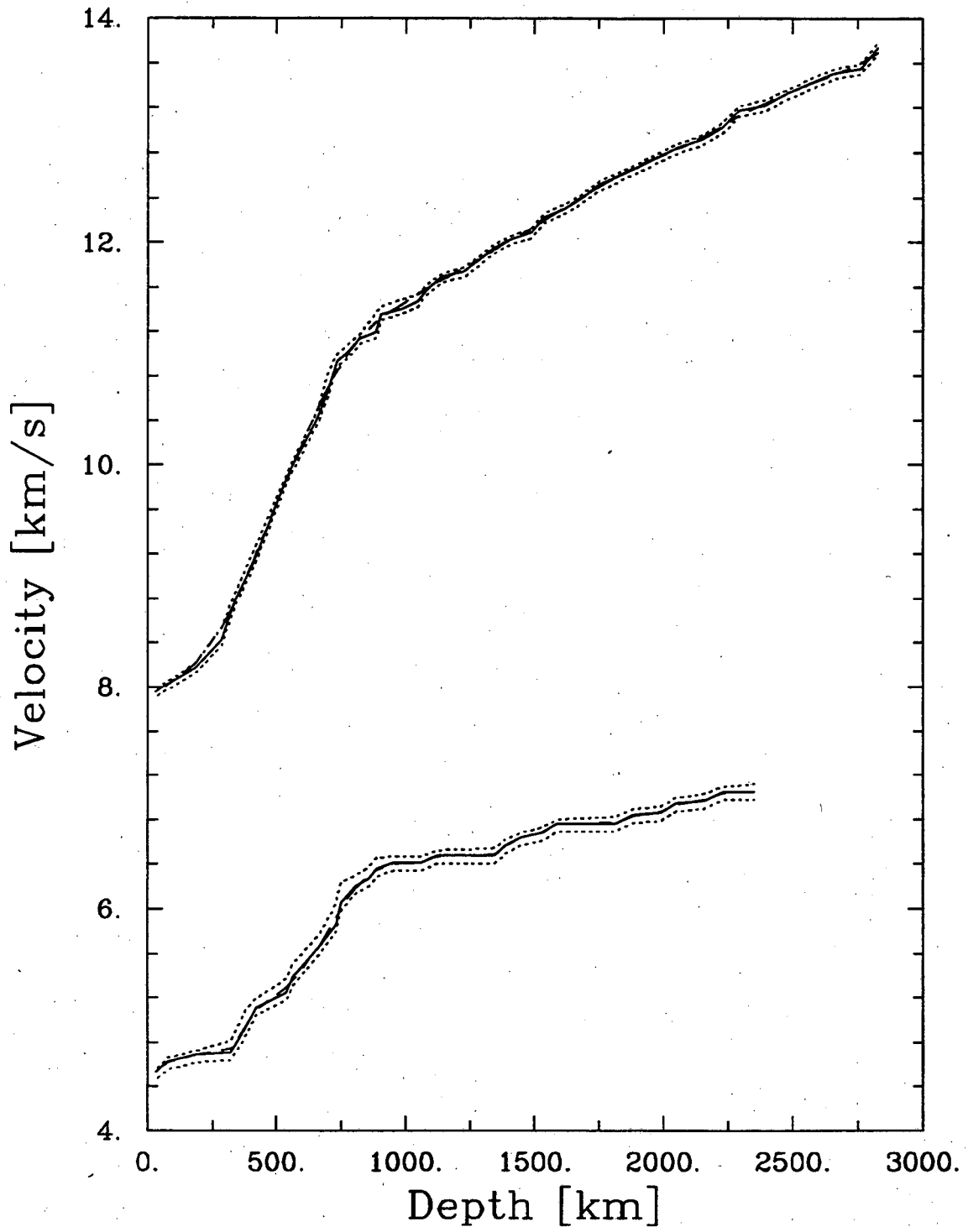Fig. A.2. Same as Figure A.1, but for region 2.

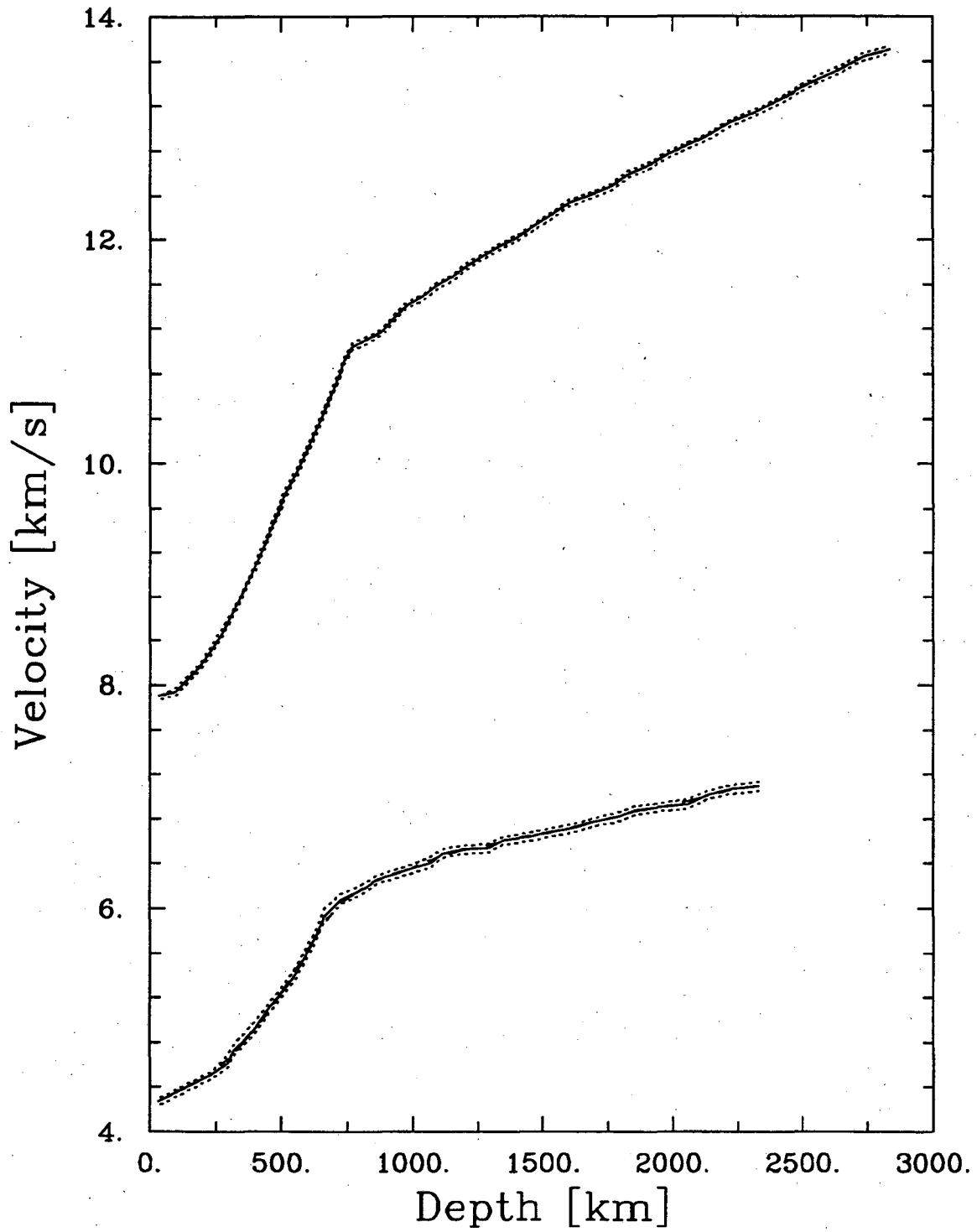Fig. A.3. Same as Figure A.1, but for region 3.
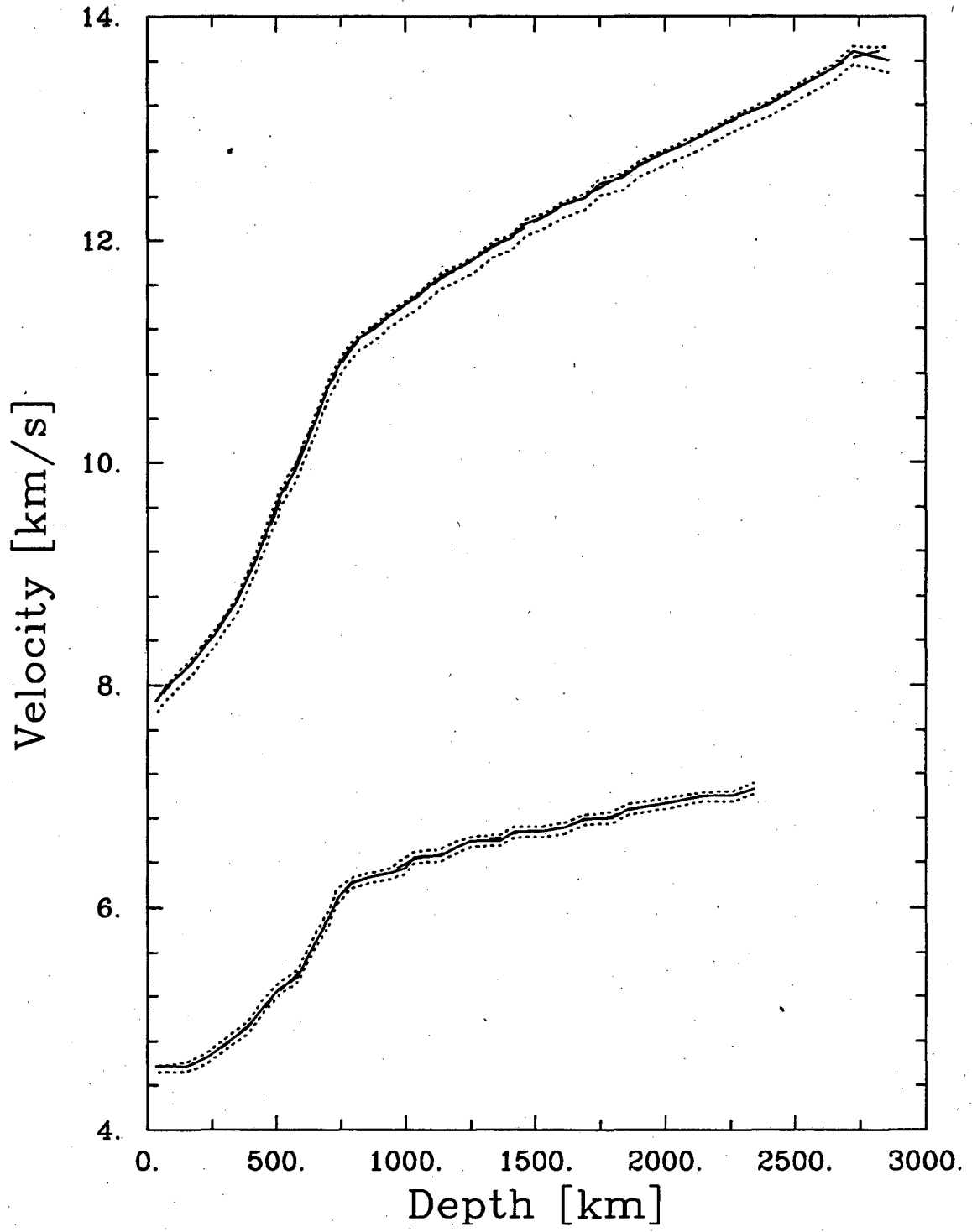
Fig. A.4. Same as Figure A.1, but for region 4.

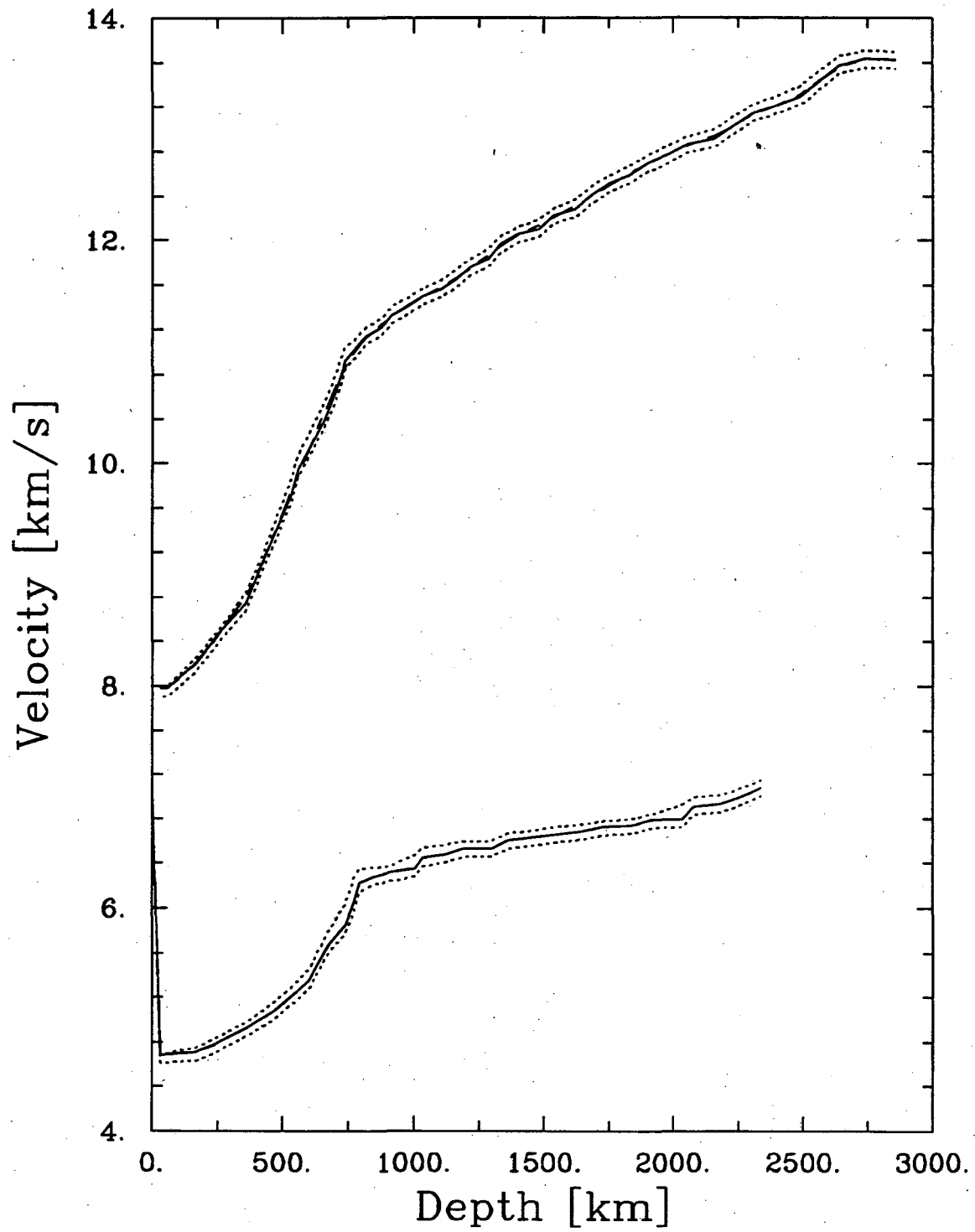Fig. A.5. Same as Figure A.1, but for region 5.

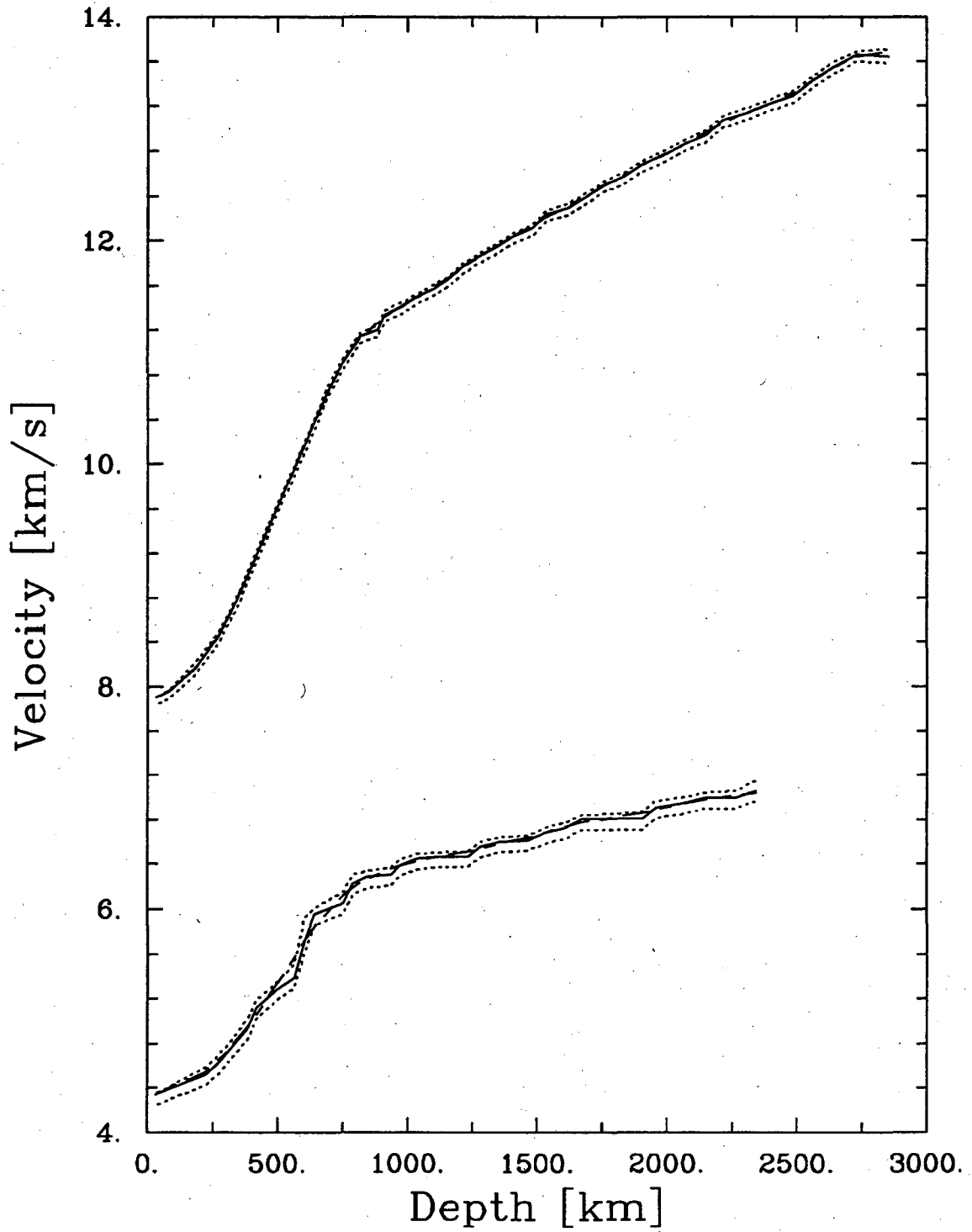Fig. A.6. Same as Figure A.1, but for region 6.

Fig. A.7. Same as Figure A.1, but for region 7.

The velocity-depth values given by the inversion represent the average velocity in an undetermined depth interval that is bounded by the the velocity-depth point directly above and below the point being considered. Because of the variablity of the averaging interval, the profiles generated by the inversion may contain spurious fluctuations about an assumed smooth underlying distribution. To recover this smooth profile, a generalized cross-validation technique described by *Craven and Wahba* [1979] was used to objectively fit a smoothing spline through the velocity points taking into account their confidence bounds. The resulting smoothed profiles are also shown in Figures A.1-7. As one can see, the velocity profiles do not contain noticeable upper mantle discontinuities. The discontinuites could not be resolved in this study due to lack of data on the backbranches of the traveltime curves. For this reason, I used the a different technique to get a more representative estimate of the mean and uncertainty in the velocity profile of the upper mantle as discussed in Chapter 2. To date, no noticeable discontinuites exist in the lower mantle over the depth range considered here. Thus, this method will should provide an accuarate representation of velocity and its uncertainty in this region.

A global mean velocity profile (v_m) is calculated from the regional profiles (v_j) via:

$$v_m = \sum_{j=1}^{7} w_j v_j \qquad \text{A.1}$$

where the weights w_j are the fractional surface area for the each region j (Table A.8). Confidence bounds for the mean profile are obtained from the bounds on the regional profiles using the same weighting scheme. Given the mean P and S velocity profiles, bulk sound velocity is calculated via:

$$V_\Phi = \sqrt{V_P^2 - 4/3 V_S^2} \qquad \text{A.2}$$

In order to assure a conservative estimate of the uncertainty on V_Φ, its upper bound is calculated using the upper bound on V_P and the lower bound of V_S in Equation A.2 and vice versa for its lower bound. The resulting V_P, V_Φ, and V_S profiles are shown in Figure A.8.

Tectonic Region	Fractional Area
(1) Young oceans	0.13
(2) Intermediate-age oceans	0.34
(3) Old oceans	0.13
(4) Active continents	0.19
(5) Continental platforms	0.10
(6) Continental shields	0.07
(7) Oceanic trenches	0.04

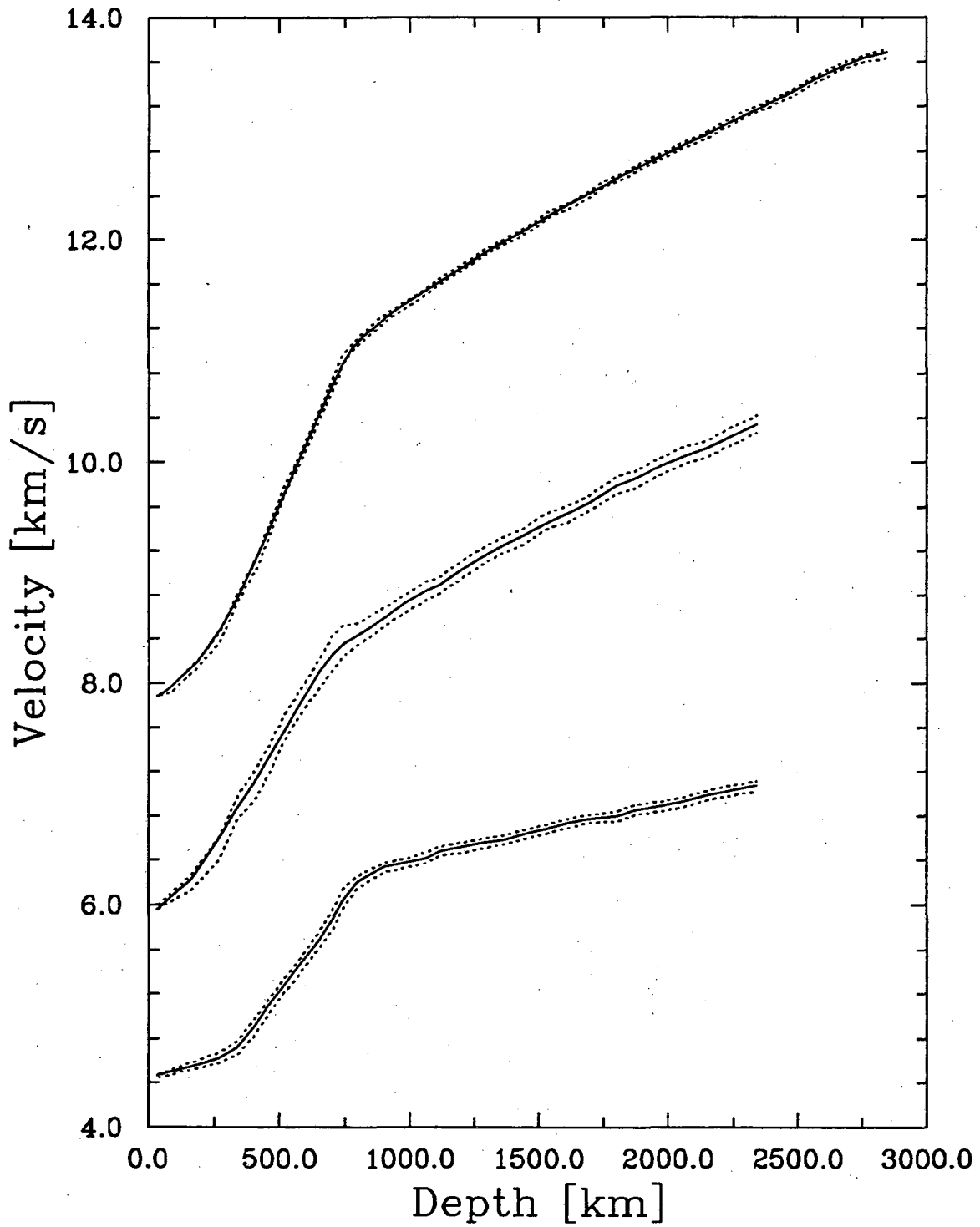TABLE A.8. Fractional surface area of the tectonic regions.

Fig. A.8. Globally averaged P, bulk sound, and S wave velocity profiles (solid lines) and their 68 % uncertainties (dotted lines).

LAWRENCE BERKELEY LABORATORY
UNIVERSITY OF CALIFORNIA
TECHNICAL INFORMATION DEPARTMENT
BERKELEY, CALIFORNIA 94720